The Astrophysical Journal Supplement Series, 252:32 (27pp), 2021 February https://doi.org/10.3847/1538-4365/abd1dc

Mid-infrared Outbursts in Nearby Galaxies (MIRONG). I. Sample Selection and Characterization

Ning Jiang[1,2], Tinggui Wang[1,2], Liming Dou[3], Xinwen Shu[4], Xueyang Hu[1,2], Hui Liu[1,2], Yibo Wang[1,2], Lin Yan[5], Zhenfeng Sheng[1,2], Chenwei Yang[6], Luming Sun[1,2,4], and Hongyan Zhou[1,6]
[1] CAS Key Laboratory for Research in Galaxies and Cosmology, Department of Astronomy, University of Science and Technology of China, Hefei, 230026, People's Republic of China; jnac@ustc.edu.cn
[2] School of Astronomy and Space Sciences, University of Science and Technology of China, Hefei, 230026, People's Republic of China; twang@ustc.edu.cn
[3] Department of Astronomy, Guangzhou University, Guangzhou 510006, People's Republic of China; doulm@gzhu.edu.cn
[4] Department of Physics, Anhui Normal University, Wuhu, Anhui, 241000, People's Republic of China
[5] Caltech Optical Observatories, California Institute of Technology, Pasadena, CA 91125, USA
[6] Polar Research Institute of China, 451 Jinqiao Road, Shanghai, 200136, People's Republic of China
Received 2020 May 23; revised 2020 November 22; accepted 2020 December 7; published 2021 February 9

Abstract

Optical time-domain astronomy has grown rapidly in the past decade, but the dynamic infrared sky is rarely explored. Aiming to construct a sample of mid-infrared outbursts in nearby galaxies (MIRONG), we have conducted a systematical search of low-redshift ($z < 0.35$) Sloan Digital Sky Survey spectroscopic galaxies that have experienced recent mid-infrared (MIR) flares using their Wide-field Infrared Survey Explorer (WISE) light curves. A total of 137 galaxies have been selected by requiring a brightening amplitude of 0.5 mag in at least one WISE band with respect to their quiescent phases. Only a small fraction (10.9%) has corresponding optical flares. Except for the four supernovae (SNe) in our sample, the MIR luminosities of the remaining sources ($L_{4.6\,\mu m} > 10^{42}$ erg s^{-1}) are markedly brighter than known SNe, and their physical locations are very close to the galactic center (median $<0\farcs1$). Only four galaxies are radio-loud, indicating that synchrotron radiation from relativistic jets could contribute to MIR variability. We propose that these MIR outbursts are dominated by the dust echoes of transient accretion onto supermassive black holes, such as tidal disruption events (TDEs) and turn-on (changing-look) active galactic nuclei. Moreover, the inferred peak MIR luminosity function is generally consistent with the X-ray and optical TDEs at the high end, albeit with large uncertainties. Our results suggest that a large population of transients has been overlooked by optical surveys, probably due to dust obscuration or intrinsically optical weakness. Thus, a search in the infrared band is crucial for us to obtain a panoramic picture of nuclear outburst. The multiwavelength follow-up observations of the MIRONG sample are in progress and will be presented in a series of subsequent papers.

Unified Astronomy Thesaurus concepts: Time domain astronomy (2109); Tidal disruption (1696); Active galactic nuclei (16); Infrared astronomy (786)

1. Introduction

Time-domain astronomy has developed rapidly in the past two decades. This great progress has been driven by the advent of new instruments and facilities dedicated to wide-field, deep, and fast surveys, such as the Catalina Real-Time Survey (CRTS; Drake et al. 2009), Palomar Transient Factory (PTF/iPTF; Law et al. 2009), Panoramic Survey Telescope and Rapid Response System (Pan-STARRS or PS; Kaiser 2004; Chambers et al. 2016), All Sky Automated Survey for SuperNovae (ASASSN; Shappee et al. 2014), Asteroid Terrestrial-impact Last Alert System (ATLAS; Tonry et al. 2018), and Zwicky Transient Facility (ZTF; Graham et al. 2019a). These remarkable projects have gradually made it possible to image the entire sky every few days and process the data in real time. It is believed that LSST will produce an unprecedented time-domain survey in the 2020s.

Supernovae (SNe) are absolutely the major class of extragalactic transients, and their number has experienced explosive growth, as expected, with the aid of the abovementioned surveys. In 2018, there were more than 7000 reported SNe,[7] although most have not been spectroscopically confirmed. In addition to increasing the number of SNe, these surveys have also accelerated the discovery and in-depth studies of peculiar SNe, such as superluminous SNe (SLSNe, e.g., ASASSN-15lh; Dong et al. 2016; see Gal-Yam 2019 as a recent review), exotic SNe with multiple peaks (e.g., iPTF14hls; Arcavi et al. 2017), and even gravitationally lensed SNe (iPTF16geu; Goobar et al. 2017). These unusual events could make great breakthroughs in our understanding of stellar explosion in extreme physical conditions.

The other population of extragalactic variable sources that has aroused great attention consists of the transient events associated with the supermassive black holes (SMBHs) located in the centers of galaxies. Among them, the tidal disruption event (TDE), in which a star is torn apart by an SMBH's tidal force, is of particular interest. During the process, about half of the stellar mass may be ejected, while the rest of the stellar material is accreted onto the BH, producing a luminous flare of electromagnetic radiation lasting for months to years (Rees 1988; Evans & Kochanek 1989; Phinney 1989). Discoveries of TDEs require modern time-domain surveys because their event rate is hundreds of times lower than SNe, with a rate of 10^{-4}–10^{-5} galaxy^{-1} yr^{-1} (Wang & Merritt 2004; Stone & Metzger 2016). Hence, the number of TDEs (or candidates) found to date is still very limited. As a rare and special form of accretion, TDEs are nevertheless extremely scientifically valuable, as they offer us an ideal chance to probe the existence, mass, and spin of SMBHs in normal galaxies (Lu et al. 2017;

[7] http://rochesterastronomy.org/sn2018/index.html

Mockler et al. 2019; Pasham et al. 2019). Moreover, they can serve as a unique laboratory to study the dynamic process of BH activity by witnessing the ignition and flameout of the accretion disk (e.g., Wevers et al. 2019), as well as rapidly launched jets (e.g., Bloom et al. 2011; Burrows et al. 2011; Mattila et al. 2018).

Despite occasionally swallowing stars, SMBHs are believed to grow mainly by accreting surrounding gas during their active galactic nucleus (AGN) phases. Stochastic variability is ubiquitous in AGNs, among which a small fraction are extremely variable, with light curves featuring flaring (e.g., Graham et al. 2017) or state-changing (e.g., Graham et al. 2019b) patterns. Follow-up spectroscopic observations of the most variable AGNs suggest that they can even change their types on timescales of years, characterized by the appearance or disappearance of broad emission lines (e.g., Shappee et al. 2014; LaMassa et al. 2015; Runnoe et al. 2016; MacLeod et al. 2016; Yang et al. 2018; Guo et al. 2020). These objects are dubbed changing-look (CL) AGNs, and their variation is driven by the dramatic change of the accretion flow rather than the obscuration (Sheng et al. 2017; Hutsemékers et al. 2019). The most intriguing subclass could be the so-called "turn-on" AGNs, which transition from a quiescent galaxy to a type 1 AGN within several months to years. Although only a few such systems have been confirmed (Gezari et al. 2017; Yan et al. 2019; see also Frederick et al. 2019), they do not appear to be extremely rare, and even one poses challenges to canonical accretion disk theories.

In a nutshell, the known extragalactic transient sky is dominated by SNe and transient SMBH accretion. The investigation of the latter has been facilitated recently by improved time-domain surveys. Current large surveys have been exclusively performed in the optical band that are blind to transients that are either self-obscured (e.g., type 2 AGNs) or located in the dusty regions (e.g., SNe). Therefore, it is crucial to conduct surveys in bands free of dust obscuration. In this sense, the mid-infrared (MIR) is the most promising band, but it was completely unexplored until the Spitzer Deep Wide-Field Survey, which has now been incorporated into the Decadal IRAC Boötes Survey. This survey is used to search for obscured SNe and study the quasar variability in the MIR (Kozlowski et al. 2010) by taking advantage of the repeatedly surveyed region ($\sim$9 deg^2). The SPitzer InfraRed Intensive Transients Survey (SPIRITS; Kasliwal et al. 2017) is a more recent project dedicated to finding infrared luminous transients by targeting 190 nearby galaxies and has yielded numerous hidden SNe and dusty stellar outbursts (Jencson et al. 2019). Despite this, such projects generally focus on a small sample of galaxies or a small sky region, so they are almost incapable of capturing rare events like TDEs and turn-on AGNs.

Fortunately, the Wide-field Infrared Survey Explorer (WISE) mission (Wright et al. 2010) and its asteroid-characterization extension, the Near-Earth Object Wide-field Infrared Survey Explorer Reactivation (NEOWISE) mission (Mainzer et al. 2014), have opened a new window to explore the dynamic MIR sky thanks to its survey mode (see Section 2.1). For instance, Sheng et al. (2020) came up with an efficient method to look for CL AGNs from MIR-variable quasars screened by WISE light curves (see also Assef et al. 2018; Stern et al. 2018) but with the caveat that only "turn-off" CL AGNs can be selected because of their parent sample of quasars. Wang et al. (2018) used WISE to systematically search for TDEs in extremely variable normal galaxies and discovered IR echoes of TDEs immediately after the pioneering discoveries of IR echoes of TDEs (Dou et al. 2016; Jiang et al. 2016; van Velzen et al. 2016). However, Wang et al. (2018) selected variables using the variability flag given by the WISE pipeline, which is based on data taken between 2009 December and 2011 February. As a result, the acquired galaxies have all entered the stage of dimming, which makes the further confirmation of their physical nature unrealistic.

To overcome the limitation from Wang et al. (2018), we have designed a new project to search for and explore MIR outbursts in nearby galaxies (MIRONG) specifically. MIRONG uses both the public WISE and NEOWISE databases to search for more recent outburst events in galaxies and enable multiwavelength follow-up. MIRONG may uncover a population of extragalactic transients that have been overlooked by traditional optical surveys and ultimately improve our understanding of the extragalactic dynamic sky. The paper is organized as follows. In Section 2, we describe the process of sample selection of MIRONG. In Sections 3–5, we characterize the sample from properties of MIR light curves, event rate and luminosity function, and host galaxies, respectively. We inspect the nature of MIRONG in Section 6 and discuss the implications of our work in Section 7. Finally, we end with a brief summary and discussion of future prospects in Section 8. We assume a cosmology with $H_0 = 70$ km s^{-1} Mpc^{-1}, $\Omega_m = 0.3$, and $\Omega_\Lambda = 0.7$.

2. Sample Selection

2.1. Characteristics of WISE and NEOWISE

WISE performed a full-sky imaging survey in four broad bandpasses centered at 3.4, 4.6, 12, and 22 μm (labeled W1–W4) from 2010 January to August. WISE continued surveying the sky in its bluest three bands during 2010 August and September. After that, NEOWISE hunted asteroids until 2011 February (Mainzer et al. 2011), with only the W1 and W2 channels remaining operational, as the solid hydrogen cryogen used to cool the W3 and W4 instrumentation had been depleted. Following a 33 month hibernation period, the WISE instrument recommenced survey operations in 2013 December (Mainzer et al. 2014). This posthibernation mission to hunt for asteroids that could pose an impact hazard to the Earth is referred to as NEOWISE-Reactivation (NEOWISE-R).

The WISE survey strategy is very novel. It has a field of view of $47' \times 47'$ and a small (10%) overlap between adjacent fields in one orbit. The scan circle advances by about $4'$ orbit^{-1}, and 15 orbits can be fulfilled each day. Therefore, for a typical sky region, the available exposures can be segmented into a series of 1 day time intervals (referred to as "visits"), with such visits occurring once every 6 months, except for the gap during the hibernation. As a spontaneous outcome of the unique survey mode, it becomes an unprecedented database to study the transient MIR sky. There are typically 12 successive orbits covering a given source within 1 day, with denser coverage toward higher ecliptic latitudes (Wright et al. 2010; Hoffman et al. 2012). Such a high-frequency sampling allows us to probe the intraday MIR variability, which was seldom explored in the past (e.g., Jiang et al. 2012; Jiang 2018).

The NEOWISE survey was still ongoing at the time of submission of this paper. Our sample selection is based on the WISE and NEOWISE-R data from 2010 to the end of 2018, which is all of the data that were available when we did this work. They have yielded an average of 12 visits for each target, so an investigation of MIR variability on year timescales is absolutely achievable for a large sample, as proved by previous

works (e.g., Wang et al. 2018). We noticed that the latest NEOWISE data release (2020 March 26) came out just before our paper submission, and it would be a massive effort to redo our work from the very beginning by including the newly released data from 2018 to 2019 December. However, the newest photometry has been added in the analysis of our final sample of MIRONG, since the more complete light curves will help us obtain more accurate quantities (e.g., peak luminosity).

2.2. Parent Sample

The Sloan Digital Sky Survey (SDSS) has spectroscopically observed millions of galaxies with an apparent Petrosian magnitude of $r < 17.77$ (Strauss et al. 2002). We have checked the SDSS DR14 spectroscopic catalog (Abolfathi et al. 2018) and picked out those flagged with a "GALAXY" class at $z < 0.35$, that is, 1,253,962 spectra in total. Note that some of them are repeated multi-epoch data for the same objects; there are 1,150,901 unique objects differentiated by their celestial coordinates. We choose spectroscopic galaxies instead of photometric because we need to know our galaxies' redshift ($z < 0.35$) and other properties. The redshift cut is to ensure that the Hα region is located in the wavelength range of the SDSS spectrum first, which will help us diagnose the spectral type by emission-line ratios in the Baldwin–Phillips–Terlevich (BPT) diagnostic diagram (Baldwin et al. 1981). Second, the cut of $z < 0.35$ will keep the dust emission within the WISE bands, as it is expected to start at 2 μm. Furthermore, the signal-to-noise ratios (S/Ns) of more distant galaxies are generally too low to undertake variability studies accurately. We designate these $\sim$1 million galaxies as the parent sample.

2.3. MIR-variable Galaxies

We construct a sample of MIR-variable galaxies in advance of the final selection of outbursts. We retrieved the W1 and W2 profile-fit photometry of each galaxy in the parent sample from the public AllWISE Multiepoch Photometry Table and NEOWISE-R Single Exposure (L1b) Source Table,[8] encompassing all exposures from 2010 to 2018. The photometry is measured by point-spread function (PSF) profile fitting, in which the PSFs have been estimated from observations of many tens of thousands of stars. The AllWISE multiframe pipeline detects sources on the deep coadded atlas images and then measures the sources for all available single-exposure images in all bands simultaneously, while the NEOWISE magnitudes are obtained by PSF fit to individual exposures directly.

The acquired single-exposure data are first filtered by the quality flags marked in the catalogs. The bad data points with poor-quality frames (`qi_fact` < 1), charged particle hits (`saa_sep` < 5), scattered moonlight (`moon_masked` $= 1$), and artifacts (`cc_flags` $\neq 0$) have been removed. In addition, we have also abandoned the photometry fitted with multiple PSF components (`nb` > 1 and `na` > 0) that is performed when the source is fit concurrently with other nearby detections or a single object is split into two components during the fitting process. The surviving data are immediately binned every half year to increase the S/N of the photometry, resulting in an average of 13 epochs for each target. This binning strategy fits the sampling rate of the WISE survey (see Section 2.1). We begin to perform a blind search of variable galaxies that satisfy δW1 > 0.5 or δW2 > 0.5. Here δW1 (δW2) is the difference between the maximum and minimum values of W1 and W2 across the combined ALLWISE +NEOWISE light curves. We have further requested δW1 > 0.3 or δW2 > 0.3 during the NEOWISE phase to make sure the variability is still obvious after 2013 December for ease of follow-up studies. The latter condition has also excluded fake variable sources caused by a possible systematical offset between ALLWISE and NEOWISE photometry. The significance of the variability is required to be not lower than 5σ, that is, $(W?\ \max - W?\ \min)\Big/\sqrt{(W?\ \max\_\mathrm{err})^2 + (W?\ \_\mathrm{err})^2} > 5$, to ensure that the variability is still valid when taking uncertainties into consideration. Last, we have cast away faint sources with the cut $W2\,\min < 14$ to obtain a magnitude limit sample.

The above cut of variability amplitude has resulted in a sample consisting of 1026 galaxies,[9] allowing us to visually check their MIR light curves one by one. While stochastic variability is predominant, peculiar variability patterns are also visible (see Figure 1), such as state transition and long-term declining and flare-like rising light curves. We notice that very few of them (11 objects) show periodic oscillations with a cycle of 1 yr (see the example in the top left panel of Figure 1). These objects are affected by the latent image artifact from a nearby bright star that appears in the preceding image in the scan.[10] The photometry pipeline has often failed to flag them automatically, so the 1 yr cycle variations may not be real. In addition, we emphasize that our selection of MIR-variable sources is conservative, and the actual fraction of these galaxies may be much higher than 0.1%, as we inferred here.

2.4. Sample of MIRONG: Galaxies with MIR Outburst

For the purpose of this study, we further selected a subsample of MIR outburst galaxies, which initially display a stable phase yet are followed by a significant brightening seen in the MIR light curves. The emission in the quiescent state serves as the background that will be subtracted from the outburst light curves. We estimated the preoutburst magnitudes by adopting the median value of the data points in the quiescent state. The beginning of the outburst is set to the epoch when either the W1 or W2 magnitude shows a brightening over 3σ significance. We adopted two criteria to qualify a flare: (1) the maximum flux density after outburst has brightened by >0.5 mag in W1 or W2 with respect to the quiescent state (ΔW1 > 0.5 or ΔW2 > 0.5) and (2) the variability significance at the epoch of maximum flux is larger than 5σ in at least one band. The above criteria are effective, with which we yield 148 MIR outburst sources. Lastly, we caution that the WISE spatial resolutions at the W1 and W2 bands are $\sim 6''$, so the photometry could suffer from the contamination of nearby sources. Thus, we rejected those targets with companions (galaxy pairs or polluted by foreground stars) within a projected distance closer than $6''$ by visually checking their SDSS images. As a result, 137 objects are left, constituting the final outburst sample

[8] https://irsa.ipac.caltech.edu/cgi-bin/Gator/nph-scan?mission=irsa&submit=Select&projshort=WISE

[9] General information on the 1026 variable galaxies can be downloaded from this website: http://staff.ustc.edu.cn/~jnac/data_public/wisevar.txt.

[10] The WISE scan direction on the sky flips every 6 months as the orbit precesses around the sky. Hence, a particular point on the sky will alternate being scanned north-to-south and south-to-north every 6 months. This means that the bright star that is seen on the preceding image in one epoch will be seen on the following image 6 months later. As a consequence, the artifact affection is periodic with a 1 yr cycle. The polluted photometry should have been flagged as "P" in "cc_flags," but the flag does not work well when the source is slightly offset from the predicted position of the latent and the expected size of the latent is poorly modeled.

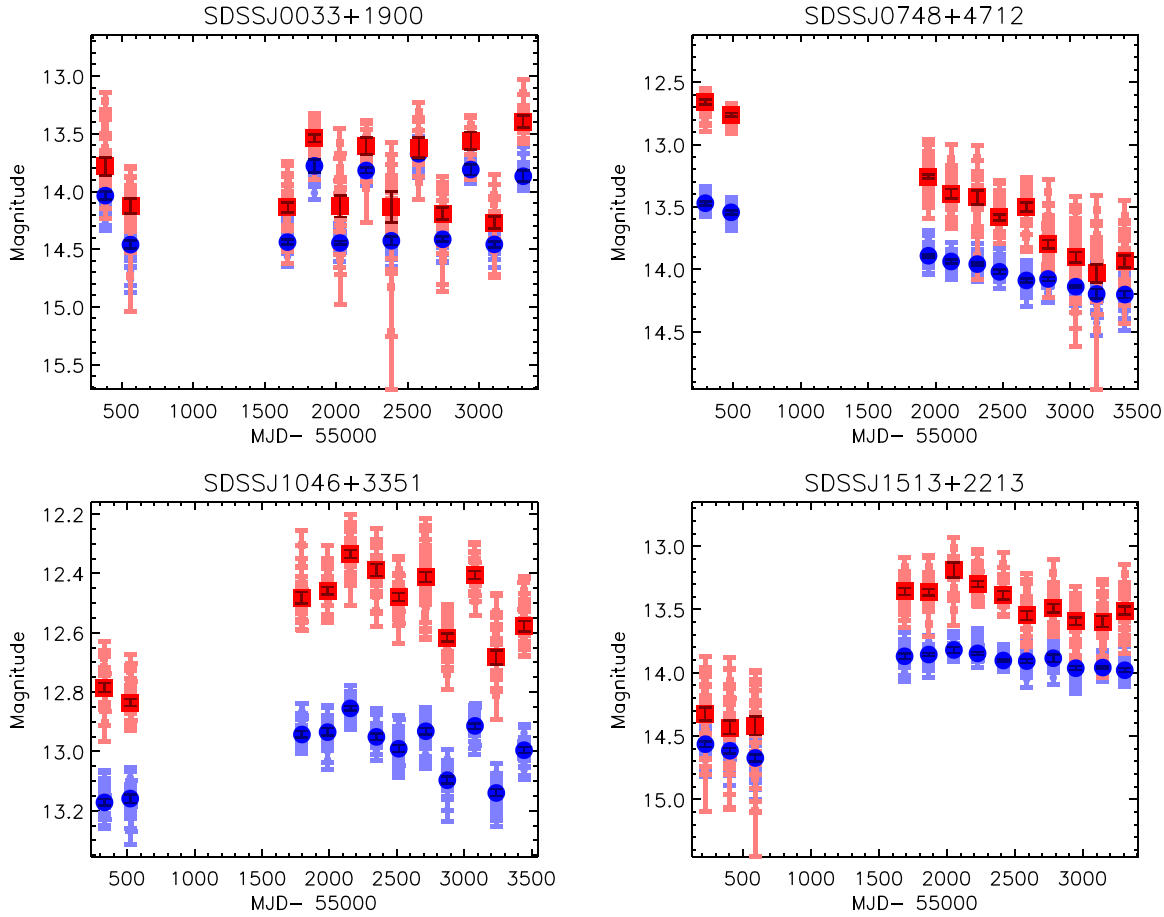

Figure 1. We show the different WISE light-curve patterns of the MIR-variable galaxies, including the periodic oscillation (top left), long-term decl. (top right), stochastic variation (bottom left), and state transition (bottom right). The recent flare-like patterns are presented separately in Figure 2. Blue dots: W1 (3.4 μm); red squares: W2 (4.6 μm). The raw single exposures are plotted in light blue and red, while the binned data are plotted in dark blue and red. As we explained in Section 2.3, the case of a 1 yr cycle of oscillation (top left) is not physical but caused by the latent image artifact from a nearby bright star.

(see the basic parameters in Table 1 and four representative examples in Figure 2). The median redshift is 0.102 (see Figure 3).

To summarize, we have finally selected a well-defined sample of 137 MIRONG that display a brightening over 0.5 mag with respect to the previous quiescent phase in the WISE light curves. These galaxies are all initially drawn from the SDSS spectroscopic catalog with rich available information, e.g., properties of host galaxies and nuclear activities (see Section 5), which allows for further detailed study of the nature of transient MIR emission in the center of galaxies.

3. Properties of MIRONG

3.1. Optical Counterparts

It is natural to ask whether these MIR flares have been detected by various optical surveys. First, we cross-matched our sample with the (candidate) SN catalog (Gal-Yam et al. 2013)[11] discovered between 2010 and 2018 and yielded 11 objects. In addition, we have also added four more objects that are reported in the literature but not listed in the SN catalog, including two Gaia nuclear transients (SDSS J0854+1113 and SDSS J1647+3843; Kostrzewa-Rutkowska et al. 2018), one CRTS outburst event (SDSS J1332+2036; Drake et al. 2019), and another turn-on quasar discovered by iPTF (SDSS J1554+3629; Gezari et al. 2017). The basic information about the 15 known optical transients is presented in Table 2.

Among these sources, SDSS J0936+0615, SDSS J1531+3724, SDSS J1540+0054, and SDSS J1554+1636 are spectroscopically confirmed SNe discovered by ASASSN. Object SDSS J0158–0052 is a candidate TDE discovered by Pan-STARRS and ASASSN that occurred in a Seyfert 1 galaxy with a low-mass BH (Blanchard et al. 2017) whose MIR flare has been successfully explained by the dust echo of the AGN torus (Jiang et al. 2017). Objects SDSS J1554+3629, SDSS J0915+4814, and SDSS J1133+6701 are newly reported turn-on AGNs that have transferred from LINERs to quasars within a few years (Gezari et al. 2017; Frederick et al. 2019). Object SDSS J1620+2407 is a candidate TDE discovered by ATLAS that shows marked newly appeared broad Balmer lines and blue continuum (Fraser et al. 2017). Apart from the nine studied objects above, the remaining six sources have only been alerted by photometry without further spectroscopic observations. Despite a lack of reliable identification, in contrast with the four SN cases ($>1''$), their close distance to the galactic center ($<1''$) suggests that they are likely associated with SMBH activity rather than a stellar explosion.

For the remaining 120 galaxies for which no known optical counterparts are matched, we have also examined the public CRTS (Drake et al. 2009) and ASASSN (Kochanek et al. 2017)

[11] See http://rochesterastronomy.org/supernova.html, noting that they are not all real SNe but candidates including nuclear transients.

Table 1
The Properties of MIR Flares

Name	R.A.	Decl.	z	ΔW1 (mag)	ΔW2 (mag)	W1m (mag)	W2m (mag)	L_{W1} (erg s^{-1})	L_{W2} (erg s^{-1})	Δd (arcsec)
(1)	(2)	(3)	(4)	(5)	(6)	(7)	(8)	(9)	(10)	(11)
SDSS J000046.46+143813.0	0.193583	14.6369	0.13660	0.32 ± 0.05	0.58 ± 0.05	-24.19 ± 0.14	-25.37 ± 0.08	43.19 ± 0.06	43.27 ± 0.03	0.08
SDSS J002701.03+071357.6	6.754291	7.23266	0.13109	0.37 ± 0.03	0.60 ± 0.06	-23.91 ± 0.07	-24.94 ± 0.10	43.08 ± 0.03	43.10 ± 0.04	0.02
SDSS J004500.47−004723.1	11.25195	−0.7897	0.05677	0.72 ± 0.04	1.17 ± 0.16	-21.99 ± 0.06	-22.93 ± 0.10	42.31 ± 0.02	42.30 ± 0.04	0.43
SDSS J010320.42+140149.8	15.83508	14.0305	0.04181	1.29 ± 0.03	1.90 ± 0.02	-25.34 ± 0.01	-26.30 ± 0.01	43.65 ± 0.01	43.64 ± 0.00	0.07
SDSS J012047.99−082918.4	20.19995	−8.4884	0.03468	0.42 ± 0.03	0.55 ± 0.02	-24.10 ± 0.07	-25.02 ± 0.04	43.16 ± 0.03	43.13 ± 0.02	0.07
SDSS J012100.67+140517.3	20.25279	14.0881	0.12938	0.36 ± 0.03	0.61 ± 0.07	-23.35 ± 0.12	-24.88 ± 0.14	42.85 ± 0.05	43.08 ± 0.06	0.11
SDSS J015804.75−005221.8	29.51979	−0.8727	0.08044	2.16 ± 0.04	2.71 ± 0.11	-24.60 ± 0.02	-25.56 ± 0.03	43.35 ± 0.01	43.35 ± 0.01	0.09
SDSS J020552.16+000411.8	31.46733	0.06994	0.07649	1.17 ± 0.01	1.76 ± 0.09	-24.81 ± 0.02	-25.85 ± 0.03	43.44 ± 0.01	43.46 ± 0.01	0.09
SDSS J074547.87+265537.9	116.4494	26.9271	0.11481	0.73 ± 0.07	0.82 ± 0.04	-24.81 ± 0.08	-25.99 ± 0.04	43.44 ± 0.03	43.52 ± 0.02	0.11
SDSS J075709.69+190842.8	119.2903	19.1452	0.10501	0.38 ± 0.02	0.69 ± 0.07	-23.78 ± 0.05	-24.83 ± 0.08	43.02 ± 0.02	43.05 ± 0.03	0.07
SDSS J081121.40+405451.8	122.8391	40.9143	0.06704	0.63 ± 0.02	0.52 ± 0.03	-24.88 ± 0.03	-25.75 ± 0.06	43.47 ± 0.01	43.42 ± 0.02	0.04
SDSS J081403.78+261144.3	123.5157	26.1956	0.07567	0.26 ± 0.03	0.61 ± 0.01	-23.23 ± 0.15	-24.77 ± 0.03	42.81 ± 0.06	43.03 ± 0.01	0.09
SDSS J081451.87+533732.5	123.7161	53.6256	0.13901	0.47 ± 0.01	0.83 ± 0.06	-24.16 ± 0.03	-25.27 ± 0.06	43.18 ± 0.01	43.23 ± 0.02	0.09
SDSS J083536.49+493542.7	128.9020	49.5951	0.04238	0.75 ± 0.08	1.38 ± 0.02	-23.55 ± 0.08	-24.66 ± 0.01	42.93 ± 0.03	42.99 ± 0.00	0.10
SDSS J083721.86+414342.0	129.3410	41.7283	0.09806	0.31 ± 0.02	0.58 ± 0.08	-24.06 ± 0.07	-25.22 ± 0.12	43.14 ± 0.03	43.21 ± 0.05	0.09
SDSS J084157.98+052605.7	130.4915	5.43491	0.15631	0.44 ± 0.03	0.65 ± 0.04	-24.95 ± 0.07	-25.95 ± 0.06	43.49 ± 0.03	43.50 ± 0.02	0.15
SDSS J084232.87+235719.6	130.6369	23.9554	0.06353	0.51 ± 0.04	0.76 ± 0.02	-23.06 ± 0.09	-23.80 ± 0.04	42.74 ± 0.03	42.64 ± 0.02	0.06
SDSS J084752.78+514236.2	131.9699	51.7100	0.11997	0.23 ± 0.08	0.61 ± 0.04	-22.86 ± 0.33	-24.37 ± 0.08	42.66 ± 0.13	42.87 ± 0.03	0.08
SDSS J085434.65+111334.7	133.6443	11.2263	0.16719	0.42 ± 0.03	0.56 ± 0.03	-25.77 ± 0.06	-26.66 ± 0.05	43.82 ± 0.02	43.79 ± 0.02	0.08
SDSS J085835.90+412113.8	134.6495	41.3538	0.08705	0.19 ± 0.06	0.53 ± 0.07	-21.12 ± 0.60	-23.14 ± 0.17	41.96 ± 0.24	42.38 ± 0.07	0.10
SDSS J085959.46+092225.6	134.9977	9.37377	0.15188	1.09 ± 0.03	1.49 ± 0.08	-25.56 ± 0.03	-26.59 ± 0.03	43.74 ± 0.01	43.76 ± 0.01	0.01
SDSS J090924.55+192004.8	137.3522	19.3346	0.10716	0.62 ± 0.06	1.29 ± 0.08	-23.64 ± 0.10	-25.13 ± 0.05	42.97 ± 0.04	43.17 ± 0.02	0.15
SDSS J091531.04+481407.7	138.8793	48.2354	0.10049	0.54 ± 0.02	0.75 ± 0.05	-24.29 ± 0.03	-25.08 ± 0.06	43.23 ± 0.01	43.16 ± 0.02	0.05
SDSS J093135.46+662652.2	142.8977	66.4478	0.08729	0.27 ± 0.02	0.52 ± 0.04	-22.78 ± 0.07	-23.73 ± 0.09	42.63 ± 0.03	42.62 ± 0.03	0.07
SDSS J093608.58+061525.4	144.0357	6.25705	0.00800	0.70 ± 0.03	0.79 ± 0.06	-18.29 ± 0.04	-18.52 ± 0.09	40.83 ± 0.02	40.53 ± 0.04	1.49
SDSS J094303.26+595809.3	145.7635	59.9692	0.07491	0.25 ± 0.01	0.67 ± 0.04	-21.62 ± 0.06	-23.07 ± 0.07	42.16 ± 0.03	42.35 ± 0.03	0.20
SDSS J094456.56+310552.2	146.2356	31.0978	0.03465	0.42 ± 0.04	0.84 ± 0.04	-22.99 ± 0.10	-23.95 ± 0.03	42.71 ± 0.04	42.70 ± 0.01	0.12
SDSS J095754.76+020711.2	149.4781	2.11977	0.12528	0.40 ± 0.05	0.60 ± 0.07	-24.01 ± 0.11	-24.98 ± 0.11	43.12 ± 0.04	43.11 ± 0.04	0.01
SDSS J100120.37+182926.6	150.3348	18.4907	0.10603	0.37 ± 0.06	0.74 ± 0.12	-22.99 ± 0.14	-24.13 ± 0.18	42.71 ± 0.06	42.78 ± 0.07	0.30
SDSS J100256.90+442457.8	150.7370	44.4160	0.15446	0.16 ± 0.02	0.62 ± 0.05	-23.62 ± 0.12	-25.54 ± 0.07	42.96 ± 0.05	43.34 ± 0.03	0.18
SDSS J100350.97+020227.6	150.9623	2.04100	0.12470	0.63 ± 0.02	0.90 ± 0.09	-24.29 ± 0.03	-25.13 ± 0.08	43.23 ± 0.01	43.17 ± 0.03	0.01
SDSS J100809.02+154951.3	152.0375	15.8309	0.11765	0.55 ± 0.02	0.81 ± 0.10	-24.60 ± 0.04	-25.63 ± 0.10	43.35 ± 0.01	43.37 ± 0.04	0.15
SDSS J100931.70+343604.7	152.3820	34.6013	0.20863	0.45 ± 0.04	0.69 ± 0.08	-24.94 ± 0.08	-26.03 ± 0.10	43.49 ± 0.03	43.53 ± 0.04	0.08
SDSS J100955.70+220949.3	152.4820	22.1636	0.14153	0.49 ± 0.03	0.66 ± 0.06	-24.90 ± 0.05	-25.80 ± 0.08	43.48 ± 0.02	43.44 ± 0.03	0.03
SDSS J101157.62+534857.9	152.9900	53.8160	0.23440	0.47 ± 0.05	0.70 ± 0.07	-25.62 ± 0.11	-26.78 ± 0.08	43.76 ± 0.04	43.83 ± 0.03	0.05
SDSS J101708.94+122412.0	154.2872	12.4033	0.10762	0.61 ± 0.04	0.95 ± 0.05	-23.66 ± 0.06	-24.60 ± 0.06	42.98 ± 0.02	42.96 ± 0.02	0.05
SDSS J102017.72+251554.3	155.0738	25.2650	0.13145	0.54 ± 0.04	1.06 ± 0.09	-23.50 ± 0.09	-24.67 ± 0.08	42.91 ± 0.04	42.99 ± 0.03	0.18
SDSS J102934.88+252635.8	157.3953	25.4432	0.23761	0.91 ± 0.02	0.85 ± 0.08	-26.11 ± 0.03	-26.64 ± 0.08	43.96 ± 0.01	43.78 ± 0.03	0.14
SDSS J102959.95+482937.9	157.4997	48.4938	0.23235	0.78 ± 0.10	0.89 ± 0.03	-25.95 ± 0.10	-26.91 ± 0.04	43.89 ± 0.04	43.89 ± 0.01	0.02
SDSS J103753.68+391249.6	159.4736	39.2137	0.10677	0.46 ± 0.03	1.07 ± 0.08	-23.31 ± 0.08	-24.78 ± 0.07	42.84 ± 0.03	43.03 ± 0.03	0.06
SDSS J104138.79+341253.5	160.4116	34.2148	0.14028	0.42 ± 0.04	0.62 ± 0.12	-24.30 ± 0.11	-25.14 ± 0.16	43.23 ± 0.04	43.18 ± 0.06	0.07
SDSS J104306.56+271602.1	160.7773	27.2672	0.12812	0.90 ± 0.06	1.46 ± 0.05	-24.45 ± 0.06	-25.42 ± 0.04	43.29 ± 0.02	43.29 ± 0.02	0.27
SDSS J104609.61+165511.4	161.5400	16.9198	0.20687	0.42 ± 0.04	0.54 ± 0.05	-25.59 ± 0.09	-26.60 ± 0.09	43.75 ± 0.04	43.76 ± 0.03	0.07
SDSS J105145.47+210132.1	162.9394	21.0255	0.06593	0.35 ± 0.03	0.60 ± 0.07	-22.24 ± 0.09	-23.24 ± 0.11	42.41 ± 0.04	42.42 ± 0.04	0.10

Table 1
(Continued)

Name	R.A.	Decl.	z	ΔW1 (mag)	ΔW2 (mag)	W1m (mag)	W2m (mag)	L_{W1} (erg s^{-1})	L_{W2} (erg s^{-1})	Δd (arcsec)
(1)	(2)	(3)	(4)	(5)	(6)	(7)	(8)	(9)	(10)	(11)
SDSS J105344.12+552405.7	163.4338	55.4015	0.15174	0.27 ± 0.03	0.51 ± 0.04	−23.84 ± 0.14	−25.14 ± 0.09	43.05 ± 0.06	43.18 ± 0.03	0.07
SDSS J105801.52+544437.0	164.5063	54.7436	0.13062	0.30 ± 0.03	0.77 ± 0.04	−23.43 ± 0.10	−24.98 ± 0.05	42.89 ± 0.04	43.11 ± 0.02	0.06
SDSS J110501.98+594103.5	166.2582	59.6843	0.03369	0.94 ± 0.02	1.26 ± 0.02	−24.22 ± 0.02	−24.96 ± 0.01	43.20 ± 0.01	43.11 ± 0.01	0.08
SDSS J110958.34+370809.6	167.4930	37.1360	0.02602	0.44 ± 0.02	0.93 ± 0.03	−22.63 ± 0.05	−23.69 ± 0.03	42.57 ± 0.02	42.60 ± 0.01	0.14
SDSS J111122.44+592334.3	167.8435	59.3928	0.16973	0.47 ± 0.02	0.71 ± 0.07	−24.48 ± 0.05	−25.34 ± 0.09	43.31 ± 0.02	43.26 ± 0.03	0.06
SDSS J111431.83+405613.8	168.6326	40.9371	0.15247	0.50 ± 0.03	0.57 ± 0.02	−25.20 ± 0.07	−26.11 ± 0.03	43.60 ± 0.03	43.57 ± 0.01	0.07
SDSS J111536.57+054449.7	168.9023	5.74713	0.08995	1.08 ± 0.12	1.85 ± 0.28	−24.39 ± 0.08	−25.58 ± 0.06	43.27 ± 0.03	43.35 ± 0.03	0.33
SDSS J112018.31+193345.8	170.0762	19.5627	0.12780	0.76 ± 0.05	0.94 ± 0.07	−25.22 ± 0.05	−26.03 ± 0.06	43.60 ± 0.02	43.54 ± 0.02	0.16
SDSS J112238.84+143348.4	170.6618	14.5634	0.19421	0.51 ± 0.02	0.52 ± 0.02	−25.76 ± 0.04	−26.53 ± 0.05	43.82 ± 0.02	43.73 ± 0.02	0.05
SDSS J112446.21+045525.4	171.1925	4.92372	0.07398	0.36 ± 0.02	0.83 ± 0.04	−23.37 ± 0.06	−24.89 ± 0.04	42.86 ± 0.02	43.08 ± 0.02	0.09
SDSS J112916.12+513123.5	172.3171	51.5231	0.03286	0.21 ± 0.02	0.74 ± 0.02	−22.24 ± 0.09	−24.06 ± 0.02	42.41 ± 0.04	42.75 ± 0.01	0.04
SDSS J113355.93+670107.0	173.4830	67.0186	0.03968	0.50 ± 0.04	0.71 ± 0.08	−23.37 ± 0.09	−24.29 ± 0.09	42.86 ± 0.04	42.84 ± 0.04	0.02
SDSS J113901.27+613408.5	174.7552	61.5690	0.13461	0.30 ± 0.01	0.65 ± 0.05	−23.68 ± 0.06	−25.17 ± 0.06	42.99 ± 0.02	43.19 ± 0.03	0.08
SDSS J114922.02+544151.4	177.3417	54.6976	0.06190	0.77 ± 0.01	1.14 ± 0.10	−23.53 ± 0.02	−24.38 ± 0.06	42.93 ± 0.01	42.88 ± 0.02	0.17
SDSS J115205.33+485049.9	178.0222	48.8471	0.15102	0.85 ± 0.07	1.06 ± 0.06	−25.42 ± 0.06	−26.33 ± 0.04	43.68 ± 0.02	43.65 ± 0.02	0.08
SDSS J115326.76+403719.1	178.3615	40.6219	0.14510	0.62 ± 0.04	0.96 ± 0.04	−24.51 ± 0.07	−25.56 ± 0.03	43.32 ± 0.03	43.35 ± 0.01	0.20
SDSS J120057.93+064823.1	180.2413	6.80641	0.03599	0.45 ± 0.04	0.80 ± 0.05	−24.10 ± 0.08	−25.47 ± 0.05	43.15 ± 0.03	43.31 ± 0.02	0.05
SDSS J120145.97+352522.5	180.4415	35.4229	0.19031	0.64 ± 0.03	0.95 ± 0.03	−25.52 ± 0.05	−26.64 ± 0.03	43.72 ± 0.02	43.78 ± 0.01	0.04
SDSS J120338.31+585911.8	180.9096	58.9866	0.04692	0.54 ± 0.04	1.03 ± 0.06	−21.37 ± 0.08	−22.59 ± 0.06	42.06 ± 0.03	42.16 ± 0.02	0.09
SDSS J120842.69+330523.0	182.1778	33.0897	0.28028	0.38 ± 0.08	0.54 ± 0.07	−25.09 ± 0.21	−26.17 ± 0.18	43.55 ± 0.08	43.59 ± 0.07	0.18
SDSS J120942.22+320258.8	182.4259	32.0496	0.05898	0.70 ± 0.02	1.01 ± 0.02	−24.34 ± 0.03	−25.22 ± 0.02	43.25 ± 0.01	43.21 ± 0.01	0.13
SDSS J121130.30+404743.2	182.8762	40.7953	0.34779	0.75 ± 0.03	0.88 ± 0.11	−26.45 ± 0.04	−27.42 ± 0.10	44.10 ± 0.02	44.09 ± 0.04	0.17
SDSS J121457.41+101418.1	183.7392	10.2383	0.14583	0.91 ± 0.03	1.40 ± 0.21	−24.77 ± 0.03	−25.79 ± 0.10	43.42 ± 0.01	43.44 ± 0.04	0.24
SDSS J121825.51+295154.8	184.6062	29.8652	0.13559	0.85 ± 0.04	1.39 ± 0.08	−24.73 ± 0.05	−25.95 ± 0.05	43.41 ± 0.02	43.50 ± 0.02	0.02
SDSS J121907.89+051645.6	184.7828	5.27933	0.08251	1.12 ± 0.04	1.64 ± 0.07	−24.03 ± 0.03	−25.05 ± 0.03	43.13 ± 0.01	43.14 ± 0.01	0.04
SDSS J122823.86+361729.0	187.0994	36.2913	0.13369	0.86 ± 0.02	1.28 ± 0.10	−24.58 ± 0.03	−25.50 ± 0.05	43.35 ± 0.01	43.32 ± 0.02	0.09
SDSS J123852.87+081512.0	189.7202	8.25333	0.11378	0.68 ± 0.03	1.04 ± 0.02	−24.40 ± 0.03	−25.48 ± 0.03	43.28 ± 0.01	43.31 ± 0.01	0.15
SDSS J124255.36+253727.9	190.7306	25.6244	0.08789	0.58 ± 0.03	1.15 ± 0.09	−23.00 ± 0.05	−24.12 ± 0.07	42.72 ± 0.02	42.77 ± 0.03	0.05
SDSS J124521.42−014735.4	191.3392	−1.7931	0.21543	0.37 ± 0.05	0.78 ± 0.08	−24.56 ± 0.17	−26.06 ± 0.10	43.34 ± 0.07	43.55 ± 0.04	0.05
SDSS J130355.93+220338.7	195.9830	22.0607	0.09601	0.38 ± 0.04	0.52 ± 0.07	−23.80 ± 0.10	−24.52 ± 0.12	43.03 ± 0.04	42.93 ± 0.05	0.13
SDSS J130532.91+395337.9	196.3871	39.8938	0.07249	0.67 ± 0.02	1.08 ± 0.04	−23.78 ± 0.03	−24.67 ± 0.03	43.03 ± 0.01	42.99 ± 0.01	0.05
SDSS J130815.57+042909.6	197.0648	4.48600	0.04832	0.35 ± 0.03	0.71 ± 0.05	−22.81 ± 0.08	−23.76 ± 0.06	42.64 ± 0.03	42.63 ± 0.02	0.01
SDSS J131022.77+251809.2	197.5948	25.3025	0.16039	0.55 ± 0.04	0.64 ± 0.08	−24.59 ± 0.08	−25.57 ± 0.11	43.35 ± 0.03	43.35 ± 0.04	0.03
SDSS J131509.34+072737.6	198.7889	7.46044	0.09182	0.66 ± 0.02	0.95 ± 0.04	−24.77 ± 0.03	−25.56 ± 0.03	43.42 ± 0.01	43.35 ± 0.01	0.05
SDSS J132259.94+330121.9	200.7497	33.0227	0.12690	0.35 ± 0.02	0.65 ± 0.03	−24.20 ± 0.06	−25.35 ± 0.05	43.19 ± 0.02	43.26 ± 0.02	0.08
SDSS J132848.45+275227.8	202.2018	27.8743	0.09114	0.60 ± 0.05	0.81 ± 0.07	−24.22 ± 0.06	−25.16 ± 0.07	43.20 ± 0.03	43.19 ± 0.03	0.04
SDSS J132902.05+234108.4	202.2585	23.6856	0.07171	0.55 ± 0.03	1.32 ± 0.04	−23.08 ± 0.06	−24.60 ± 0.03	42.75 ± 0.02	42.96 ± 0.01	0.13
SDSS J133212.62+203637.9	203.0525	20.6105	0.11249	1.16 ± 0.01	1.58 ± 0.03	−25.48 ± 0.02	−26.48 ± 0.02	43.71 ± 0.01	43.71 ± 0.01	0.22
SDSS J133731.36+003528.8	204.3806	0.59133	0.29881	0.72 ± 0.09	0.74 ± 0.05	−27.36 ± 0.09	−28.23 ± 0.05	44.46 ± 0.04	44.42 ± 0.02	0.12
SDSS J134032.49+184218.6	205.1353	18.7051	0.09018	0.37 ± 0.06	0.65 ± 0.07	−22.76 ± 0.14	−23.81 ± 0.10	42.62 ± 0.06	42.64 ± 0.04	0.08
SDSS J134105.98−004902.4	205.2749	−0.8173	0.17538	0.61 ± 0.05	0.66 ± 0.08	−25.43 ± 0.08	−26.25 ± 0.10	43.69 ± 0.03	43.62 ± 0.04	0.09
SDSS J134123.20+151650.4	205.3466	15.2806	0.12553	0.39 ± 0.03	0.72 ± 0.04	−23.87 ± 0.10	−25.16 ± 0.05	43.06 ± 0.04	43.19 ± 0.02	0.12
SDSS J134849.38+155902.0	207.2057	15.9838	0.18237	0.83 ± 0.05	1.11 ± 0.05	−25.83 ± 0.07	−26.85 ± 0.06	43.85 ± 0.03	43.86 ± 0.02	0.11
SDSS J135241.36+000925.8	208.1723	0.15716	0.16596	0.37 ± 0.04	0.60 ± 0.04	−24.25 ± 0.12	−25.40 ± 0.07	43.22 ± 0.05	43.28 ± 0.03	0.20

Table 1
(Continued)

Name	R.A.	Decl.	z	ΔW1 (mag)	ΔW2 (mag)	W1m (mag)	W2m (mag)	L_{W1} (erg s^{-1})	L_{W2} (erg s^{-1})	Δd (arcsec)
(1)	(2)	(3)	(4)	(5)	(6)	(7)	(8)	(9)	(10)	(11)
SDSS J140221.26+392212.3	210.5885	39.3700	0.06375	1.65 ± 0.01	2.15 ± 0.04	-24.97 ± 0.01	-25.73 ± 0.01	43.50 ± 0.00	43.42 ± 0.00	0.22
SDSS J140648.43+062834.8	211.7017	6.47633	0.08499	0.35 ± 0.01	0.70 ± 0.03	-24.10 ± 0.04	-25.28 ± 0.04	43.16 ± 0.02	43.23 ± 0.01	0.13
SDSS J140950.27+105740.2	212.4594	10.9611	0.05972	0.19 ± 0.02	0.54 ± 0.05	-23.06 ± 0.14	-24.65 ± 0.08	42.74 ± 0.06	42.98 ± 0.03	0.15
SDSS J141235.89+411458.5	213.1495	41.2495	0.10250	0.34 ± 0.02	0.54 ± 0.03	-23.73 ± 0.06	-24.48 ± 0.07	43.00 ± 0.02	42.91 ± 0.03	0.08
SDSS J142254.11+060953.4	215.7254	6.16483	0.05636	0.77 ± 0.02	1.23 ± 0.02	-24.85 ± 0.03	-25.67 ± 0.01	43.45 ± 0.01	43.39 ± 0.00	0.19
SDSS J142420.78+624916.5	216.0865	62.8212	0.10913	0.41 ± 0.04	0.59 ± 0.02	-24.27 ± 0.09	-25.06 ± 0.03	43.22 ± 0.03	43.15 ± 0.01	0.05
SDSS J142808.89−023124.8	217.0370	−2.5235	0.05207	0.37 ± 0.07	0.50 ± 0.13	-21.67 ± 0.18	-22.68 ± 0.30	42.18 ± 0.07	42.19 ± 0.12	0.03
SDSS J143016.05+230344.4	217.5668	23.0623	0.08105	0.56 ± 0.01	0.74 ± 0.05	-24.94 ± 0.03	-25.69 ± 0.06	43.49 ± 0.01	43.40 ± 0.02	0.02
SDSS J144024.32+175852.7	220.1013	17.9813	0.11574	0.43 ± 0.04	0.54 ± 0.07	-22.73 ± 0.15	-23.84 ± 0.13	42.61 ± 0.06	42.66 ± 0.05	0.03
SDSS J144227.57+555846.3	220.6148	55.9795	0.07689	1.39 ± 0.02	1.79 ± 0.03	-26.07 ± 0.01	-26.86 ± 0.01	43.94 ± 0.00	43.86 ± 0.00	0.04
SDSS J144758.41+402335.8	221.9933	40.3932	0.13025	0.89 ± 0.02	1.22 ± 0.04	-25.40 ± 0.02	-26.20 ± 0.02	43.67 ± 0.01	43.60 ± 0.01	0.05
SDSS J144829.01+113732.1	222.1208	11.6255	0.06657	0.58 ± 0.03	1.15 ± 0.02	-23.14 ± 0.05	-24.35 ± 0.02	42.77 ± 0.02	42.86 ± 0.01	0.23
SDSS J150440.39+010735.0	226.1682	1.12638	0.12826	0.61 ± 0.03	0.61 ± 0.03	-26.39 ± 0.04	-27.24 ± 0.04	44.07 ± 0.02	44.02 ± 0.02	0.11
SDSS J150844.22+260249.1	227.1842	26.0469	0.08255	0.28 ± 0.03	0.73 ± 0.06	-22.47 ± 0.13	-24.12 ± 0.07	42.50 ± 0.05	42.77 ± 0.03	0.11
SDSS J151117.94+221428.2	227.8247	22.2411	0.12048	0.37 ± 0.04	0.64 ± 0.05	-24.11 ± 0.10	-25.36 ± 0.07	43.16 ± 0.04	43.27 ± 0.03	0.08
SDSS J151257.18+280937.5	228.2382	28.1604	0.11552	0.28 ± 0.03	0.67 ± 0.04	-23.19 ± 0.12	-24.61 ± 0.06	42.79 ± 0.05	42.97 ± 0.02	0.01
SDSS J151345.76+311125.0	228.4406	31.1902	0.07181	0.81 ± 0.01	1.16 ± 0.03	-24.21 ± 0.02	-25.01 ± 0.02	43.20 ± 0.01	43.13 ± 0.01	0.01
SDSS J152438.13+531458.7	231.1588	53.2496	0.08513	0.67 ± 0.05	0.85 ± 0.05	-23.21 ± 0.06	-23.97 ± 0.05	42.80 ± 0.02	42.71 ± 0.02	0.10
SDSS J153151.41+372445.9	232.9642	37.4127	0.02990	1.43 ± 0.04	1.84 ± 0.10	-21.37 ± 0.03	-22.24 ± 0.03	42.06 ± 0.01	42.02 ± 0.01	0.99
SDSS J153310.02+272920.2	233.2917	27.4889	0.07193	0.53 ± 0.07	0.69 ± 0.09	-24.52 ± 0.13	-25.53 ± 0.10	43.32 ± 0.05	43.33 ± 0.04	0.03
SDSS J153711.29+581420.2	234.2970	58.2389	0.09356	1.28 ± 0.08	1.47 ± 0.11	-25.18 ± 0.04	-26.04 ± 0.04	43.59 ± 0.01	43.54 ± 0.02	0.06
SDSS J154029.29+005437.2	235.1220	0.91033	0.01172	0.37 ± 0.06	0.62 ± 0.11	-17.76 ± 0.16	-18.79 ± 0.17	40.62 ± 0.06	40.64 ± 0.07	0.63
SDSS J154158.63+071836.4	235.4942	7.31011	0.16305	0.42 ± 0.05	0.79 ± 0.11	-23.92 ± 0.11	-25.08 ± 0.12	43.08 ± 0.04	43.16 ± 0.05	0.06
SDSS J154843.06+220812.6	237.1794	22.1368	0.03127	2.12 ± 0.02	2.90 ± 0.04	-24.00 ± 0.01	-24.91 ± 0.01	43.12 ± 0.00	43.09 ± 0.00	0.01
SDSS J154955.19+332752.0	237.4799	33.4644	0.08565	1.44 ± 0.04	2.09 ± 0.05	-24.29 ± 0.02	-25.20 ± 0.02	43.23 ± 0.01	43.20 ± 0.01	0.03
SDSS J155437.26+525526.4	238.6552	52.9240	0.06644	0.71 ± 0.01	1.32 ± 0.01	-23.62 ± 0.01	-24.76 ± 0.01	42.96 ± 0.00	43.03 ± 0.00	0.11
SDSS J155438.39+163637.6	238.6599	16.6104	0.00798	0.60 ± 0.05	1.03 ± 0.12	-17.63 ± 0.07	-18.47 ± 0.08	40.56 ± 0.03	40.51 ± 0.03	0.83
SDSS J155440.25+362952.0	238.6677	36.4977	0.23683	0.76 ± 0.04	1.01 ± 0.16	-25.91 ± 0.04	-26.80 ± 0.11	43.88 ± 0.02	43.84 ± 0.04	0.11
SDSS J155539.95+212005.7	238.9164	21.3349	0.07094	0.51 ± 0.02	1.05 ± 0.04	-23.39 ± 0.05	-24.79 ± 0.03	42.87 ± 0.02	43.04 ± 0.01	0.08
SDSS J155640.32+451338.4	239.1680	45.2273	0.18083	0.64 ± 0.07	0.86 ± 0.08	-24.88 ± 0.09	-25.95 ± 0.07	43.47 ± 0.04	43.50 ± 0.03	0.04
SDSS J155743.52+272753.0	239.4313	27.4647	0.03156	0.28 ± 0.01	0.79 ± 0.01	-22.62 ± 0.05	-24.30 ± 0.02	42.56 ± 0.02	42.84 ± 0.01	0.03
SDSS J160052.26+461242.9	240.2177	46.2119	0.19742	0.32 ± 0.02	0.62 ± 0.04	-24.72 ± 0.07	-25.93 ± 0.06	43.40 ± 0.03	43.49 ± 0.03	0.05
SDSS J161258.17+141617.5	243.2423	14.2715	0.07200	0.29 ± 0.02	0.57 ± 0.03	-22.10 ± 0.08	-23.58 ± 0.06	42.35 ± 0.03	42.56 ± 0.03	0.09
SDSS J162034.99+240726.5	245.1457	24.1240	0.06551	1.31 ± 0.04	1.64 ± 0.05	-24.17 ± 0.02	-24.80 ± 0.02	43.18 ± 0.01	43.04 ± 0.01	0.14
SDSS J162810.03+481047.7	247.0417	48.1799	0.12454	0.25 ± 0.03	0.58 ± 0.05	-22.93 ± 0.12	-24.34 ± 0.09	42.69 ± 0.05	42.86 ± 0.03	0.12
SDSS J163246.84+441618.5	248.1951	44.2718	0.05789	0.49 ± 0.01	0.91 ± 0.02	-23.06 ± 0.03	-23.99 ± 0.02	42.74 ± 0.01	42.72 ± 0.01	0.01
SDSS J164754.38+384342.0	251.9765	38.7283	0.08547	1.14 ± 0.02	1.68 ± 0.06	-23.99 ± 0.02	-24.91 ± 0.02	43.11 ± 0.01	43.09 ± 0.01	0.05
SDSS J165726.81+234528.1	254.3617	23.7578	0.05914	2.96 ± 0.03	3.59 ± 0.05	-25.52 ± 0.01	-26.69 ± 0.01	43.72 ± 0.00	43.80 ± 0.00	0.05
SDSS J165922.65+204947.4	254.8443	20.8298	0.04513	0.17 ± 0.02	0.60 ± 0.02	-22.78 ± 0.11	-24.44 ± 0.04	42.63 ± 0.04	42.90 ± 0.01	0.05
SDSS J211529.89−001107.0	318.8745	−0.1852	0.23285	0.55 ± 0.06	0.77 ± 0.07	-25.07 ± 0.11	-25.96 ± 0.09	43.54 ± 0.04	43.51 ± 0.03	0.06
SDSS J214142.90−085702.3	325.4287	−8.9506	0.08729	0.45 ± 0.04	0.76 ± 0.05	-23.29 ± 0.09	-24.38 ± 0.06	42.83 ± 0.04	42.88 ± 0.02	0.12

Table 1
(Continued)

Name	R.A.	Decl.	z	ΔW1 (mag)	ΔW2 (mag)	W1m (mag)	W2m (mag)	L_{W1} (erg s^{-1})	L_{W2} (erg s^{-1})	Δd (arcsec)
(1)	(2)	(3)	(4)	(5)	(6)	(7)	(8)	(9)	(10)	(11)
SDSS J214603.88+104128.6	326.5161	10.6912	0.16358	0.60 ± 0.05	0.82 ± 0.08	-24.61 ± 0.07	-25.46 ± 0.08	43.36 ± 0.03	43.31 ± 0.03	0.11
SDSS J215055.73−010654.1	327.7322	−1.1150	0.08791	1.87 ± 0.12	1.90 ± 0.11	-24.29 ± 0.05	-25.00 ± 0.03	43.23 ± 0.02	43.12 ± 0.01	0.03
SDSS J215648.45+004110.6	329.2018	0.68627	0.05389	0.20 ± 0.02	0.51 ± 0.02	-22.14 ± 0.12	-23.64 ± 0.05	42.37 ± 0.05	42.58 ± 0.02	0.11
SDSS J220349.23+112433.0	330.9551	11.4091	0.18627	0.95 ± 0.02	1.52 ± 0.09	-25.58 ± 0.03	-26.63 ± 0.04	43.75 ± 0.01	43.78 ± 0.02	0.08
SDSS J221541.60−010721.0	333.9233	−1.1225	0.04775	0.27 ± 0.03	0.65 ± 0.05	-22.59 ± 0.10	-23.82 ± 0.08	42.55 ± 0.04	42.65 ± 0.03	0.26
SDSS J231055.38+222008.5	347.7307	22.3356	0.07829	0.25 ± 0.02	0.50 ± 0.05	-22.97 ± 0.06	-24.10 ± 0.09	42.70 ± 0.03	42.76 ± 0.03	0.02
SDSS J231222.78+133538.8	348.0949	13.5941	0.16553	0.36 ± 0.05	0.60 ± 0.05	-24.09 ± 0.14	-25.17 ± 0.09	43.15 ± 0.06	43.19 ± 0.04	0.02
SDSS J232452.26+154251.0	351.2177	15.7141	0.15109	0.75 ± 0.02	0.88 ± 0.06	-25.15 ± 0.03	-25.97 ± 0.08	43.58 ± 0.01	43.51 ± 0.03	0.04

Note. Column (1): SDSS name. Columns (2)–(4): R.A., decl., and redshift given by SDSS. Columns (5) and (6): amplitudes of variability in the W1 and W2 bands. Columns (7) and (8): peak absolute magnitude in W1 and W2. Columns (9) and (10): peak monochromatic luminosity of W1 and W2. Column (11): offset distance between the maximum outburst epoch and the quiescent state.

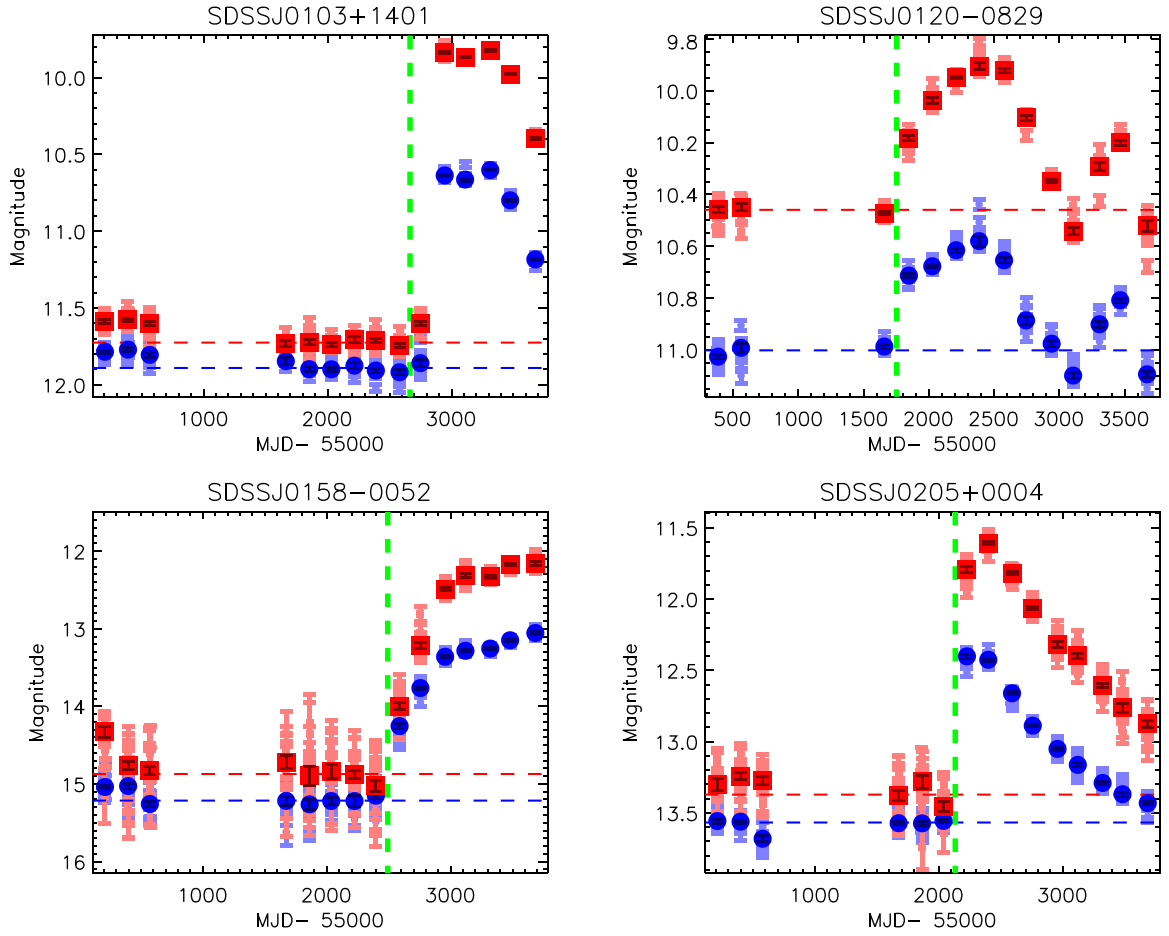

Figure 2. Similar to Figure 1, we show the WISE light curves of four representative outburst galaxies in our MIRONG sample. The estimated magnitudes at the quiescent phase are shown with dashed blue and red lines. The vertical green dashed lines mark the boundary of the quiescent and outburst stage. Object SDSS J0103+1401 shows very fast rising followed by a relatively stable high state, in contrast with SDSS J0205+0004, which also displays fast rising but immediate declining. The other two objects show slower rising, in which SDSS J0120–0829 has manifested itself as a complete flare in terms of both rising and declining (Sun et al. 2020).

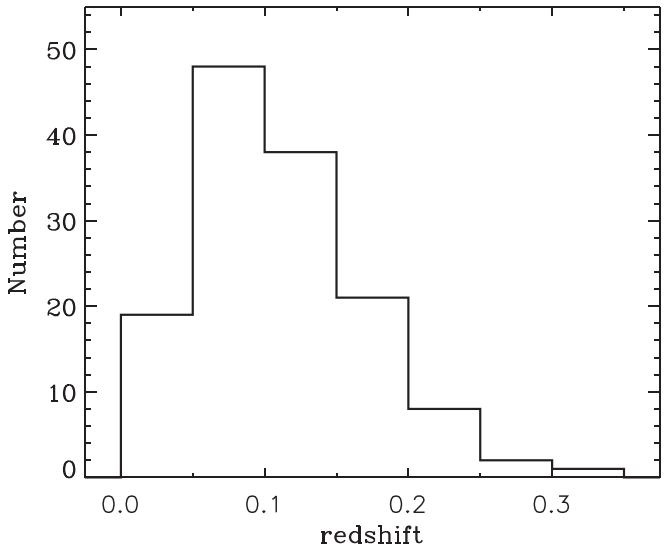

Figure 3. Histogram of the redshift of our sample.

data. The combined data give *V*-band light curves spanning from 2005 to 2018. We did not find any optical flares, implying the faintness of optical emission for most, if not all, MIR burst galaxies.

3.2. Constraints on the Physical Position of MIR Flares

The specific locations in the galactic region of the MIR flares can give us strong clues to their nature. For example, an outburst offset from the galactic center can be convincingly classified as an SN. Otherwise, the central SMBHs might be considered as the most likely origin.

The astrometry of the WISE catalog has been reconstructed with respect to the 2MASS Point Source Catalog reference frame. The rms error of the position is found to be less than $0\farcs5$ for sources with $S/N > 20$ in at least one WISE band, where the noise includes flux errors due to zodiacal foreground emission, instrumental effects, source photon statistics, and neighboring sources.[12] The WISE PSF profile-fit photometry we used is measured at the intensity-weighted center, so the variation of the center position can tell us whether or not the outburst is far away from the preoutburst galactic center. For instance, when an off-centered SN has exploded and is MIR-bright, there should be a positional offset between the WISE photometric center of its host galaxy and the intensity-weighted center determined by the SN outburst.

To test whether significant positional offsets exist, we have calculated the mean photometric center (R.A., decl.) given by the ALLWISE and NEOWISE-R catalogs at the quiescent state

[12] http://wise2.ipac.caltech.edu/docs/release/allsky/expsup/sec6_4.html

Table 2
Optical Counterparts

Galaxy (1)	Transient (2)	Date (3)	Offset (4)	AT Designation (5)	Classification (6)
SDSS J0045−0047	PS16dsp	2016-08-03	0.39	AT2016ezq	⋯
SDSS J0158−0052	PS16dtm	2016-08-12	0.16	SN2016ezh	TDE
SDSS J0841+0526	ATLAS17nvk	2017-11-15	<0.5[a]	AT2017jdg	⋯
SDSS J0854+1113	GNT	2016-09-26	<0.5[a]	⋯	⋯
SDSS J0915+4814	ZTF18aaidlyq	2018-11-03	0.13	AT2018ivp	Turn-on AGN
SDSS J0936+0615	ASASSN-18xl	2018-10-09	2.93	SN2018hfm	SN
SDSS J1133+6701	ZTF18aasuray	2018-05-10	0.09	AT2018cdp	Turn-on AGN
SDSS J1332+2036	CRTS_OBC	2015-03-29	⋯	⋯	⋯
SDSS J1531+3724	ASASSN-17jq	2017-07-25	1.93	AT2017fra	SN
SDSS J1533+2729	ATLAS18mtv	2017-12-30	0.27	AT2017kav	⋯
SDSS J1540+0054	ASASSN-16eh	2016-04-10	1.20	SN2016blz	SN
SDSS J1554+1636	ASASSN-15bd	2015-01-17	1.00	⋯	SN
SDSS J1554+3629	iPTF16bco	2016-06-01	0.44	⋯	Turn-on AGN
SDSS J1620+2407	ATLAS17jrp	2017-08-03	0.00	AT2017gge	TDE candidate
SDSS J1647+3843	GNT	2017-06-10	<0.5[a]	⋯	⋯

Notes. Column (1): SDSS abbreviated name of the galaxy. Column (2): transient named by the discovering surveys. Column (3): optical discovery date. Column (4): distance to the galactic center in units of arcseconds. Column (5): designation on the transient name server. Column (6): classified nature of the transients.
[a] The precise offset is unknown but should be $<0\farcs5$ because of the selection criteria of the Gaia nuclear transient (Kostrzewa-Rutkowska et al. 2018).

and that from the maximum outburst epoch, respectively. We defined the angular distance between them as the offset distance (Δd, in units of arcseconds). The distribution of Δd is presented in Figure 4. The majority of our galaxies show very small Δd with a median value of $0\farcs08$. We noticed that only the four known SNe (see Section 3.1) have Δd larger than $0\farcs5$ ($1\farcs48$, $0\farcs99$, $0\farcs63$, and $0\farcs83$), which is expected, since their optical offsets are known as large as $2\farcs93$, $1\farcs93$, $1\farcs20$, and $1\farcs00$, respectively. This demonstrates that checking for the shift of photometric center appears effective in recognizing a candidate outburst located more than $1''$ from the nucleus.

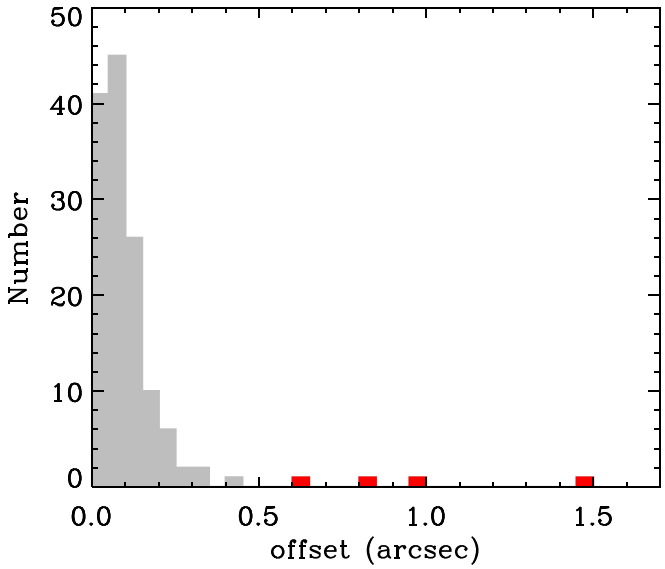

Figure 4. Histogram of center offset distance (Δd) in units of arcseconds, defined as the angular distance of the photometric center at the maximum and quiescent epochs. The Δd of SNe (highlighted in red) are all larger than $0\farcs5$, in contrast with the tiny values of other objects (median $0\farcs08$).

3.3. The MIR Light Curves

Since the bulk of our MIR flares have no informed optical counterparts, we instead try to characterize their properties by the MIR light curves themselves. The whole sample has brightened by average 0.63 (median 0.53) and 0.96 (0.79) magnitudes in W1 and W2, respectively, indicating that the variability amplitude at the W2 band is overall larger than W1. In other words, the W1–W2 color displays a trend of redder when brighter (RWB; see Figure 5) with a median Δ(W1–W2) = 0.33. Only two Seyfert galaxies (SDSS J0811+4054 and SDSS J1029+2526) show the color changes in an opposite way. The RWB evolution is consistent with the scenario found in CL AGNs, indicating a higher hot dust contribution than the starlight-dominated quiescent state when the AGN activity becomes stronger (e.g., Sheng et al. 2017; Yang et al. 2018).

In order to further investigate the properties of the MIR outbursts, we subtracted the background emission from the light curves in the flare state (Section 2.4). The background-subtracted W2 absolute magnitude ($W2_m$) is presented in Figure 6, with the majority (95.6%, 131 out of 137) ranging from −22.5 to −27, corresponding to the logarithmic monochromatic luminosity ($\log L_{W2}$) between 42 and 44. It is conspicuous that while the low-luminosity outliers ($W2_m \gtrsim -22.5$ or $\log L_{W2} \lesssim 42$) are all SNe, the radio-loud AGNs (see Section 6.2) dominate at the high-luminosity end. We stress that the minimum absolute magnitudes (or maximum luminosity) do not always tell us the true peak, since some of them are still rising in the light curves. If we naively suppose that the MIR outburst started from the middle between the first brightening data point and the quiescent state, the median rising timescale to the (current) peak is 429 days, or 398 days in the rest-frame of galaxies.

3.4. Dust Properties

In this subsection, we try to acquire more physical quantities by fitting the MIR emission with the dust thermal emission scenario. For dust grains with size distribution $N(a)$ (a is the radius of the grain sphere), density ρ, and absorption coefficient Q_ν at a luminosity distance d_L, the observed monochromatic

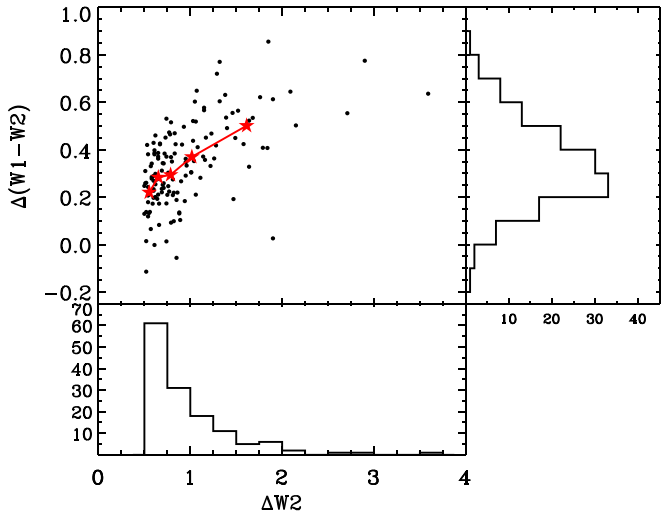

Figure 5. Color variation Δ(W1–W2) vs. W2 variability amplitude (ΔW2) of the MIR outburst galaxies. The histograms of Δ(W1–W2) and ΔW2 are shown in the right and bottom panels, respectively. We have divided the whole sample into five equal-sized subsamples sorted by ΔW2 and plotted the median Δ(W1–W2) of each subsample as red stars. The MIR variability shows an overall trend of RWB.

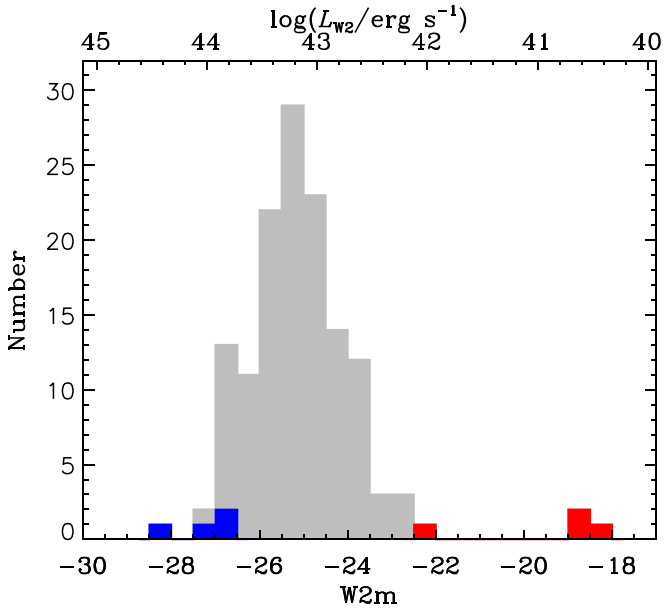

Figure 6. Histogram of peak absolute W2 magnitude. We plot the confirmed SNe in red and radio-loud AGNs in blue.

flux at a given frequency can be calculated as (see also Wang et al. 2019)

$$f_\nu = \frac{1}{4\pi d_L^2}\int_a^{a_{\max}} N(a)4\pi a^2 Q_\nu(a)\pi B_\nu(T)\,\mathrm{da} = \frac{3M_d}{4\rho d_L^2}\left\langle\frac{Q_\nu}{a}\right\rangle B_\nu(T), \quad (1)$$

where

$$\left\langle\frac{Q_\nu}{a}\right\rangle = \frac{\int_a^{a_{\max}} N(a)a^3(Q/a)\mathrm{da}}{\int_a^{a_{\max}} N(a)a^3\mathrm{da}}; \quad (2)$$

$$M_{\rm d} = \int_a^{a_{\max}} N(a)\rho\frac{4}{3}\pi a^3\mathrm{da}. \quad (3)$$

For simplicity, we assume that the dust grains follow an MRN size distribution (Mathis et al. 1977; see also Draine & Lee 1984) as $N(a)\propto a^{-3.5}$ with $a = 0.01\mu$m, $a_{\max} = 10\mu$m and an average density of $\rho = 2.7\ \mathrm{g\ cm^{-3}}$ for silicate grains.

We begin the fit with blackbody model ($Q_\nu = 1$). However, the real dust emission is not a perfect blackbody, and the absorption coefficient should be considered. We adopt the silicate absorption coefficients in Laor & Draine (1993), which gives $\left\langle\frac{Q_\nu}{a}\right\rangle = 0.214$ and 0.177 in W1 and W2, respectively. The fluxes in W1 and W2 are then fitted with the modified blackbody model to derive the dust temperature (T_d) and mass (M_d). The luminosity is comparable to that obtained with a simple blackbody model, while the T_d is systematically lower and M_d is about 1 order of magnitude higher (see Figure 7). We note that the T_d values are all below 1500 K, in agreement with the suppression of the sublimation temperature of silicate and graphite grains (Barvainis 1987; Mor & Netzer 2012). All of the blackbody parameters to describe the dust emission at the epoch of luminosity maximum can be found in Table 3, and their distributions are presented in Figure 7.

We then attempted to estimate the distance of dust emission (R_d) to the central radiation source. By assuming spherical symmetry for the dust distribution, the distance of dust emission can be expressed by

$$R_d = \left(\frac{L_{\rm d}}{4\pi\sigma T_d^4}\right)^{1/2}. \quad (4)$$

As the dust distribution is uncertain, the above estimation may be oversimplified but can be treated as a strict lower limit on the scale of dust distribution (median value of 0.06 pc). In reality, the dust might not fully cover the central radiation source. If the dust covering factor is f_d (with unity as complete coverage), the corresponding distance should be increased by a factor of $f_d^{-1/2}$. Likewise, the R_d for the case of the modified blackbody model would also be larger, yielding a median value of 0.20 pc ($f_d = 1$) that is scaled by the dust mass. Alternatively, the MIR rising timescale can also be used as a distance indicator of the dust responsible for the peak emission. In this way, we obtain a median value of 0.34 pc given the median rest-frame rising timescale of 398 days. The $f_d = 0.04$ (or $f_d = 0.34$) from the blackbody (or modified blackbody) fit can generally reproduce the observed rising timescale. Above all, we may conclude that the dust is located at the order of 0.1 pc (see distribution in panel (d) of Figure 7) with a covering factor at the order of 0.1.

4. Event Rate and Luminosity Function

4.1. Event Rate Estimation

Regardless of their physical nature, we try to estimate the event rate of the MIRONG selected by us in the same manner used in Wang et al. (2018). The accumulative number is roughly proportional to the comoving volume up to $z\sim 0.09$; then the increase rate becomes slower and finally flattens (see Figure 8). This suggests that the sample can be taken as almost complete at $z < 0.09$ but is obviously underrepresentative at $z > 0.09$ if there is no evident redshift evolution in the event

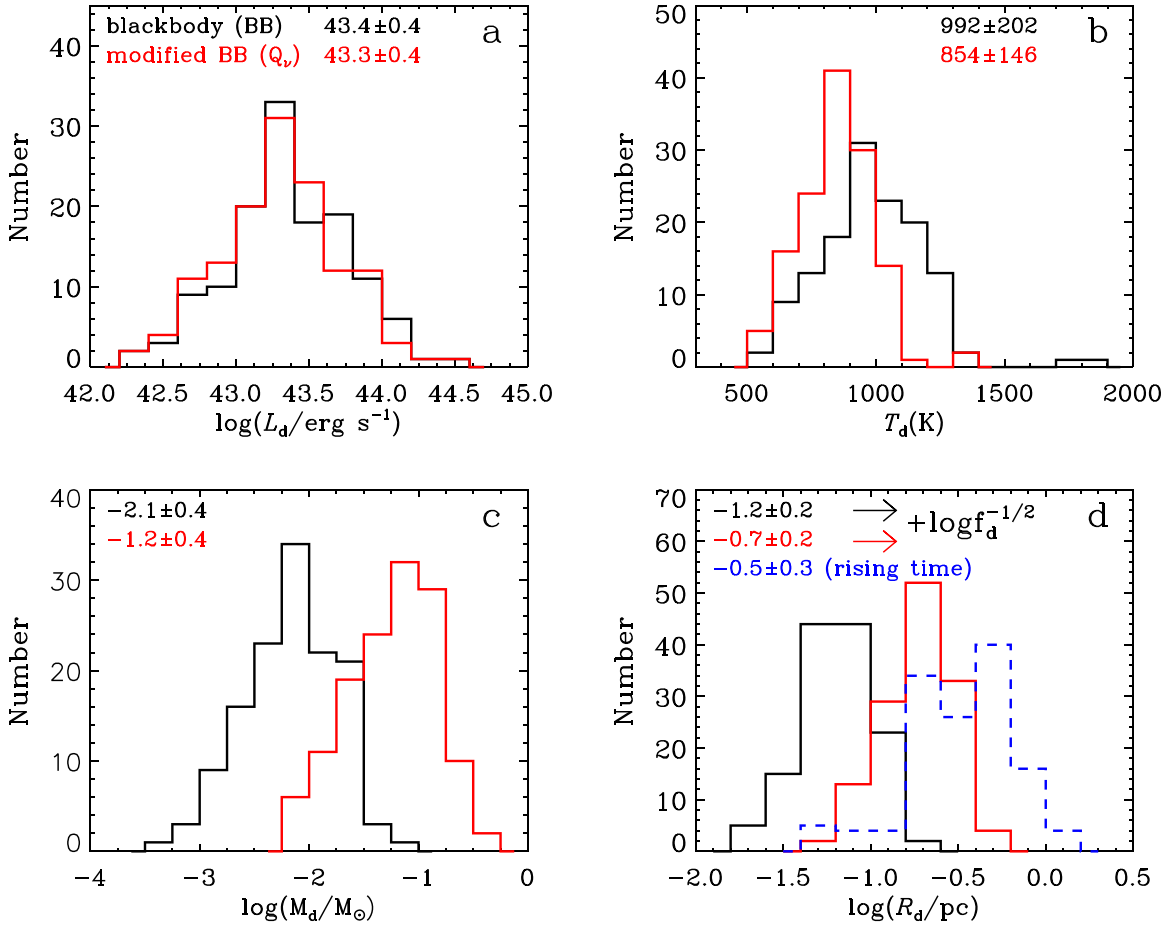

Figure 7. Histograms of the fitted dust luminosity (panel (a)), temperature (b), mass (c), and distance to the heating source (d). All parameters are derived at the W2 maximum epoch. The black line represents the pure blackbody case, while the red shows the fitting with dust absorption efficiency taken into consideration. The numbers indicated in the panels are the medians and standard deviations of the distributions. The four SN sources have not been shown in the plots, as they are outliers in the low end whose values can be retrieved in Table 3. For the dust distance (panel (d)), we have also overplotted the distance given by the rising timescale of the WISE light curves (blue dashed line). The arrows indicate that the black and red histograms will shift by $\log f_d^{-1/2}$ if the real dust covering factor (f_d) is not unity.

rate. There are 61 objects at $z < 0.09$, yielding a density of $1.2 \times 10^{-6}\,\mathrm{Mpc}^{-3}$ in the SDSS sky region.

On the other hand, we note that the SDSS main galaxy surveys are originally designed to target galaxies with dereddened r-band magnitudes brighter than 17.77 (Strauss et al. 2002). The cut ensures that galaxies with r-band absolute magnitudes of $M_r < -19.5$ are complete, which corresponds to the luminosity range for most galaxies in our sample (Figure 11). Considering only galaxies with $M_r < -19.5$ at $z < 0.09$ will result in a density of $2.2 \times 10^{-4}\,\mathrm{galaxy}^{-1}$. Since our sample selection requires a brightening phase in the NEOWISE stage (spanning 5 yr) and an average rising timescale of about 1 yr, the event rate should be divided by a factor of 4 to obtain the rate per year. The final event rate is about $5.4 \times 10^{-5}\,\mathrm{galaxy}^{-1}\,\mathrm{yr}^{-1}$, and the corresponding density rate is $3.0 \times 10^{-7}\,\mathrm{Mpc}^{-3}\,\mathrm{yr}^{-1}$, which is basically consistent with the $10^{-7}\,\mathrm{Mpc}^{-3}\,\mathrm{yr}^{-1}$ given by Wang et al. (2018).

4.2. Peak Luminosity Function

We use the $V/V_{\max}$ method (Schmidt 1968; Eales 1993) to calculate the MIR peak luminosity function of the outburst. The formula is adopted as follows:

$$\Phi(L)\mathrm{dL} = \sum_{L_i \in [L-\Delta L/2, L+\Delta L/2]} \frac{1}{V_{\max} f_{\mathrm{comp}}}. \quad (5)$$

Here $V_{\max}$ is the maximum comoving volume within which the galaxy of interest is detectable at a given depth. Taking 17.77 and 14.5 as the limiting magnitude at the r band and W2, respectively, we computed the $V_{\max}$ for each target. In its simplest form, $\Phi(L)$ is the sum of $1/V_{\max}$ for all objects in each luminosity bin. The limiting magnitude of 14.5 at the W2 band is determined from our cut $W2\,\mathrm{min} < 14$ and a brightening amplitude of >0.5 mag (see Section 2.3), which is verified by the magnitude–redshift distribution of the final MIRONG sample (see Figure 9). Here f_{comp} is the completeness for sources located in the SDSS footprint that have been spectroscopically observed. The spectroscopic effective area of the SDSS DR14 catalog is 9376 deg^2 (the full sky is 41,252.96 deg^2), and about 92.8% of the galaxies at $r < 17.77$ have been included in the main galaxy sample (Lazo et al. 2018); thus, $f_{\mathrm{comp}} = \frac{0.928 \times 9376}{41252.96} = 0.211$.

The luminosity function in log–log space with log L_{W2} bin 0.5 is shown in Figure 10. We estimate the statistical errors using the bootstrap method. To this end, we generate $N = 1000$ bootstrap samples, each of which consists of objects picked randomly from the original sample. The errors are then given by the standard deviation in the distribution of Φ measured from the bootstrap samples. The Schechter function is typically

Table 3
The Fitted Dust Parameters

Name	$T_{\rm bb}$ (K)	$\log L_{\rm bb}$ (erg s^{-1})	$\log M_{\rm bb}$ ($M_\odot$)	$\log R_{\rm bb}$ (pc)	T_d (K)	$\log L_d$ (erg s^{-1})	$\log M_d$ ($M_\odot$)	$\log R_d$ (pc)
(1)	(2)	(3)	(4)	(5)	(6)	(7)	(8)	(9)
SDSS J0000+1438	901 ± 40	43.41 ± 0.09	−2.01 ± 0.12	−1.12 ± 0.09	794 ± 31	43.37 ± 0.09	−1.07 ± 0.11	−0.65 ± 0.12
SDSS J0027+0713	995 ± 50	43.24 ± 0.10	−2.35 ± 0.14	−1.29 ± 0.10	865 ± 37	43.20 ± 0.10	−1.39 ± 0.13	−0.81 ± 0.14
SDSS J0045−0047	996 ± 129	42.45 ± 0.25	−3.14 ± 0.34	−1.69 ± 0.24	857 ± 93	42.42 ± 0.25	−2.20 ± 0.31	−1.22 ± 0.33
SDSS J0103+1401	961 ± 22	43.79 ± 0.04	−1.74 ± 0.06	−0.98 ± 0.04	829 ± 16	43.76 ± 0.04	−0.81 ± 0.05	−0.52 ± 0.06
SDSS J0120−0829	998 ± 27	43.29 ± 0.05	−2.31 ± 0.07	−1.27 ± 0.05	855 ± 20	43.25 ± 0.04	−1.37 ± 0.06	−0.80 ± 0.07
SDSS J0121+1405	727 ± 29	43.25 ± 0.11	−1.80 ± 0.13	−1.01 ± 0.10	657 ± 24	43.20 ± 0.11	−0.90 ± 0.13	−0.56 ± 0.14
SDSS J0158−0052	999 ± 93	43.50 ± 0.18	−2.10 ± 0.25	−1.16 ± 0.17	862 ± 68	43.46 ± 0.18	−1.15 ± 0.23	−0.68 ± 0.24
SDSS J0205+0004	936 ± 60	43.60 ± 0.14	−1.88 ± 0.18	−1.06 ± 0.13	815 ± 45	43.57 ± 0.14	−0.94 ± 0.17	−0.59 ± 0.18
SDSS J0745+2655	879 ± 48	43.65 ± 0.11	−1.72 ± 0.14	−0.98 ± 0.10	775 ± 36	43.61 ± 0.10	−0.78 ± 0.13	−0.51 ± 0.14
SDSS J0757+1908	954 ± 48	43.19 ± 0.11	−2.33 ± 0.14	−1.28 ± 0.10	832 ± 35	43.16 ± 0.11	−1.37 ± 0.13	−0.80 ± 0.14
SDSS J0811+4054	1072 ± 39	43.60 ± 0.06	−2.13 ± 0.09	−1.18 ± 0.06	912 ± 27	43.56 ± 0.06	−1.17 ± 0.08	−0.70 ± 0.09
SDSS J0814+2611	689 ± 12	43.21 ± 0.04	−1.75 ± 0.05	−0.99 ± 0.04	623 ± 10	43.15 ± 0.04	−0.86 ± 0.05	−0.55 ± 0.05
SDSS J0814+5337	945 ± 40	43.36 ± 0.10	−2.14 ± 0.12	−1.18 ± 0.09	828 ± 30	43.33 ± 0.09	−1.18 ± 0.11	−0.70 ± 0.12
SDSS J0835+4935	864 ± 47	43.12 ± 0.09	−2.22 ± 0.13	−1.23 ± 0.10	757 ± 35	43.08 ± 0.09	−1.30 ± 0.12	−0.77 ± 0.13
SDSS J0837+4143	880 ± 47	43.34 ± 0.12	−2.04 ± 0.16	−1.13 ± 0.11	775 ± 36	43.31 ± 0.12	−1.10 ± 0.15	−0.66 ± 0.16
SDSS J0841+0526	1041 ± 39	43.65 ± 0.07	−2.02 ± 0.10	−1.13 ± 0.07	901 ± 29	43.61 ± 0.07	−1.04 ± 0.09	−0.64 ± 0.10
SDSS J0842+2357	1192 ± 50	42.86 ± 0.06	−3.05 ± 0.10	−1.64 ± 0.07	994 ± 33	42.82 ± 0.06	−2.08 ± 0.08	−1.15 ± 0.09
SDSS J0847+5142	729 ± 33	43.04 ± 0.10	−2.01 ± 0.13	−1.12 ± 0.09	657 ± 26	42.99 ± 0.10	−1.11 ± 0.12	−0.67 ± 0.13
SDSS J0854+1113	1146 ± 38	43.95 ± 0.06	−1.88 ± 0.08	−1.06 ± 0.06	979 ± 27	43.92 ± 0.05	−0.87 ± 0.07	−0.55 ± 0.08
SDSS J0858+4121	560 ± 22	42.69 ± 0.13	−1.91 ± 0.15	−1.07 ± 0.10	516 ± 19	42.62 ± 0.13	−1.06 ± 0.14	−0.65 ± 0.14
SDSS J0859+0922	1010 ± 61	43.90 ± 0.13	−1.72 ± 0.16	−0.97 ± 0.12	878 ± 45	43.86 ± 0.12	−0.74 ± 0.15	−0.48 ± 0.16
SDSS J0909+1920	729 ± 40	43.34 ± 0.14	−1.71 ± 0.17	−0.97 ± 0.12	657 ± 32	43.29 ± 0.14	−0.82 ± 0.17	−0.53 ± 0.17
SDSS J0915+4814	1177 ± 57	43.35 ± 0.08	−2.53 ± 0.12	−1.38 ± 0.09	990 ± 39	43.31 ± 0.08	−1.54 ± 0.11	−0.88 ± 0.12
SDSS J0931+6626	1012 ± 34	42.77 ± 0.07	−2.85 ± 0.09	−1.54 ± 0.06	872 ± 24	42.73 ± 0.06	−1.90 ± 0.08	−1.06 ± 0.09
SDSS J0936+0615	2541 ± 476	41.37 ± 0.17	−5.86 ± 0.37	−3.04 ± 0.26	1657 ± 179	41.16 ± 0.13	−4.81 ± 0.23	−2.51 ± 0.34
SDSS J0943+5958	725 ± 16	42.51 ± 0.06	−2.54 ± 0.07	−1.38 ± 0.05	652 ± 12	42.46 ± 0.06	−1.64 ± 0.07	−0.93 ± 0.07
SDSS J0944+3105	955 ± 41	42.85 ± 0.08	−2.67 ± 0.11	−1.45 ± 0.08	824 ± 30	42.82 ± 0.07	−1.74 ± 0.10	−0.99 ± 0.11
SDSS J0957+0207	1037 ± 66	43.26 ± 0.12	−2.40 ± 0.17	−1.31 ± 0.12	895 ± 48	43.23 ± 0.12	−1.42 ± 0.15	−0.82 ± 0.17
SDSS J1001+1829	896 ± 77	42.91 ± 0.19	−2.50 ± 0.24	−1.36 ± 0.17	788 ± 58	42.87 ± 0.19	−1.56 ± 0.23	−0.89 ± 0.24
SDSS J1002+4424	619 ± 13	43.61 ± 0.08	−1.15 ± 0.09	−0.69 ± 0.06	569 ± 11	43.55 ± 0.08	−0.31 ± 0.08	−0.27 ± 0.09
SDSS J1003+0202	1159 ± 97	43.36 ± 0.15	−2.50 ± 0.21	−1.36 ± 0.15	981 ± 67	43.32 ± 0.15	−1.50 ± 0.19	−0.86 ± 0.21
SDSS J1008+1549	985 ± 73	43.52 ± 0.16	−2.06 ± 0.20	−1.14 ± 0.14	856 ± 54	43.48 ± 0.15	−1.10 ± 0.19	−0.66 ± 0.20
SDSS J1009+3436	1018 ± 62	43.67 ± 0.13	−1.96 ± 0.17	−1.10 ± 0.12	891 ± 46	43.63 ± 0.13	−0.97 ± 0.16	−0.61 ± 0.17
SDSS J1009+2209	1115 ± 63	43.61 ± 0.11	−2.18 ± 0.14	−1.21 ± 0.10	953 ± 44	43.57 ± 0.10	−1.19 ± 0.13	−0.72 ± 0.14
SDSS J1011+5348	992 ± 59	43.97 ± 0.13	−1.62 ± 0.16	−0.92 ± 0.12	873 ± 45	43.93 ± 0.12	−0.63 ± 0.15	−0.43 ± 0.16
SDSS J1017+1224	1041 ± 55	43.12 ± 0.10	−2.55 ± 0.14	−1.39 ± 0.10	895 ± 40	43.08 ± 0.10	−1.58 ± 0.12	−0.90 ± 0.14
SDSS J1020+2515	901 ± 56	43.12 ± 0.14	−2.30 ± 0.18	−1.26 ± 0.13	794 ± 43	43.08 ± 0.14	−1.35 ± 0.17	−0.78 ± 0.18
SDSS J1029+2526	1772 ± 192	44.14 ± 0.15	−2.46 ± 0.24	−1.34 ± 0.17	1398 ± 112	44.07 ± 0.13	−1.30 ± 0.19	−0.76 ± 0.23
SDSS J1029+4829	1140 ± 96	44.04 ± 0.13	−1.79 ± 0.20	−1.01 ± 0.14	983 ± 70	44.00 ± 0.13	−0.75 ± 0.18	−0.49 ± 0.19
SDSS J1037+3912	738 ± 34	43.19 ± 0.13	−1.88 ± 0.15	−1.05 ± 0.11	664 ± 27	43.14 ± 0.13	−0.98 ± 0.14	−0.60 ± 0.15
SDSS J1041+3412	1169 ± 136	43.36 ± 0.21	−2.51 ± 0.29	−1.37 ± 0.21	991 ± 95	43.32 ± 0.20	−1.51 ± 0.26	−0.87 ± 0.29
SDSS J1043+2716	1035 ± 63	43.44 ± 0.11	−2.22 ± 0.15	−1.23 ± 0.11	894 ± 46	43.40 ± 0.10	−1.25 ± 0.14	−0.75 ± 0.15
SDSS J1046+1655	1074 ± 54	43.91 ± 0.10	−1.82 ± 0.13	−1.02 ± 0.09	932 ± 40	43.87 ± 0.09	−0.81 ± 0.12	−0.51 ± 0.13
SDSS J1051+2101	957 ± 58	42.57 ± 0.12	−2.96 ± 0.16	−1.60 ± 0.11	829 ± 42	42.53 ± 0.12	−2.02 ± 0.15	−1.13 ± 0.16
SDSS J1053+5524	849 ± 28	43.32 ± 0.08	−2.00 ± 0.10	−1.11 ± 0.07	755 ± 22	43.27 ± 0.08	−1.07 ± 0.09	−0.65 ± 0.10
SDSS J1058+5444	724 ± 16	43.29 ± 0.06	−1.75 ± 0.07	−0.99 ± 0.05	654 ± 13	43.24 ± 0.06	−0.86 ± 0.07	−0.55 ± 0.07
SDSS J1105+5941	1156 ± 32	43.33 ± 0.04	−2.53 ± 0.07	−1.38 ± 0.05	964 ± 22	43.28 ± 0.04	−1.58 ± 0.06	−0.90 ± 0.07
SDSS J1109+3708	881 ± 25	42.74 ± 0.06	−2.64 ± 0.08	−1.44 ± 0.05	768 ± 19	42.70 ± 0.06	−1.72 ± 0.07	−0.98 ± 0.07
SDSS J1111+5923	1174 ± 71	43.43 ± 0.11	−2.45 ± 0.15	−1.34 ± 0.11	999 ± 50	43.40 ± 0.11	−1.43 ± 0.14	−0.83 ± 0.15
SDSS J1114+4056	1114 ± 36	43.73 ± 0.05	−2.06 ± 0.08	−1.14 ± 0.05	954 ± 25	43.69 ± 0.05	−1.06 ± 0.07	−0.64 ± 0.07
SDSS J1115+0544	858 ± 167	43.49 ± 0.45	−1.85 ± 0.56	−1.04 ± 0.40	757 ± 128	43.45 ± 0.44	−0.92 ± 0.53	−0.57 ± 0.56
SDSS J1120+1933	1188 ± 87	43.73 ± 0.12	−2.17 ± 0.18	−1.20 ± 0.13	1002 ± 60	43.69 ± 0.12	−1.17 ± 0.16	−0.70 ± 0.18
SDSS J1122+1433	1302 ± 39	43.94 ± 0.05	−2.12 ± 0.07	−1.17 ± 0.05	1091 ± 26	43.90 ± 0.05	−1.06 ± 0.06	−0.64 ± 0.07
SDSS J1124+0455	697 ± 17	43.25 ± 0.07	−1.73 ± 0.08	−0.98 ± 0.06	629 ± 13	43.20 ± 0.07	−0.83 ± 0.08	−0.53 ± 0.08
SDSS J1129+5131	580 ± 6	42.99 ± 0.03	−1.67 ± 0.04	−0.95 ± 0.03	530 ± 5	42.93 ± 0.03	−0.78 ± 0.04	−0.50 ± 0.04
SDSS J1133+6701	994 ± 74	43.00 ± 0.14	−2.59 ± 0.19	−1.41 ± 0.13	853 ± 53	42.96 ± 0.13	−1.66 ± 0.17	−0.94 ± 0.18
SDSS J1139+6134	747 ± 20	43.35 ± 0.08	−1.74 ± 0.09	−0.99 ± 0.06	673 ± 16	43.30 ± 0.07	−0.84 ± 0.09	−0.54 ± 0.09
SDSS J1149+5441	1078 ± 92	43.05 ± 0.16	−2.68 ± 0.22	−1.45 ± 0.15	915 ± 64	43.02 ± 0.15	−1.72 ± 0.20	−0.97 ± 0.21
SDSS J1152+4850	1115 ± 80	43.82 ± 0.12	−1.97 ± 0.17	−1.10 ± 0.12	954 ± 57	43.78 ± 0.12	−0.97 ± 0.16	−0.60 ± 0.17
SDSS J1153+4037	990 ± 41	43.49 ± 0.08	−2.10 ± 0.11	−1.16 ± 0.08	862 ± 30	43.45 ± 0.08	−1.13 ± 0.10	−0.67 ± 0.11
SDSS J1200+0648	730 ± 28	43.46 ± 0.09	−1.60 ± 0.12	−0.91 ± 0.08	653 ± 22	43.41 ± 0.09	−0.70 ± 0.11	−0.46 ± 0.11
SDSS J1201+3525	985 ± 27	43.91 ± 0.06	−1.66 ± 0.07	−0.95 ± 0.05	863 ± 21	43.88 ± 0.05	−0.68 ± 0.07	−0.46 ± 0.07

Table 3
(Continued)

Name	$T_{\rm bb}$ (K)	$\log L_{\rm bb}$ (erg s^{-1})	$\log M_{\rm bb}$ ($M_\odot$)	$\log R_{\rm bb}$ (pc)	T_d (K)	$\log L_d$ (erg s^{-1})	$\log M_d$ ($M_\odot$)	$\log R_d$ (pc)
(1)	(2)	(3)	(4)	(5)	(6)	(7)	(8)	(9)
SDSS J1203+5859	807 ± 38	42.29 ± 0.10	−2.94 ± 0.13	−1.58 ± 0.09	714 ± 29	42.25 ± 0.10	−2.02 ± 0.13	−1.12 ± 0.13
SDSS J1208+3305	1087 ± 80	43.73 ± 0.14	−2.02 ± 0.19	−1.12 ± 0.14	949 ± 60	43.69 ± 0.14	−0.98 ± 0.18	−0.60 ± 0.19
SDSS J1209+3202	1050 ± 27	43.38 ± 0.04	−2.31 ± 0.06	−1.27 ± 0.04	895 ± 19	43.34 ± 0.04	−1.36 ± 0.06	−0.79 ± 0.06
SDSS J1211+4047	1243 ± 113	44.24 ± 0.18	−1.74 ± 0.24	−0.98 ± 0.17	1072 ± 82	44.21 ± 0.18	−0.63 ± 0.22	−0.43 ± 0.24
SDSS J1214+1014	1016 ± 161	43.58 ± 0.33	−2.05 ± 0.43	−1.14 ± 0.31	882 ± 119	43.55 ± 0.33	−1.07 ± 0.40	−0.65 ± 0.43
SDSS J1218+2951	877 ± 48	43.64 ± 0.13	−1.73 ± 0.16	−0.98 ± 0.11	776 ± 37	43.60 ± 0.12	−0.79 ± 0.15	−0.51 ± 0.16
SDSS J1219+0516	964 ± 60	43.29 ± 0.12	−2.25 ± 0.16	−1.24 ± 0.12	836 ± 44	43.25 ± 0.12	−1.31 ± 0.15	−0.77 ± 0.16
SDSS J1228+3617	1089 ± 92	43.48 ± 0.16	−2.27 ± 0.22	−1.25 ± 0.16	934 ± 66	43.45 ± 0.16	−1.28 ± 0.20	−0.76 ± 0.22
SDSS J1238+0815	949 ± 22	43.45 ± 0.04	−2.06 ± 0.06	−1.14 ± 0.04	829 ± 16	43.41 ± 0.04	−1.11 ± 0.06	−0.66 ± 0.06
SDSS J1242+2537	898 ± 60	42.91 ± 0.15	−2.51 ± 0.19	−1.37 ± 0.13	787 ± 45	42.87 ± 0.15	−1.57 ± 0.18	−0.90 ± 0.18
SDSS J1245−0147	797 ± 40	43.71 ± 0.14	−1.50 ± 0.16	−0.86 ± 0.11	719 ± 32	43.66 ± 0.13	−0.58 ± 0.16	−0.40 ± 0.16
SDSS J1303+2203	1259 ± 101	43.16 ± 0.13	−2.84 ± 0.19	−1.54 ± 0.13	1045 ± 67	43.12 ± 0.12	−1.85 ± 0.16	−1.04 ± 0.18
SDSS J1305+3953	1060 ± 41	43.16 ± 0.07	−2.54 ± 0.10	−1.39 ± 0.07	905 ± 29	43.12 ± 0.07	−1.59 ± 0.09	−0.91 ± 0.10
SDSS J1308+0429	982 ± 45	42.78 ± 0.09	−2.79 ± 0.12	−1.51 ± 0.08	845 ± 33	42.74 ± 0.09	−1.85 ± 0.11	−1.04 ± 0.11
SDSS J1310+2518	1053 ± 72	43.50 ± 0.14	−2.19 ± 0.18	−1.21 ± 0.13	911 ± 52	43.46 ± 0.13	−1.20 ± 0.17	−0.72 ± 0.18
SDSS J1315+0727	1167 ± 50	43.55 ± 0.07	−2.32 ± 0.10	−1.28 ± 0.07	982 ± 34	43.51 ± 0.07	−1.34 ± 0.09	−0.79 ± 0.10
SDSS J1322+3301	911 ± 23	43.40 ± 0.06	−2.04 ± 0.07	−1.14 ± 0.05	801 ± 17	43.36 ± 0.05	−1.10 ± 0.07	−0.67 ± 0.07
SDSS J1328+2752	1028 ± 72	43.34 ± 0.13	−2.31 ± 0.18	−1.27 ± 0.13	884 ± 52	43.31 ± 0.13	−1.35 ± 0.16	−0.79 ± 0.18
SDSS J1329+2341	694 ± 19	43.13 ± 0.07	−1.83 ± 0.09	−1.03 ± 0.06	626 ± 15	43.08 ± 0.07	−0.94 ± 0.09	−0.58 ± 0.09
SDSS J1332+2036	1001 ± 26	43.86 ± 0.05	−1.74 ± 0.07	−0.99 ± 0.05	867 ± 19	43.82 ± 0.05	−0.78 ± 0.07	−0.51 ± 0.07
SDSS J1337+0035	1288 ± 108	44.59 ± 0.13	−1.45 ± 0.20	−0.84 ± 0.14	1098 ± 76	44.55 ± 0.12	−0.35 ± 0.17	−0.29 ± 0.19
SDSS J1340+1842	945 ± 59	42.79 ± 0.12	−2.72 ± 0.16	−1.47 ± 0.12	823 ± 44	42.75 ± 0.12	−1.77 ± 0.15	−1.00 ± 0.16
SDSS J1341−0049	1226 ± 105	43.81 ± 0.14	−2.14 ± 0.21	−1.19 ± 0.15	1036 ± 73	43.77 ± 0.14	−1.11 ± 0.18	−0.68 ± 0.20
SDSS J1341+1516	831 ± 25	43.33 ± 0.07	−1.95 ± 0.09	−1.09 ± 0.06	739 ± 20	43.28 ± 0.07	−1.03 ± 0.08	−0.63 ± 0.09
SDSS J1348+1559	1043 ± 52	44.01 ± 0.10	−1.67 ± 0.13	−0.95 ± 0.09	906 ± 39	43.97 ± 0.09	−0.67 ± 0.12	−0.45 ± 0.13
SDSS J1352+0009	944 ± 37	43.42 ± 0.08	−2.08 ± 0.11	−1.16 ± 0.08	830 ± 28	43.38 ± 0.08	−1.12 ± 0.10	−0.68 ± 0.11
SDSS J1402+3922	1177 ± 45	43.63 ± 0.06	−2.26 ± 0.09	−1.24 ± 0.07	984 ± 30	43.59 ± 0.06	−1.29 ± 0.08	−0.76 ± 0.09
SDSS J1406+0628	861 ± 17	43.37 ± 0.04	−1.97 ± 0.06	−1.10 ± 0.04	759 ± 13	43.33 ± 0.04	−1.04 ± 0.05	−0.64 ± 0.06
SDSS J1409+1057	662 ± 17	43.17 ± 0.07	−1.72 ± 0.09	−0.97 ± 0.06	600 ± 14	43.11 ± 0.07	−0.83 ± 0.08	−0.53 ± 0.09
SDSS J1412+4114	1227 ± 46	43.13 ± 0.06	−2.83 ± 0.09	−1.53 ± 0.06	1025 ± 30	43.09 ± 0.06	−1.83 ± 0.08	−1.03 ± 0.09
SDSS J1422+0609	1105 ± 22	43.58 ± 0.03	−2.20 ± 0.05	−1.21 ± 0.03	933 ± 15	43.54 ± 0.03	−1.24 ± 0.04	−0.73 ± 0.04
SDSS J1424+6249	1188 ± 50	43.35 ± 0.06	−2.56 ± 0.10	−1.39 ± 0.07	999 ± 34	43.31 ± 0.06	−1.56 ± 0.08	−0.89 ± 0.09
SDSS J1428−0231	940 ± 101	42.34 ± 0.22	−3.16 ± 0.29	−1.69 ± 0.20	815 ± 75	42.30 ± 0.21	−2.22 ± 0.26	−1.22 ± 0.28
SDSS J1430+2303	1204 ± 63	43.62 ± 0.09	−2.31 ± 0.13	−1.27 ± 0.09	1005 ± 42	43.57 ± 0.08	−1.33 ± 0.11	−0.78 ± 0.12
SDSS J1440+1758	927 ± 55	42.80 ± 0.13	−2.67 ± 0.16	−1.45 ± 0.12	812 ± 41	42.76 ± 0.12	−1.73 ± 0.15	−0.98 ± 0.16
SDSS J1442+5558	1158 ± 35	44.06 ± 0.05	−1.79 ± 0.07	−1.01 ± 0.05	973 ± 23	44.03 ± 0.05	−0.82 ± 0.06	−0.52 ± 0.07
SDSS J1447+4023	1202 ± 46	43.80 ± 0.07	−2.12 ± 0.09	−1.18 ± 0.07	1012 ± 32	43.76 ± 0.06	−1.12 ± 0.08	−0.68 ± 0.09
SDSS J1448+1137	828 ± 19	43.00 ± 0.05	−2.28 ± 0.06	−1.25 ± 0.05	732 ± 15	42.96 ± 0.05	−1.36 ± 0.06	−0.79 ± 0.07
SDSS J1504+0107	1140 ± 37	44.20 ± 0.05	−1.63 ± 0.08	−0.93 ± 0.06	969 ± 26	44.16 ± 0.05	−0.64 ± 0.07	−0.44 ± 0.08
SDSS J1508+2602	657 ± 22	42.97 ± 0.10	−1.90 ± 0.12	−1.07 ± 0.08	597 ± 18	42.91 ± 0.10	−1.02 ± 0.11	−0.63 ± 0.11
SDSS J1511+2214	848 ± 33	43.40 ± 0.09	−1.91 ± 0.11	−1.07 ± 0.08	752 ± 26	43.36 ± 0.09	−0.98 ± 0.11	−0.61 ± 0.11
SDSS J1512+2809	761 ± 19	43.12 ± 0.06	−2.00 ± 0.08	−1.12 ± 0.05	683 ± 15	43.07 ± 0.06	−1.10 ± 0.07	−0.67 ± 0.07
SDSS J1513+3111	1147 ± 31	43.32 ± 0.05	−2.52 ± 0.07	−1.37 ± 0.05	964 ± 21	43.28 ± 0.05	−1.55 ± 0.06	−0.89 ± 0.07
SDSS J1524+5314	1202 ± 84	42.92 ± 0.11	−3.00 ± 0.16	−1.61 ± 0.11	1005 ± 57	42.88 ± 0.10	−2.02 ± 0.14	−1.12 ± 0.15
SDSS J1531+3724	1026 ± 93	42.19 ± 0.17	−3.46 ± 0.23	−1.84 ± 0.16	874 ± 66	42.15 ± 0.16	−2.52 ± 0.21	−1.37 ± 0.22
SDSS J1533+2729	959 ± 84	43.48 ± 0.17	−2.05 ± 0.23	−1.14 ± 0.16	831 ± 62	43.44 ± 0.16	−1.11 ± 0.21	−0.67 ± 0.22
SDSS J1537+5814	1102 ± 128	43.71 ± 0.20	−2.06 ± 0.28	−1.14 ± 0.20	937 ± 90	43.68 ± 0.19	−1.08 ± 0.25	−0.65 ± 0.27
SDSS J1540+0054	894 ± 82	40.78 ± 0.18	−4.63 ± 0.24	−2.43 ± 0.17	776 ± 60	40.74 ± 0.18	−3.71 ± 0.23	−1.97 ± 0.24
SDSS J1541+0718	933 ± 77	43.29 ± 0.19	−2.19 ± 0.23	−1.21 ± 0.17	821 ± 59	43.25 ± 0.18	−1.23 ± 0.22	−0.73 ± 0.23
SDSS J1548+2208	998 ± 32	43.25 ± 0.06	−2.35 ± 0.08	−1.29 ± 0.06	854 ± 23	43.21 ± 0.06	−1.42 ± 0.07	−0.82 ± 0.08
SDSS J1549+3327	1053 ± 54	43.37 ± 0.09	−2.33 ± 0.13	−1.28 ± 0.09	901 ± 39	43.33 ± 0.09	−1.36 ± 0.12	−0.79 ± 0.13
SDSS J1554+5255	868 ± 6	43.16 ± 0.02	−2.19 ± 0.02	−1.21 ± 0.01	763 ± 4	43.12 ± 0.01	−1.27 ± 0.02	−0.75 ± 0.02
SDSS J1554+1636	1026 ± 116	40.69 ± 0.20	−4.95 ± 0.28	−2.59 ± 0.20	871 ± 81	40.65 ± 0.20	−4.03 ± 0.25	−2.13 ± 0.27
SDSS J1554+3629	1207 ± 169	44.01 ± 0.27	−1.92 ± 0.36	−1.07 ± 0.26	1032 ± 120	43.97 ± 0.26	−0.86 ± 0.33	−0.54 ± 0.36
SDSS J1555+2120	741 ± 17	43.19 ± 0.06	−1.89 ± 0.07	−1.06 ± 0.05	664 ± 14	43.14 ± 0.06	−0.99 ± 0.07	−0.61 ± 0.07
SDSS J1556+4513	1009 ± 76	43.64 ± 0.15	−1.98 ± 0.20	−1.10 ± 0.14	881 ± 56	43.60 ± 0.14	−0.99 ± 0.18	−0.61 ± 0.19
SDSS J1557+2727	617 ± 5	43.05 ± 0.03	−1.72 ± 0.03	−0.97 ± 0.02	561 ± 4	42.99 ± 0.02	−0.83 ± 0.03	−0.53 ± 0.03
SDSS J1600+4612	929 ± 27	43.63 ± 0.07	−1.85 ± 0.09	−1.04 ± 0.06	821 ± 21	43.59 ± 0.07	−0.88 ± 0.08	−0.55 ± 0.09
SDSS J1612+1416	708 ± 13	42.72 ± 0.05	−2.28 ± 0.06	−1.26 ± 0.04	638 ± 11	42.67 ± 0.05	−1.39 ± 0.06	−0.81 ± 0.06
SDSS J1620+2407	1349 ± 99	43.32 ± 0.10	−2.80 ± 0.17	−1.51 ± 0.12	1096 ± 62	43.27 ± 0.10	−1.81 ± 0.14	−1.01 ± 0.16
SDSS J1628+4810	778 ± 26	43.01 ± 0.09	−2.16 ± 0.11	−1.19 ± 0.07	698 ± 21	42.96 ± 0.09	−1.25 ± 0.10	−0.74 ± 0.10
SDSS J1632+4416	1235 ± 76	43.17 ± 0.10	−2.80 ± 0.15	−1.52 ± 0.11	808 ± 13	42.63 ± 0.04	−1.88 ± 0.05	−1.06 ± 0.14

Table 3
(Continued)

Name	T_{bb} (K)	log L_{bb} (erg s^{-1})	log M_{bb} ($M_\odot$)	log R_{bb} (pc)	T_d (K)	log L_d (erg s^{-1})	log M_d ($M_\odot$)	log R_d (pc)
(1)	(2)	(3)	(4)	(5)	(6)	(7)	(8)	(9)
SDSS J1647+3843	1036 ± 51	43.25 ± 0.10	−2.42 ± 0.13	−1.32 ± 0.09	1027 ± 51	43.12 ± 0.10	−1.82 ± 0.13	−1.02 ± 0.13
SDSS J1657+2345	842 ± 33	43.93 ± 0.09	−1.37 ± 0.11	−0.80 ± 0.08	749 ± 26	43.83 ± 0.08	−0.53 ± 0.10	−0.38 ± 0.11
SDSS J1659+2049	633 ± 8	43.10 ± 0.04	−1.71 ± 0.05	−0.97 ± 0.03	708 ± 10	42.80 ± 0.04	−1.46 ± 0.05	−0.85 ± 0.05
SDSS J2115−0011	1206 ± 94	43.67 ± 0.14	−2.25 ± 0.19	−1.24 ± 0.14	1333 ± 130	43.54 ± 0.16	−1.75 ± 0.23	−0.99 ± 0.20
SDSS J2141−0857	912 ± 41	43.01 ± 0.09	−2.43 ± 0.12	−1.33 ± 0.09	794 ± 31	42.89 ± 0.09	−1.56 ± 0.11	−0.90 ± 0.12
SDSS J2146+1041	1818 ± 466	43.38 ± 0.28	−3.26 ± 0.52	−1.74 ± 0.37	848 ± 52	43.26 ± 0.15	−1.28 ± 0.18	−0.75 ± 0.46
SDSS J2150−0106	1255 ± 205	43.35 ± 0.24	−2.64 ± 0.37	−1.44 ± 0.26	1043 ± 135	43.24 ± 0.22	−1.73 ± 0.32	−0.99 ± 0.36
SDSS J2156+0041	692 ± 12	42.74 ± 0.04	−2.22 ± 0.05	−1.22 ± 0.04	709 ± 13	42.45 ± 0.05	−1.80 ± 0.06	−1.01 ± 0.06
SDSS J2203+1124	1024 ± 70	43.92 ± 0.15	−1.73 ± 0.19	−0.98 ± 0.13	909 ± 54	43.85 ± 0.15	−0.79 ± 0.18	−0.51 ± 0.18
SDSS J2215−0107	801 ± 27	42.79 ± 0.08	−2.43 ± 0.10	−1.33 ± 0.07	789 ± 24	42.69 ± 0.07	−1.77 ± 0.09	−1.00 ± 0.10
SDSS J2310+2220	883 ± 29	42.90 ± 0.07	−2.49 ± 0.09	−1.36 ± 0.07	796 ± 23	42.68 ± 0.07	−1.79 ± 0.09	−1.01 ± 0.09
SDSS J2312+1335	985 ± 49	43.33 ± 0.10	−2.24 ± 0.13	−1.24 ± 0.09	853 ± 36	43.17 ± 0.10	−1.38 ± 0.12	−0.81 ± 0.13
SDSS J2324+1542	1202 ± 70	43.70 ± 0.10	−2.22 ± 0.15	−1.22 ± 0.10	1168 ± 78	43.54 ± 0.12	−1.58 ± 0.17	−0.90 ± 0.15

Note. Column (1): object name. Columns (2)–(4): dust temperature, luminosity, and mass fitted with the blackbody model at the epoch of W2 luminosity maximum. The dust mass is in units of solar mass. Column (5): distance of the dust to the central heating source assuming spherically symmetric distribution and a covering factor of 1. Columns (6)–(9): similar to columns (2)–(5) but with the dust absorption coefficient considered.

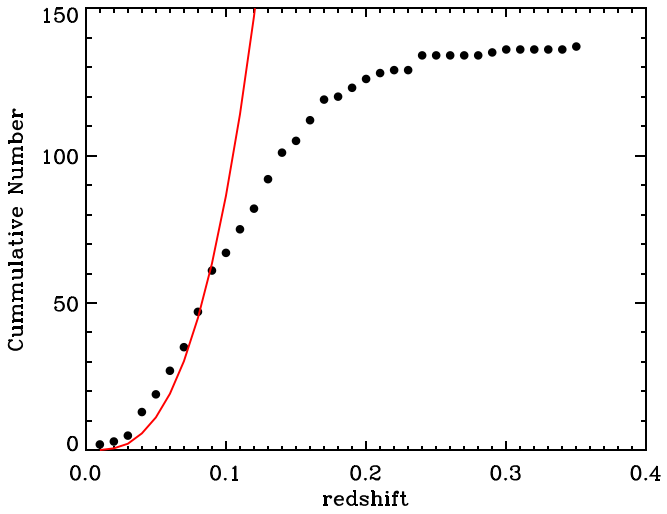

Figure 8. Accumulated redshift distribution of our sample. The curve shows the comoving volume of th SDSS footprint at the corresponding redshift multiplied by 1.2×10^{-6} Mpc^{-3}.

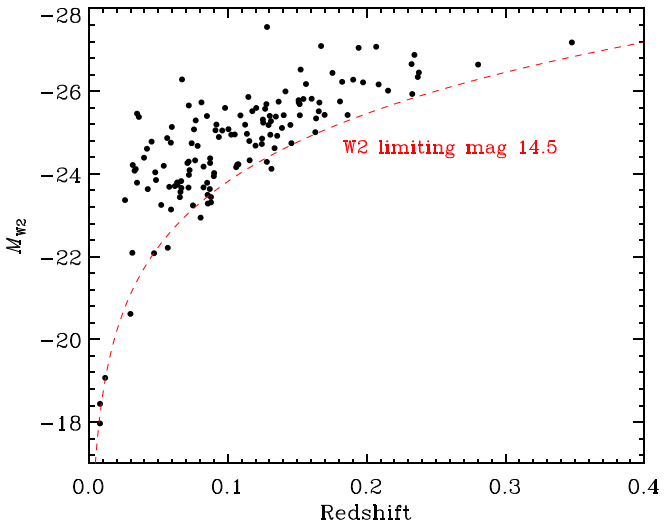

Figure 9. Host galaxy W2 absolute magnitudes (quiescent state) of our sample, which decreases with redshift. The red dashed line denotes the limiting magnitude of 14.5.

used to characterize galaxy luminosity functions (Schechter 1976) in the form of

$$\Phi(L)\mathrm{dL} = \left(\frac{\Phi^*}{L^*}\right)\left(\frac{L}{L^*}\right)^{\alpha} e^{-L/L^*}\mathrm{dL}, \quad (6)$$

where L is the galaxy luminosity, L^* is the characteristic luminosity where the power-law form of the function cuts off, and the parameter Φ^* is the normalization. We try to fit the luminosity function at the high end with a single Schechter function, yielding $\log \Phi^* = -2.92$, $\log L^* = 43.50$, and $\alpha = -0.05$. The sources at the very faint end of $\log L_{W2}$ (<41) are occupied by SNe and appear as a distinct population from the high end; thus, we have ignored them in the fitting. The luminosity function drops quickly at the very high end. The flattening at $\log L_{W2} \lesssim 43$ could be due to the selection effect that requires a brightening amplitude greater than 0.5 mag. It is possible that there are more fainter outbursts with relatively low brightening amplitudes (<0.5 mag) that were missed by our selection.

5. Host Galaxy and Central BH

5.1. Host Galaxy Properties

The host galaxy properties are crucial to understanding the nature of MIRONG. It is well known that galaxies show a bimodal distribution in the color–magnitude diagram (CMD), which is mainly clustered into a red sequence and blue cloud (e.g., Strateva et al. 2001; Bell et al. 2004) with a green valley in between. We retrieved the apparent *ugriz* Petrosian magnitudes from the SDSS DR14 and then corrected for the extinction using the dust maps of Schlegel et al. (1998). For a fair comparison of galaxies at different redshifts in the CMD, we applied *k*-corrections to the observed magnitudes to $z = 0.1$

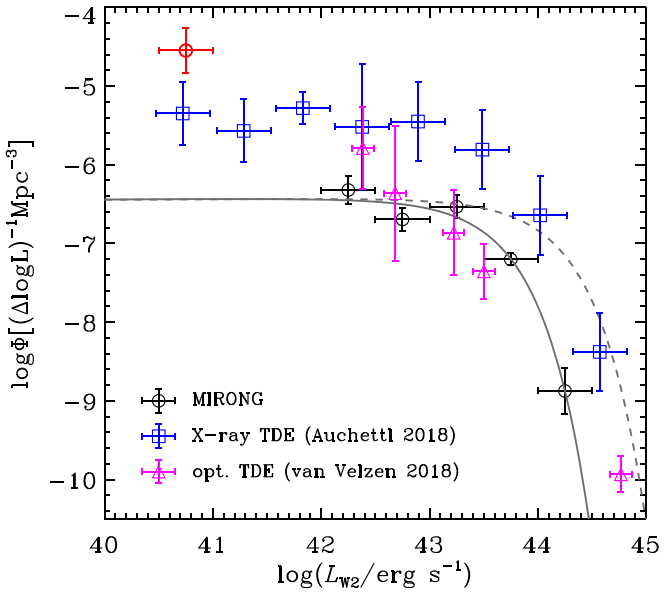

Figure 10. The W2 peak luminosity function of our MIRONG sample. The data points are plotted with log L_{W2} ranging from 40.5 to 44.5 (bin 0.5). The faint end (log $L_{W2} \in [40.5, 41]$) is totally contributed by extremely low-redshift SNe (red circle). The high end (log $L_{W2} > 42$) is fitted by a single Schechter function (gray line). The shifted gray dashed line depicts the luminosity function of the primary emission that causes the MIR outburst assuming a dust covering factor of 0.3. We have also overlaid the observed X-ray (blue squares; data from Figure 6 of Auchettl et al. 2018) and optical (magenta triangles; data from Figure 1 of van Velzen 2018) luminosity functions of TDEs for comparison.

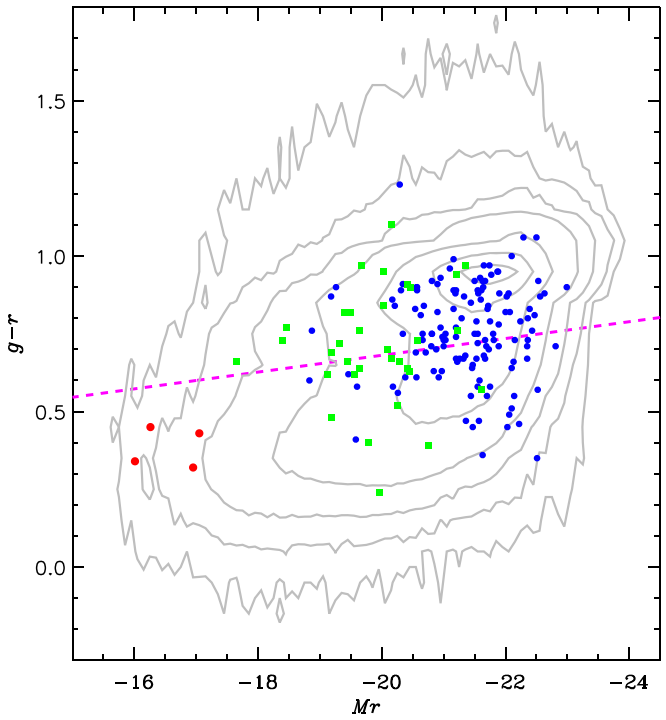

Figure 11. The CMD ($g - r$ vs. M_r) of the MIRONG sample (blue filled circles). The magnitudes and color are displayed after correction for Galactic dust extinction and k-correction to $z = 0.1$. We denote the four SN host galaxies in red. Contours show the density of low-redshift ($z < 0.2$) SDSS DR7 spectroscopic galaxies. The contour lines correspond to 5, 25, 100, 400, 2000, 5000, and 8000 galaxies bin^{-1} of $\Delta(g - r) = 0.1$ and $\Delta M_r = 0.1$. The magenta dashed line is the assigned line of demarcation between the blue clouds and red sequence. We have also plotted the optical TDEs (van Velzen et al. 2020) for comparison (green squares), in which the magnitudes are from either SDSS or Pan-STARRS.

(close to the median redshift of our sample) using the `IDL` code `KCORRECT` (v4.3) [13] given by Blanton & Roweis (2007; see also Blanton et al. 2003). To divide the SDSS galaxy sample into the red and blue classes, we used the following magnitude-dependent color cut:

$$g - r = -0.027 * M_r + 0.14. \quad (7)$$

Our sample concentrates on the densest region of the CMD diagram (see Figure 11). There are 82 galaxies categorized into the red sequence, and the fraction (59.9%) is somewhat comparable to the ensemble SDSS spectroscopic galaxy sample (63.0%). The difference in M_r is also tiny, with our sample only 0.24 mag brighter. In other words, the host galaxies of the MIR outbursts are not significantly biased in terms of optical color and magnitude. For comparison, the host galaxies of optically selected TDEs are much less luminous, and most are dwarf galaxies.

The SDSS data release also provides a value-added catalog of the galaxy intrinsic properties.[14] For instance, the Portsmouth group has performed stellar kinematics and emission-line flux measurements (Thomas et al. 2013) using the publicly available codes Penalized PiXel Fitting (pPXF; Cappellari & Emsellem 2004) and Gas and Absorption Line Fitting (GANDALF v1.5; Sarzi et al. 2006). GANDALF fits stellar population and Gaussian emission-line templates to the galaxy spectrum simultaneously to separate stellar continuum and absorption lines from the ionized gas emission. Stellar kinematics are evaluated by pPXF where the line-of-sight velocity distribution is fitted directly in pixel space. The fits account for the impact of diffuse dust in the galaxy on the spectral shape adopting a Calzetti (2001) extinction curve. Outputs from this fitting process include stellar velocity dispersions ($\sigma_\star$), emission-line fluxes, equivalent widths, and BPT classifications. Note that for one source, SDSS J1422 +1609, the galaxy parameters are not available in the catalog due to the lack of SDSS spectrum.

The Portsmouth group has also provided the measurements of stellar mass ($M_\star$) through spectral energy distribution (SED) fitting with stellar population models (Maraston et al. 2013). However, their fittings only considered the SDSS optical photometry and may induce bias due to the narrow range of wavelength coverage. Therefore, we tried more comprehensive SED fittings by including the near-IR and ultraviolet (UV) photometry, which is capable of better tracing the old and young stellar populations, respectively. The UV data are taken by the Galaxy Evolution Explorer (GALEX; Martin et al. 2005) with the near-UV (NUV) and far-UV (FUV) filters. For the NIR data, we adopted the *J*-, *H*-, and *K*-band Petrosian magnitudes given by the UKIRT InfraRed Deep Sky Surveys (UKIDSS; Lawrence et al. 2007). For sources that are located outside the UKIDSS footprint, we used the magnitudes from the Two Micron All Sky Survey (2MASS; Skrutskie et al. 2006).

After gathering the UV, optical, and NIR magnitudes, as well as their errors, we begin the broadband SED fitting utilizing `iSEDfit`,[15] which is a code to determine the $M_\star$, star formation rates (SFRs), and other physical properties of galaxies within a simplified Bayesian framework (Moustakas

[13] http://kcorrect.org/
[14] https://www.sdss.org/dr15/spectro/galaxy/
[15] http://www.sos.siena.edu/ jmoustakas/isedfit/

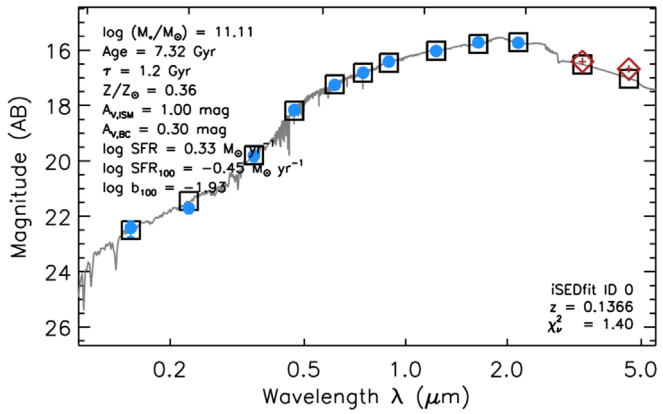

Figure 12. The SED fit of one galaxy (SDSS J0000+1438) in our sample. We have collected the NUV (GALEX), optical (SDSS), NIR (UKIDSS or 2MASS), and MIR (WISE) magnitudes and then performed the fitting with `iSEDfit`. The blue filled circles are actual photometry data used in the fitting, and the black open squares are predictions of the fitting model at the input bands. The WISE W1 and W2 bands (red open diamonds) have not been used in the fitting but only plotted as a comparison, since the PSF magnitudes will underestimate the flux of extended sources (e.g., nearby galaxies). Most of the photometry errors are tiny and thus are not visible in the plots.

et al. 2013). The fitting results are quite good (see an example in Figure 12), and the resulting $M_\star$ are higher than those given by the Portsmouth group by a median of 0.16 dex, indicating a fraction of the old stellar population probably missed by the SED fitting using only the optical data. Generally, the $M_\star$ distribution is consistent with the M_{r^*}. Most galaxies (92.0%) have stellar masses in the range $10^{10-11.5}\,M_\odot$ (median $10^{10.7}\,M_\odot$; see Figure 15). The least massive five galaxies with a mass lower than $10^{9.5}\,M_\odot$, including the four SN hosts, could be classified as dwarf galaxies, since their masses are even lower than the Large Magellanic Cloud ($2.7\times10^9\,M_\odot$; van der Marel et al. 2002).

5.2. Nuclear Activity and Mass of SMBHs

As we have mentioned in Section 1, the transient accretion onto SMBHs is a major population of extragalactic transients associated with galaxies. It is thus useful to assess the preoutburst nuclear activity of these galaxies, which may shed light on the nature of the outburst. The narrow-line ratios of galaxies, namely their location at the BPT diagram, can be used as a diagnosis of the nuclear activity, but only the broad emission lines can give unambiguous evidence of active SMBHs and plausible estimated $M_{\rm BH}$. In order to detect the potential broad lines, we have performed careful spectral analysis on the SDSS spectrum of these galaxies.

Our spectral fitting procedures are as follows: (1) subtracting the starlight and AGN continuum to obtain the emission-line residuals and (2) Gaussian fitting to emission lines including broad components when necessary. The spectrum is corrected for the Galactic extinction with the extinction map of Schlegel et al. (1998) and the reddening curve of Fitzpatrick (1999). We model the starlight component with the stellar templates of Lu et al. (2006), which were built from the simple stellar population spectra (Bruzual & Charlot 2003). The AGN continuum is modeled as a power law. After subtracting the starlight and AGN continuum component, we try to fit emission lines with multiple Gaussians, while only broad components ($\sigma>500\,{\rm km\,s^{-1}}$) for H$\alpha$, H$\beta$, Mg II, and He I are allowed to vary. Although emission lines in a fraction of galaxies can be fitted with a broad Hα component superimposed on the narrow component, only those broad Hα lines with S/Ns higher than 10 are considered valid, resulting in a final sample of 26 galaxies. The robustness of our fitting results is demonstrated in SDSS J0158–0052 (see Figure 13), which is a well-known low-mass AGN candidate selected by broad Hα emission (Greene & Ho 2007; Xiao et al. 2011). The $M_{\rm BH}$ is subsequently calculated by an empirical virial mass estimator ($M_{\rm BH}=fRv^2/G$) for single-epoch spectra using the formalism presented in Greene & Ho (2007). This method postulates that the broad-line region gas is virialized with a velocity dispersion characterized by the widths of broad lines and a distance to the BH estimated from the conventional radius–luminosity relation (e.g., Kaspi et al. 2005; Bentz et al. 2013).

Regarding the narrow-line sources, their nuclear activity can be alternatively identified by their positions in the BPT diagram (see Figure 14). According to the classification of the Portsmouth group (with the broad-line AGNs updated from our own fittings), our sample can be categorized into 37 (14 with broad lines) Seyferts, 23 (4) LINERs, 35 (2) star-forming galaxies, and 41 (6) composites. Broad-line star-forming galaxies are not common but indeed exist (see Figure 8 of Liu et al. 2019). However, the fraction in our sample looks somewhat high (2/35), which may indicate the some of the MIR outbursts in star-forming galaxies are driven by AGNs. The total number of AGNs contained in our sample is 49 ($37+4+2+6$) when taking into account both Seyferts and broad-line sources in other BPT types.

No clear evidence of intense AGN activity is found for other sources. We caution that LINERs can be treated as weak AGNs powered by SMBHs. In the absence of broad lines, we have to estimate their $M_{\rm BH}$ with other approaches, such as the correlations with either the $\sigma_\star$ or mass of the galactic bulge ($M_{\rm bulge}$) established in local massive galaxies (see Kormendy & Ho 2013 for a review). Our experiences and other works suggest that the velocity dispersion after correction of the instrument broadening ($70\,{\rm km\,s^{-1}}$) is reliable down to $\sim50-60\,{\rm km\,s^{-1}}$ (e.g., Zahid et al. 2016; Chilingarian et al. 2017). Hence, we adopted only the $M_{\rm BH}$–$\sigma_\star$ relation when $\sigma_\star>50\,{\rm km\,s^{-1}}$, leaving seven galaxies without $M_{\rm BH}$ measurements because of low $\sigma_\star$. Although the $M_{\rm BH}$–$M_{\rm bulge}$ relation (e.g., McConnell & Ma 2013) has been extensively used to estimate $M_{\rm BH}$, the SDSS resolution is generally too low to isolate the bulge component from the disk. We thus used the relation between $M_{\rm BH}$ and total stellar mass (Reines & Volonteri 2015) for the last seven objects. Our final sample has a broad range of $M_{\rm BH}$ with a logarithmic mass from 4.5 to 9.0 (median 7.3; see Figure 15).

6. Nature of the MIR Flares

The above analysis of the properties of MIR flares and their host galaxies allows us to further explore their physical nature. The MIR flares can be generally attributed to nonthermal emission from jets or dust thermal emission heated by different processes, such as SNe, AGNs, or TDEs. We will discuss each of these possibilities below.

6.1. Infrared Luminous SNe

As mentioned in Section 3.1, SDSS J0936+0615, SDSS J1531+3724, SDSS J1540+0054, and SDSS J1554+1636 are known hosts of SNe reported by ASASSN.[16] Interestingly,

[16] http://www.astronomy.ohio-state.edu/asassn/sn_list.html

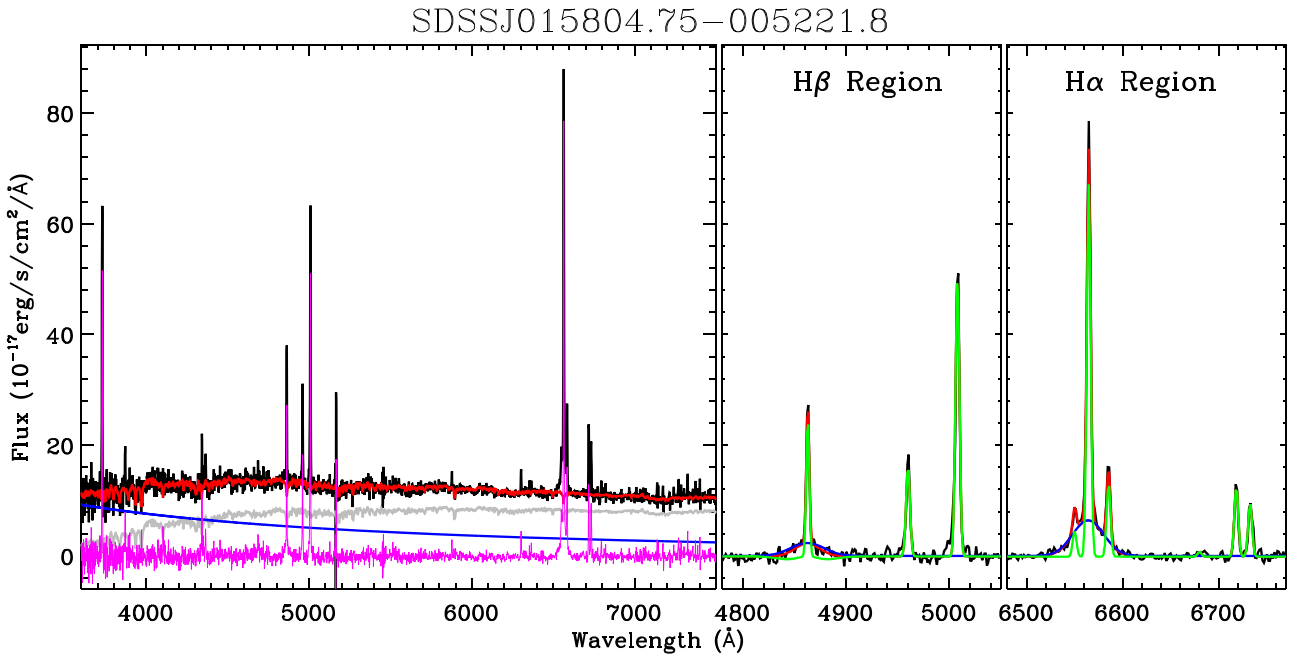

Figure 13. We show the analysis of the SDSS spectrum of SDSS J0158–0052 as an illustration of the spectral decomposition. The left panel displays the subtraction of starlight (gray) and AGN continuum (blue). The sum of the starlight and continuum is plotted in red, and the residual is plotted in magenta. The middle panel highlights the Gaussian fitting of the Hβ–[O III] region, in which the broad Hα component, narrow lines, and total are shown in blue, green, and red, respectively. The right panel is similar but for the Hα–[N II]–[S II] region.

their peak MIR luminosity appears to be lowest, with absolute W2 magnitudes fainter than −22 (or $\log L_{\rm W2} < 42$). The reason that they pass our selection threshold of variability amplitude (>0.5 mag) could be the dwarfness of their host galaxies (see Figure 11), which makes the MIR outburst luminosity overluminous with respect to the host. Indeed, the four SN galaxies are the least massive ones and occupy the low-mass end ($\log M_* < 9$). In addition, these galaxies appear very young in terms of their blue colors (g–$r < 0.5$). Hence, the SNe in our sample occupy the lowest MIR luminosity end and reside in dwarf star-forming galaxies.

Spectroscopic follow-ups have classified the four SNe into one Ia-91T-like and three type II sources. Previous studies suggest that the IR emission of SNe IIn is statistically more luminous and long-lasting than other types (e.g., type Ia) due to the heating of preexisting dust in the circumstellar medium (CSM; Fox et al. 2013; Tinyanont et al. 2016). The SNe Ia usually show very weak MIR emission and are not detectable 3 yr after the explosion (Tinyanont et al. 2016), except for the Ia-CSM subclass. In the same way, some 91T-like SNe also display the interacting CSM (e.g., Harris et al. 2018), which could be responsible for the observed MIR flare. The luminous infrared transients uncovered by the SPIRITS project are mainly obscured core-collapse SNe with peak 4.5 μm (Spitzer, roughly WISE W2) magnitudes between −14 and −18.2 (Jencson et al. 2019), which are significantly fainter than that in our sample.

The evolution of absolute W2 magnitudes as a function of time is presented in Figure 16. It is clear that the four SNe have the faintest MIR emission (see also the peak magnitude distribution in Figure 6), and their duration is relatively short. While the SN occurring in SDSS J1531+3724 (ASASSN-17jq) is relatively bright, it is still fainter than the non-SN objects. In our previous work (Jiang et al. 2019), we checked for the WISE light curves of all SNe in the public catalog reported between 2008 and 2018. Among them, the most luminous ones are all IIn (e.g., SN2010jl, SN2013dz, and SN2014ab) with luminosity $L_{W2} \sim 10^{42}$ erg s^{-1}, which is comparable to that of ASASSN-17jq. In summary, the MIR luminosity of our sample is systematically higher than the SN by at least 2–3 mag; thus, the SN scenario is disfavored as the origin for the bulk of MIRONG.

6.2. Nonthermal Emission from Jet

We next examine the possibility of nonthermal emission produced by relativistic jets. It has been proved that the synchrotron radiation of jets can contribute significantly to the MIR emission, as well as its variability (e.g., Jiang et al. 2012; Liao et al. 2019). We cross-matched our sample with the catalog of Faint Images of the Radio Sky at Twenty cm (FIRST)[17] using a matching radius of 5″, resulting in 22 objects detected with S/Ns higher than 5. There are eight objects outside of the FIRST footprint, so we matched them with the NRAO VLA Sky Survey (NVSS) catalog[18] but found nondetections.

The radio detections do not necessarily suggest the association with jet activity, since the star formation may also contribute to the radio emission. We used the SFR given by Chang et al. (2015), which is derived by fitting the broadband SDSS+WISE SED using MAGPHYS (da Cunha et al. 2008). The SFR measurements for 128 out of 137 galaxies are found. For the remaining sources, the SFRs were estimated from the 24 μm flux[19] (Chary & Elbaz 2001). Then we calculated the expected radio flux from star formation using the correlation between 1.4 GHz luminosity ($L_{1.4\,\rm G}$) and SFR (Equation (3) in Davies et al. 2017). As displayed in Table 4 and Figure 17, the

[17] http://sundog.stsci.edu/cgi-bin/searchfirst
[18] https://www.cv.nrao.edu/nvss/NVSSlist.shtml
[19] Here we adopted the WISE W4-band (22 μm) flux as an approximation.

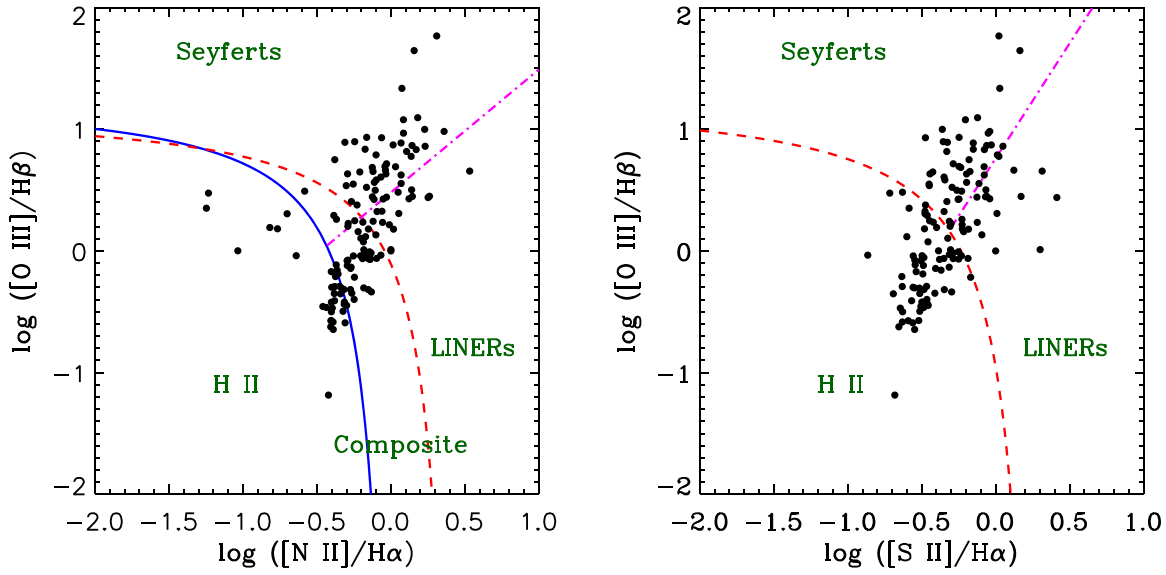

Figure 14. Locations of the MIR outburst galaxies (black filled circles) in the BPT diagram. The lines separating the different regions are mainly drawn from Kewley et al. (2006), only with the Seyfert/LINER dividing line (magenta dashed line) in the left panel from Cid Fernandes et al. (2010).

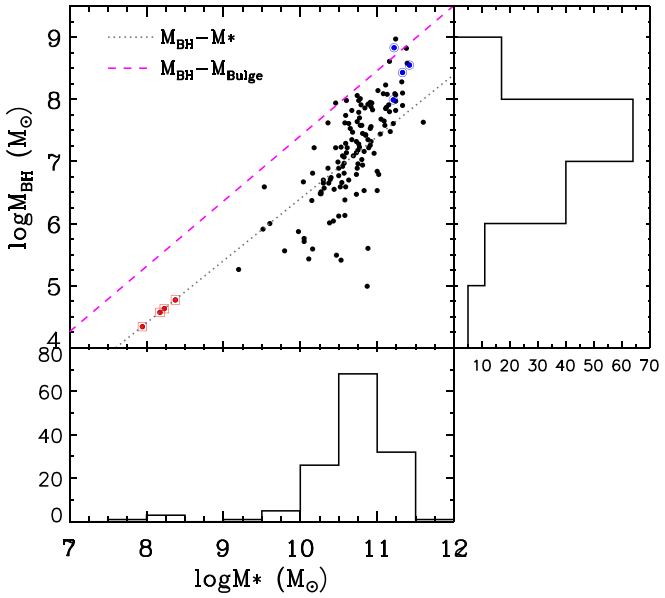

Figure 15. The BH mass ($M_{\rm BH}$) vs. stellar mass (M_*) distribution of our sample. The red filled circles are SNe, and the blue filled circles are strong jetted sources. The histograms of $M_{\rm BH}$ and M_* are shown in the right and bottom panels. Overlaid in gray dotted and magenta dashed lines are the correlation between $M_{\rm BH}$ and bulge mass (McConnell & Ma 2013) and total stellar mass (Reines & Volonteri 2015), respectively.

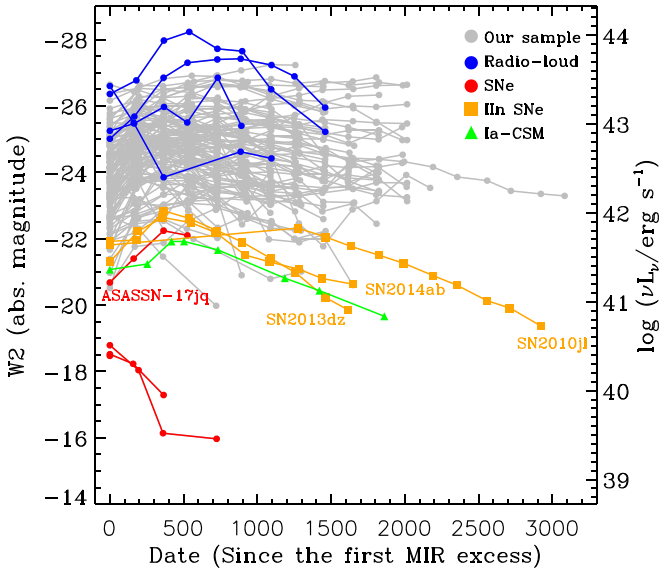

Figure 16. Time-resolved W2 magnitudes with date zero-point set as the time of first MIR excess. Our sample has been plotted in solid gray circles with the radio-loud sources and SNe highlighted in blue and red, respectively. We have also overplotted other IR-luminous SNe (orange squares), which are among the brightest known to us, for comparison. The Ia-CSM light curve (green triangles) is drawn from Fox et al. (2013).

radio emission for star-forming and composite galaxies is fully consistent with the expectation from the star formation. Only SDSS J1337+0035, which is a composite but shows extremely high radio power, is an exception. We then used the radio-loudness parameter R to quantify the radio intensity for AGN sources (Seyferts or LINERs) plus SDSS J1337+0035, which is defined as the ratio of the flux densities between 6 cm and 4400 Å (Kellermann et al. 1989). Here the 6 cm flux is derived from the 1.4 GHz flux assuming a spectral slope of −0.7. The 4400 Å flux is converted from the 5100 Å flux, which is derived from the bolometric luminosity ($L_{\rm bol}$). The latter is computed from the [O III] luminosity (Lamastra et al. 2009) assuming a bolometric correction of 8.1 (Runnoe et al. 2012). The derived radio-loudness parameters are listed in Table 4.

Four galaxies (SDSS J1046+1655, SDSS J1211+4047, SDSS J1337+0035, and SDSS J1348+1559) stand out from the rest in the above evaluations. They show radio power 38–600 times higher than that predicted from SFR. Meanwhile, their radio-loudness (>1000) is at least 2 orders of magnitude higher than other sources. Moreover, the radio luminosity for the four sources is higher than $10^{23.6}$ W Hz^{-1}, above which a radio-loud AGN can be classified (Kellermann et al. 2016). Therefore, they are likely radio-loud AGNs for which the MIR flares could originate from the nonthermal emission of preexisting jets. For those galaxies that are not radio-loud

Table 4
Radio Properties of FIRST-detected Objects

Name (1)	Type (2)	$F_{1.4}$ (3)	log $L_{1.4}$ (4)	log SFR (5)	$F'_{1.4}$ (6)	$F'_{1.4}/F_{1.4}$ (7)	R (8)	Class (9)
SDSS J0120−0829	Seyfert(b)	3.68	22.00	0.80	8.00	0.46	12	SF
SDSS J0205+0004	Star-forming	0.75	22.02	0.56	0.76	0.98	⋯	SF
SDSS J0745+2655	Seyfert(b)	3.09	23.01	1.60	7.97	0.39	3	SF
SDSS J0811+4054	Seyfert(b)	1.64	22.24	1.50	18.02	0.09	10	SF
SDSS J1046+1655	LINER	69.72	24.91	0.97	0.32	216	29226	Jet
SDSS J1105+5941	Seyfert(b)	5.96	22.19	0.66	5.62	1.06	12	w.Jet
SDSS J1114+4056	Seyfert(b)	1.28	22.89	0.66	0.24	5.30	26	w.Jet
SDSS J1129+5131	Composite	5.01	22.09	0.45	3.06	1.64	⋯	SF
SDSS J1200+0648	Seyfert	5.18	22.19	0.96	12.16	0.43	15	SF
SDSS J1211+4047	LINER	12.34	24.66	0.45	0.02	599	27722	Jet
SDSS J1303+2203	Seyfert	1.76	22.60	0.53	0.43	4.12	19	w.Jet
SDSS J1310+2518	Composite	1.83	23.09	1.19	1.09	1.69	⋯	SF
SDSS J1328+2752	Seyfert	3.09	22.80	0.34	0.27	11.46	26	w.Jet
SDSS J1337+0035	Composite	127.25	25.53	1.89	2.41	53	27566	Jet
SDSS J1348+1559	LINER	17.46	24.19	1.00	0.46	38	3952	Jet
SDSS J1406+0628	Star-forming	2.55	22.65	0.91	1.80	1.42	⋯	SF
SDSS J1430+2303	Seyfert(b)	1.63	22.41	0.28	0.28	5.77	13	w.Jet
SDSS J1442+5558	Composite	1.03	22.16	0.74	1.31	0.78	⋯	SF
SDSS J1504+0107	Seyfert	1.31	22.74	1.57	5.72	0.23	30	SF
SDSS J1533+2729	Seyfert(b)	3.04	22.57	0.55	0.83	3.66	11	w.Jet
SDSS J1557+2727	Composite	7.72	22.24	0.60	5.34	1.44	⋯	SF
SDSS J2156+0041	Seyfert(b)	1.19	21.91	0.27	0.65	1.84	8	w.Jet

Note. Column (1): name. Column (2): BPT type listed in Table 5. Column (3): radio flux at 1.4 GHz in units of millijanskys. Column (4): logarithmic radio luminosity at 1.4 GHz in units of watts per hertz after k-correction. Column (5): SFR estimated from SDSS+WISE SED fitting or W4 flux. Column (6): radio flux derived from SFR. Column (7): ratio between the observed radio flux and the predicted one from star formation. Column (8): radio-loudness parameter defined as the ratio of the monochromatic flux between 6 cm (5 GHz) and AGN continuum at 4400 Å ($f_{\nu,6\ \mathrm{cm}}/f_{\nu,4400\ \text{Å}}$). Column (9): main origin of radio emission. "SF": star formation. "Jet": undisputed intense jet emission. "w.Jet": jet likely contributed, since the observed radio flux is higher than the SFR prediction, but the radio power should be much weaker than "Jet," as R is not very high (<30).

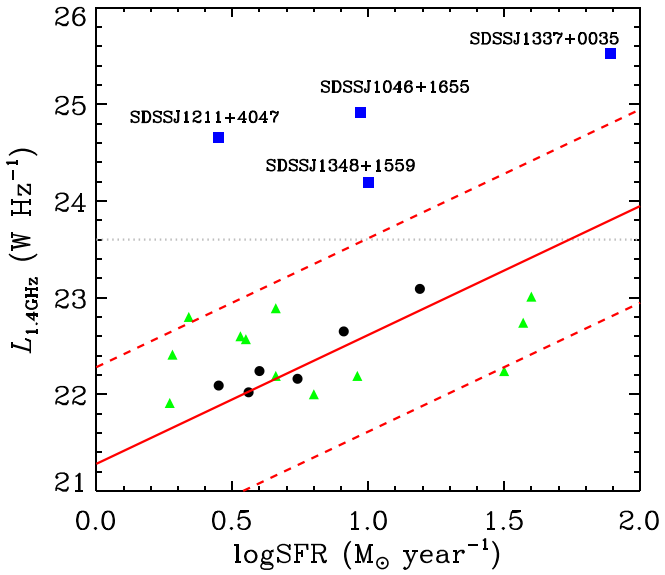

Figure 17. The 1.4 GHz luminosity vs. the SFR of the radio-detected sources in our sample. The red line is the expected radio emission from star formation (Equation (3) in Davies et al. 2017). One index offset from the expectation is plotted as red dashed lines. We have highlighted the radio-loud AGNs with blue squares and other AGNs (Seyferts or broad Hα objects) with green triangles. The gray dotted line represents the radio luminosity beyond which can be considered the undisputed jet origin (Kellermann et al. 2016).

before the MIR flare, we cannot rule out the probability of a new-formed relativistic jet contributing the MIR emission. Unfortunately, no quasi-simultaneous radio observations are available. In fact, by examining the WISE light curves in each epoch, we did not find any evidence for intraday variability, which could indicate the presence of a relativistic jet (Jiang et al. 2012). Timely radio follow-ups would be helpful to further test this intriguing scenario.

6.3. Dust Echo of Transient SMBH Accretion

After removing the four known SNe and four radio-loud sources, we now investigate the origin of MIR outbursts for the other 129 galaxies in our sample. As we analyzed in Section 5.2, there are 49 galaxies that show evidence of AGN activity in their optical spectra. In addition, 16 galaxies can be classified as LINERs. Therefore, the 128 galaxies (except SDSS J1422+0609, for which the SDSS spectrum is not available) can be grouped into two populations, including 65 AGNs (49 Seyferts and 16 LINERs) and 63 quiescent galaxies.

6.3.1. Echoes of Turn-on AGNs

The UV/optical variability on various timescales is well known to be an inherent property of AGNs, albeit the physical mechanism behind it is not fully understood (Ulrich et al. 1997). The amplitude of optical variability is typically a few tenths of a magnitude within a timescale of months but also showing larger variations over longer timescales. There is an increasing population of dramatically variable AGNs, so-called CL AGNs, that exhibit flux rising/declining in continuum ($\Delta m > 1$ mag) over several years and change the spectral types accordingly (e.g., LaMassa et al. 2015; MacLeod et al. 2016;

Table 5
The Properties of the Host Galaxies and BH

Name (1)	M_r (2)	$g-r$ (3)	$\sigma_\star$ (4)	log M_* (5)	log SFR (6)	log $M_{\rm BH}$ (7)	Type (8)
SDSS J0000+1438	−21.54	0.89	192.	11.11	−0.13	8.23	Seyfert
SDSS J0027+0713	−21.48	0.96	154.	11.05	0.89	7.68	Seyfert
SDSS J0045−0047	−19.48	0.41	44.9	9.604	−0.10	6.00	Star-forming
SDSS J0103+1401	−21.39	0.71	94.2	10.73	0.94	6.47	Star-forming
SDSS J0120−0829	−20.83	0.79	115.	10.73	0.80	6.79	Seyfert(b)
SDSS J0121+1405	−21.49	0.77	130.	10.91	0.49	7.26	Star-forming
SDSS J0158−0052	−19.49	0.61	45.4	10.15	−0.09	6.37	Star-forming(b)
SDSS J0205+0004	−20.44	0.71	112.	10.55	0.56	6.92	Star-forming
SDSS J0745+2655	−21.46	0.40	123.	10.18	1.60	7.22	Seyfert(b)
SDSS J0757+1908	−21.19	0.71	131.	10.59	0.40	7.29	Composite
SDSS J0811+4054	−20.37	0.65	120.	10.16	1.50	6.81	Seyfert(b)
SDSS J0814+2611	−21.02	0.92	176.	10.78	0.32	8.01	Star-forming
SDSS J0814+5337	−21.51	0.71	165.	10.84	0.44	7.86	Star-forming
SDSS J0835+4935	−21.42	0.76	128.	10.77	−3.34	7.23	Composite
SDSS J0837+4143	−21.48	0.92	167.	10.92	0.47	7.88	Composite
SDSS J0841+0526	−22.36	0.91	145.	11.32	0.69	8.28	LINER(b)
SDSS J0842+2357	−20.69	0.74	61.1	10.53	0.29	5.41	Star-forming
SDSS J0847+5142	−21.12	0.70	134.	10.67	0.46	7.35	Star-forming
SDSS J0854+1113	−22.82	0.95	281.	11.60	1.29	7.63	LINER(b)
SDSS J0858+4121	−20.19	0.91	127.	10.46	−4.38	7.22	Composite
SDSS J0859+0922	−21.94	0.60	66.1	10.88	0.79	5.60	Star-forming
SDSS J0909+1920	−20.65	0.79	101.	10.54	−0.87	6.66	Composite
SDSS J0915+4814	−21.64	0.99	138.	10.85	−0.52	7.42	LINER
SDSS J0931+6626	−20.82	1.06	147.	10.92	−4.06	7.56	LINER
SDSS J0936+0615	−16.10	0.51	26.4	8.175	−1.67	4.57	Star-forming
SDSS J0943+5958	−20.07	0.88	97.4	10.44	−4.41	6.55	LINER
SDSS J0944+3105	−22.03	0.67	147.	11.10	−0.09	7.58	Composite
SDSS J0957+0207	−21.03	0.85	123.	10.73	0.23	7.14	Composite
SDSS J1001+1829	−20.73	0.73	94.5	10.26	−0.17	6.48	Star-forming
SDSS J1002+4424	−22.43	0.93	223.	11.39	−3.48	8.58	LINER
SDSS J1003+0202	−21.20	0.90	115.	10.75	0.06	6.96	Seyfert
SDSS J1008+1549	−21.63	0.80	139.	11.04	0.92	7.44	Seyfert
SDSS J1009+3436	−22.20	0.74	109.	11.00	1.30	6.84	Composite
SDSS J1009+2209	−21.88	0.91	182.	11.24	0.62	7.97	Seyfert(b)
SDSS J1011+5348	−22.36	1.08	246.	11.38	0.20	8.82	LINER
SDSS J1017+1224	−20.49	0.77	120.	10.57	−0.04	7.07	Seyfert
SDSS J1020+2515	−21.32	0.47	65.8	10.16	0.54	5.59	Star-forming
SDSS J1029+2526	−21.98	0.41	41.3	10.52	1.30	6.59	Star-forming(b)
SDSS J1029+4829	−22.31	0.31	123.	10.68	1.67	7.47	Seyfert(b)
SDSS J1037+3912	−20.58	0.72	81.6	10.50	0.31	6.12	Star-forming
SDSS J1041+3412	−21.54	0.72	129.	10.73	0.48	7.32	Composite(b)
SDSS J1043+2716	−20.89	0.79	101.	10.37	−0.13	6.65	Composite
SDSS J1046+1655	−22.44	0.92	220.	11.42	0.97	8.55	LINER
SDSS J1051+2101	−20.12	0.86	104.	10.39	−0.16	6.71	Seyfert
SDSS J1053+5524	−21.97	0.51	51.4	10.87	1.10	4.99	Star-forming
SDSS J1058+5444	−21.33	0.56	90.7	10.58	0.63	6.38	Star-forming
SDSS J1105+5941	−21.17	0.64	122.	10.80	0.66	7.03	Seyfert(b)
SDSS J1109+3708	−20.84	0.75	150.	10.58	−4.15	7.62	LINER
SDSS J1111+5923	−22.02	0.74	169.	10.79	0.21	7.91	Composite
SDSS J1114+4056	−21.65	0.96	214.	11.33	0.66	8.10	Seyfert(b)
SDSS J1115+0544	−20.70	0.98	125.	10.75	−1.90	7.18	LINER
SDSS J1120+1933	−21.62	0.61	131.	10.76	1.14	7.28	Composite
SDSS J1122+1433	−22.19	0.86	216.	11.33	1.47	7.90	Seyfert(b)
SDSS J1124+0455	−21.27	0.68	94.4	10.27	0.78	6.48	Composite
SDSS J1129+5131	−20.94	0.74	111.	10.74	0.45	6.89	Composite
SDSS J1133+6701	−21.38	0.82	142.	10.91	−0.36	7.53	LINER(b)
SDSS J1139+6134	−21.87	0.47	113.	10.81	1.00	6.94	Star-forming
SDSS J1149+5441	−20.96	0.75	101.	10.30	0.23	6.65	Star-forming
SDSS J1152+4850	−21.51	0.71	171.	10.46	0.89	7.94	Composite
SDSS J1153+4037	−21.45	0.49	95.5	10.27	0.89	6.51	Star-forming
SDSS J1200+0648	−21.53	0.89	166.	11.12	0.96	7.87	Seyfert
SDSS J1201+3525	−22.31	0.84	182.	11.23	0.56	8.09	Seyfert
SDSS J1203+5859	−18.76	0.61	57.3	9.198	−0.63	5.26	Star-forming

Table 5
(Continued)

Name (1)	M_r (2)	$g-r$ (3)	$\sigma_\star$ (4)	log M_* (5)	log SFR (6)	log $M_{\rm BH}$ (7)	Type (8)
SDSS J1208+3305	−21.86	1.02	261.	11.24	1.63	8.97	Seyfert
SDSS J1209+3202	−21.21	0.82	148.	10.78	0.40	7.58	Seyfert
SDSS J1211+4047	−22.06	1.07	175.	11.21	0.45	7.99	LINER
SDSS J1214+1014	−21.39	0.60	44.7	10.69	0.55	7.09	Seyfert
SDSS J1218+2951	−21.55	0.57	127.	10.61	0.56	7.22	Composite
SDSS J1219+0516	−20.24	0.77	47.2	10.30	−0.06	6.70	Composite
SDSS J1228+3617	−21.36	0.67	81.9	10.58	0.29	6.13	Star-forming
SDSS J1238+0815	−21.07	0.70	150.	10.36	0.67	7.62	Seyfert
SDSS J1242+2537	−20.25	0.93	116.	10.49	−4.44	6.99	Composite
SDSS J1245−0147	−22.34	0.61	127.	10.92	0.24	7.32	LINER
SDSS J1303+2203	−21.42	0.92	171.	10.93	0.53	7.71	Seyfert
SDSS J1305+3953	−20.72	0.93	163.	10.67	−3.28	7.82	LINER
SDSS J1308+0429	−20.86	0.95	161.	10.76	−4.18	7.79	Seyfert
SDSS J1310+2518	−21.58	0.71	149.	10.63	1.19	7.61	Composite
SDSS J1315+0727	−21.86	0.85	154.	11.00	0.46	6.53	Composite(b)
SDSS J1322+3301	−21.63	0.82	123.	10.96	0.93	7.13	LINER
SDSS J1328+2752	−21.11	0.88	174.	10.76	0.34	7.98	Seyfert
SDSS J1329+2341	−20.54	0.83	105.	10.40	−0.29	6.74	Composite
SDSS J1332+2036	−21.39	0.77	74.3	10.83	0.89	6.53	Composite(b)
SDSS J1337+0035	−22.58	0.73	209.	11.33	1.89	8.43	Composite
SDSS J1340+1842	−20.46	0.91	132.	10.57	−0.53	6.81	Seyfert(b)
SDSS J1341−0049	−21.95	0.67	176.	10.77	1.21	7.70	Seyfert(b)
SDSS J1341+1516	−21.65	0.76	145.	10.65	0.47	7.53	Composite
SDSS J1348+1559	−21.72	0.95	246.	11.22	1.00	8.83	LINER
SDSS J1352+0009	−22.17	0.73	124.	10.83	0.20	7.16	LINER
SDSS J1402+3922	−20.76	0.64	128.	10.31	−0.26	6.57	Seyfert(b)
SDSS J1406+0628	−21.42	0.74	139.	10.85	0.91	7.43	Star-forming
SDSS J1409+1057	−22.26	0.75	180.	10.74	−0.39	8.06	LINER
SDSS J1412+4114	−21.50	0.94	165.	11.11	−3.84	7.85	Composite
SDSS J1422+0609	−21.96	0.85	…	11.21	0.47	7.61	…
SDSS J1424+6249	−21.79	0.90	182.	11.08	0.16	8.09	Composite
SDSS J1428−0231	−18.68	0.83	98.8	9.532	−0.11	6.59	Composite(b)
SDSS J1430+2303	−21.04	1.01	183.	11.15	0.28	7.91	Seyfert(b)
SDSS J1440+1758	−20.65	0.79	79.1	10.43	−0.27	6.04	Composite
SDSS J1442+5558	−21.80	0.73	174.	10.60	0.74	7.98	Composite
SDSS J1447+4023	−21.53	0.91	163.	11.24	−0.36	7.82	LINER
SDSS J1448+1137	−21.09	0.80	101.	10.57	0.09	6.97	Star-forming
SDSS J1504+0107	−22.15	0.86	181.	11.24	1.57	8.07	Seyfert
SDSS J1508+2602	−20.73	0.67	69.0	10.05	0.37	5.71	Composite
SDSS J1511+2214	−21.45	1.02	225.	11.16	0.07	8.61	Seyfert
SDSS J1512+2809	−21.39	0.93	152.	11.09	−3.89	7.65	LINER
SDSS J1513+3111	−21.22	0.69	103.	10.63	−0.15	6.70	Composite
SDSS J1524+5314	−20.08	0.60	78.0	10.38	0.11	6.01	Star-forming
SDSS J1531+3724	−16.99	0.43	23.9	8.375	−0.91	4.77	Star-forming
SDSS J1533+2729	−21.37	0.95	196.	11.01	0.55	8.14	Seyfert(b)
SDSS J1537+5814	−20.45	0.84	86.0	10.53	0.70	7.23	Seyfert(b)
SDSS J1540+0054	−16.66	0.40	33.4	8.231	−1.80	4.63	Star-forming
SDSS J1541+0718	−21.34	0.65	140.	10.81	0.63	7.45	Star-forming
SDSS J1548+2208	−19.01	0.93	73.7	9.976	−1.39	5.87	Composite
SDSS J1549+3327	−20.12	0.58	64.8	9.796	−0.05	5.56	Star-forming
SDSS J1554+5255	−20.92	0.72	111.	10.50	−0.23	6.89	Composite
SDSS J1554+1636	−15.98	0.42	79.8	7.946	−1.50	4.34	Star-forming
SDSS J1554+3629	−22.04	0.81	182.	11.13	0.83	8.08	LINER
SDSS J1555+2120	−20.10	1.27	135.	10.88	−3.09	7.35	Composite
SDSS J1556+4513	−21.04	0.75	170.	10.88	1.15	7.92	Seyfert
SDSS J1557+2727	−20.43	0.94	111.	10.36	0.60	6.89	Composite
SDSS J1600+4612	−22.30	0.77	161.	11.16	−0.67	7.80	Star-forming
SDSS J1612+1416	−20.53	0.87	123.	10.60	0.06	7.14	Composite
SDSS J1620+2407	−20.76	0.70	102.	10.04	−1.02	6.67	Star-forming
SDSS J1628+4810	−21.25	0.48	61.4	10.11	0.70	5.43	Star-forming
SDSS J1632+4416	−20.51	0.88	158.	10.59	−4.26	7.74	LINER
SDSS J1647+3843	−20.28	0.62	63.2	10.47	0.21	5.49	Star-forming

Table 5
(Continued)

Name (1)	M_r (2)	$g-r$ (3)	$\sigma_\star$ (4)	log M_* (5)	log SFR (6)	log $M_{\rm BH}$ (7)	Type (8)
SDSS J1657+2345	−19.30	0.68	48.7	9.515	0.15	5.91	Seyfert
SDSS J1659+2049	−21.67	0.87	148.	10.80	−0.02	7.58	Seyfert
SDSS J2115−0011	−21.66	1.01	178.	11.17	1.41	7.48	Seyfert(b)
SDSS J2141−0857	−20.50	0.79	106.	10.50	−0.41	6.77	Seyfert
SDSS J2146+1041	−21.80	0.54	121.	10.55	0.80	7.09	Star-forming
SDSS J2150−0106	−18.97	1.00	70.3	10.05	−0.64	5.76	Seyfert
SDSS J2156+0041	−20.75	0.87	114.	10.59	0.27	6.59	Seyfert(b)
SDSS J2203+1124	−21.71	0.98	152.	10.74	−0.19	7.64	Composite
SDSS J2215−0107	−21.40	1.01	107.	11.02	−0.10	6.79	Composite
SDSS J2310+2220	−20.65	1.09	127.	10.89	0.57	7.22	Seyfert
SDSS J2312+1335	−21.43	0.90	172.	10.91	0.77	7.95	Composite
SDSS J2324+1542	−21.36	0.83	140.	10.94	0.42	7.83	Composite(b)

Note. Column (1): SDSS name. Columns (2) and (3): SDSS r-band absolute magnitude and $g-r$ color after k-correction to 0.1. Column (4): stellar velocity dispersion. Column (5): stellar mass. Column (6): estimated BH mass. Column (7): classification in the BPT diagram, with suffix "(b)" highlighting robust broad Hα detection. Column (8): logarithmic SFR in units of solar mass per year (see Section 6.2).

Runnoe et al. 2016; Yang et al. 2018). Specifically, the CL AGNs with rising/declining photometric light curves are termed turn-on/turn-off. In addition to state changes found in CL AGNs, major outbursts have also been found in AGNs (e.g., Graham et al. 2017; Trakhtenbrot et al. 2019).

In AGN unification, the dusty torus is a vital ingredient to address a variety of phenomena in different types of AGNs. The torus will unavoidably absorb part of the UV-optical photons from the accretion disk and reprocess them into the IR. The picture has been widely accepted through SED fitting (e.g., Fritz et al. 2006; Nenkova et al. 2008; Stalevski et al. 2012) and IR reverberation mapping (e.g., Suganuma et al. 2006; Koshida et al. 2014; Lyu et al. 2019). It is plausible that our discovered MIR flares are due to dust echoes of turn-on AGNs. Such a scenario can be tested by obtaining new optical spectra to see whether there is evident spectral evolution. In fact, we have performed a detailed study of SDSS J1115+0544, which has undergone a brightening by 2.5 mag in the V band over ∼120 days, then faded by 0.5 mag over 200 days, followed by a plateau lasting for >600 days. The multi-epoch optical spectra over 400 days in the plateau phase revealed newly formed and steady broad Hα and Hβ emission that is compatible with the characteristics of a turn-on AGN (Yan et al. 2019). Intriguingly, together with the three objects (SDSS J1554+3629, SDSS J0945+4814, and SDSS J1133+6701) mentioned in Section 3.1, the four reported sources are all classified as LINERs in the BPT diagram, which may suggest a uniform class of the turn-on system (Frederick et al. 2019).

6.3.2. Echoes of TDEs

Nearly half of the objects in our sample show no signs of AGN activity, neither Seyfert nor LINER, in the SDSS spectra. The giant nuclear flares of inactive galaxies are usually attributed to TDEs. For Schwarzschild BHs, the TDEs are observable only when the BH masses are lower than the Hills mass (∼10^8 $M_\odot$). Otherwise, the star will be swallowed whole rather than produce an electromagnetically luminous flare because its tidal radius is within the horizon (Hills 1975; Rees 1988). The $M_{\rm BH}$ distribution of our sample peaks at 2.0×10^7 $M_{\rm BH}$ with only 17 (12.4%) greater than 10^8 $M_\odot$ (see Figure 15). If excluding Seyferts and LINERs, only three galaxies are more massive than the Hills mass

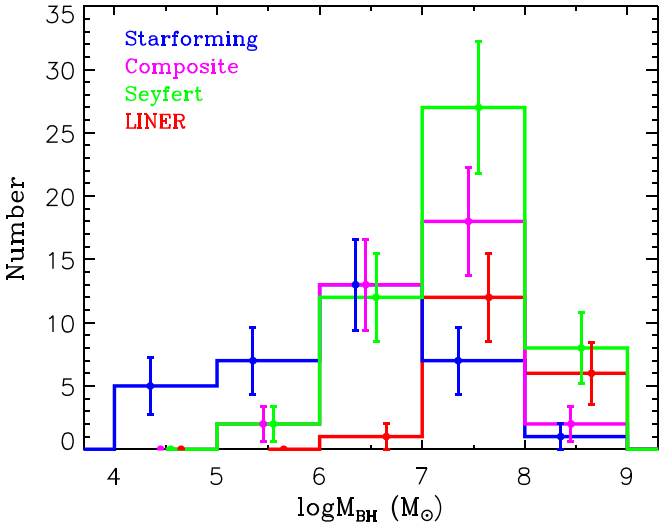

Figure 18. Histograms of $M_{\rm BH}$ for star-forming (blue), composite (magenta), Seyfert (green), and LINER (red) galaxies in our sample as classified by the BPT diagram. The error bars are the Poisson fluctuations of the number in each bin. Note that we have put all broad-line sources into the "Seyfert" subset, whatever their BPT types are.

(see Figure 18); hence, the TDE interpretation for the MIR bursts is possible.

Similar to AGNs, the UV/optical photons released by TDEs can be absorbed by dust in the vicinity of the BH and reprocessed into the IR band, giving rise to an IR flare like an echo. Lu et al. (2016) calculated the light curve of the IR echo with a 1D radiative transfer model and showed that the dust emission peaks at MIR (3–10 μm). They have predicted that the typical luminosity is between 10^{42} and 10^{43} erg s^{-1}, depending on the dust covering factor (ranging from 0.1 to 1), which is fairly comparable with that inferred in our sample. Such an IR echo has been detected in a handful of optical TDEs from the WISE data (Jiang et al. 2016; van Velzen et al. 2016), though the amplitude of the IR variability is smaller (∼0.2 mag) compared with the sample in this work. Furthermore, Dou et al. (2016) reported the long-lasting IR echoes from four coronal-line TDE candidates (Wang et al. 2012; Yang et al. 2013). These findings suggest that

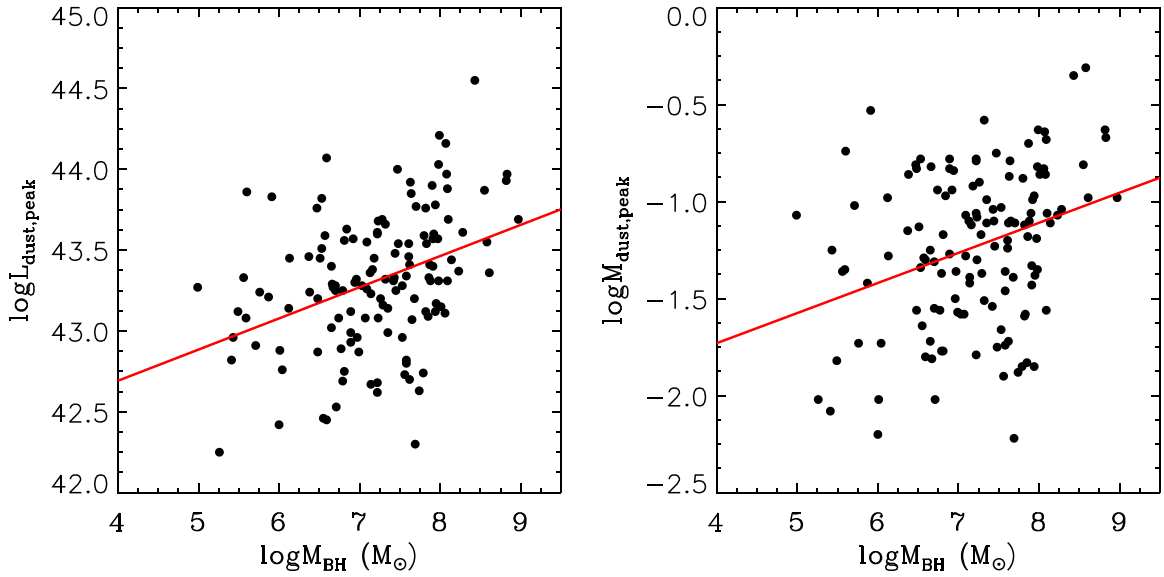

Figure 19. Left panel: correlation between peak MIR luminosity (L_d) and $M_{\rm BH}$. Right panel: correlation between inferred dust mass (M_d) and $M_{\rm BH}$. Overlaid in red is the linear least-squares fitting. The L_d and M_d values are derived by dust with absorption efficiency (see Table 3).

IR echoes might be ubiquitous for TDEs occurring in a gas (dust)-rich nuclear environment.

On the other hand, the IR echo itself is suggestive of TDEs in a dust-rich environment. Wang et al. (2018) conducted a systematical search and obtained a sample of 19 low-redshift ($z < 0.22$) non-Seyfert galaxies that display a slow decline in the MIR emission, reminiscent of those coronal-line TDEs (Dou et al. 2016). Unfortunately, because they are already in the late fading stage, the spectroscopic observations might be too late to identify the TDE-like characteristics. In contrast, our objects are observed at a much earlier phase, either still rising or just decaying, which is valuable for timely multiwavelength follow-ups. By checking for optical counterparts (see Section 3.1), we found that SDSS J0158–0052 (PS16dtm) and SDSS J1620 +2407 (ATLAS17jrp) have indeed been alerted as TDE candidates (Blanchard et al. 2017; Fraser et al. 2017). The identifications of TDEs in our sample are thus encouraged. We caution that even for active galaxies in our sample, the TDE scenario is possible and worthwhile to explore. One universal manifestation accompanying AGN TDEs (e.g., Blanchard et al. 2017; Kankare et al. 2017; Tadhunter et al. 2017) is the long-lasting and luminous MIR flares as a result of the echoes of the dusty torus (Dou et al. 2017; Jiang et al. 2017, 2019).

Given the faintness in the optical bands for most MIRONG (Section 3.1), they could be promising candidates of dust-obscured TDEs that are still poorly explored. If not due to obscuration, their optical emission should be otherwise intrinsically weak, which is especially possible in the TDE scenario. The electromagnetic output of TDEs was initially thought to be dominated by X-ray or FUV emission from accretion, making the origin of optical emission hotly disputed (Roth et al. 2020). Therefore, some objects in our sample could belong to classical TDEs, which are luminous in the X-ray/FUV but faint in the optical band. In this sense, the IR search of TDEs is superior to other individual bands as long as the BH is set in a dusty environment.

Based on the sample of 19 galaxies, Wang et al. (2018) found that the peak MIR luminosity is well correlated with the $M_{\rm BH}$. However, the correlation (excluding SNe) appears less significant in our sample presented here (see Figure 19), though a Spearman rank analysis gives a correlation coefficient of $\rho = 0.377$, corresponding to a null hypothesis probability of $p = 8 \times 10^{-6}$. If we examine the dust mass instead of luminosity, the correlation is even less obvious ($\rho = 0.116$, $p = 0.001$).

7. Discussion

Similar to Wang et al. (2018), our tentative conclusion is that the MIRONG discovered by us are most likely associated with transient SMBH accretion in the form of either TDEs or turn-on AGN activity. Only a small fraction of them are due to IR-luminous SNe or nonthermal emission from relativistic jets. The conclusions are supported by several lines of evidence: (1) the outburst locations prefer to be in the region very close to the galactic center, (2) the maximum MIR luminosity is higher than the brightest SNe by 1–2 orders, (3) only a few have radio-loud jet emission before the outburst, and (4) the luminosity function broadly agrees with the results of optical and X-ray TDEs (or nuclear transients).

In order to differentiate the diverse nature of these MIRONG, multiwavelength follow-up observations have been conducted, including optical spectra (Y. B. Wang et al. 2020, in preparation), NIR photometry (H. Liu et al. 2020, in preparation), and radio (Dai et al. 2020) and X-ray observations. So far, we have successfully obtained a sizable sample of likely TDEs or turn-on AGNs, which will be reported in the following series of papers. These events are generally not detected in the optical band and thus largely overlooked by previous works; hence, they present a significant advance over previous studies of similar events.

7.1. TDE Demography and Missing Energy Puzzle

The observations of TDEs were initially restricted to the serendipitous discoveries of X-ray flares in the centers of galaxies, yielding a very limited number of candidates. The number has grown remarkably in the past decade with the advent of dedicated optical time-domain surveys (Komossa 2015; van Velzen et al. 2020). However, there is still a large discrepancy in the event rate between observation and theory (Stone et al. 2020). The observations usually find a rate of $\sim 10^{-5}$ galaxy^{-1} yr^{-1} (Donley

et al. 2002; van Velzen & Farrar 2014), which is at least an order of magnitude below the theoretical estimation in realistic galactic nuclei (Wang & Merritt 2004; Stone & Metzger 2016). Although dynamical mechanisms to suppress TDE rates have been proposed, they seem unlikely to work in practice (e.g., Lezhnin & Vasiliev 2015). One solution may be a very broad intrinsic TDE luminosity function of which we have so far only seen the high end at a given band (e.g., Blagorodnova et al. 2017; van Velzen 2018) in view of the complicated radiative emission mechanisms (Roth et al. 2020). The TDE demography at any single band can thus be seriously underestimated.

Moreover, the rate discrepancy becomes more specific and definitive when optical TDEs are found to be overrepresented in poststarburst (or so-called E+A) galaxies with the rate elevated by a factor of ∼100 (e.g., Arcavi et al. 2014; French et al. 2016). This preference cannot be fully accounted for by selection effects in comparison with control samples (Law-Smith et al. 2017). Such an enhancement is difficult to understand in theory, even though their hosts show high central stellar densities (French et al. 2020). This would require violent dynamical processes to occur, but it seems impossible in most poststarburst galaxies.

Another observational discrepancy is known as the missing energy puzzle, namely, a huge shortage of the observed energy relative to predictions. In the simplest picture, if half of the stellar material is accreted onto the BH, the expected energy released is $\sim 10^{52}$–10^{53} erg. The observed total energy of optical TDEs is only $\sim 10^{51}$ erg. Where is the missing 90%–99% of the energy? Some models argue that the real accretion efficiency is actually quite low due to advection or outflow (e.g., Svirski et al. 2017; Dai et al. 2018). Lu & Kumar (2018) suggested that the missing part may be in the unobserved extreme-UV (EUV) band and/or in the form of relativistic jets. The jet mode is disfavored because of the rareness of jetted TDEs, but the EUV option coincides with the theoretical peak and the Rayleigh–Jeans-like optical/NUV SED. If that is true, at least in several TDEs, the issue then becomes how to measure the EUV energy that is not directly visible.

Two recent studies may shed light on an avenue to solve or alleviate the puzzles above. Tadhunter et al. (2017) reported a candidate TDE in F01004-2237 from a sample of 15 nearby ultraluminous infrared galaxies (ULIRGs), suggesting an event rate as high as $\sim 10^{-2}$ galaxy^{-1} yr^{-1}. The ULIRGs are generally starburst systems with a large amount of dust that is able to veil even energetic outbursts like TDEs. In the meantime, the energy absorbed by dust will manifest the original TDE emission as a luminous IR echo. The picture is nicely corroborated by the huge MIR flare detected in F01004-2237 (Dou et al. 2017), whose integrated IR energy until now was $>3 \times 10^{52}$ erg. The other work claims a dust-enshrouded TDE in the western nucleus (B) of the merging galaxy pair Arp 299 (Mattila et al. 2018). This event is almost silent in the optical and X-ray but displays long-lasting echoes in the NIR and MIR with a total radiated energy $>1.5 \times 10^{52}$ erg. The missing energy puzzle is almost settled in both systems when the IR energy is taken into account.

The two case studies also hint that perhaps the TDEs in poststarburst systems are only the tip of the iceberg, and the real TDE rate in starburst galaxies could be immense (Guillochon 2017). It is widely believed that galaxy mergers or interactions are capable of driving galactic-scale gas inflow to the nuclear region and triggering intense star formation. Even for an isolated disk galaxy, its center could be a concentrated region of gas and dust ornamented by enhanced star formation. Indeed, a considerable fraction of galaxies in the MIRONG sample are star-forming systems, as indicated by their SDSS fiber spectrum, whose nuclei are easily obscured as a result of intense star formation processes.

Interestingly, the MIRONG event rate estimated by us is 5.4×10^{-5} galaxy^{-1} yr^{-1} (see Section 4.1), which is comparable to that of optical TDEs. It would be of great value if a large percentage of them were eventually confirmed as real TDEs. Furthermore, if we naively assume a typical dust covering factor as the AGN torus, the inferred luminosity function of the MIRONG is comparable with the observations of X-ray (Auchettl et al. 2018) and optical TDEs (van Velzen 2018) at the high end (see Figure 10). The faint-end discrepancy is at least partly caused by the imperfect correction for the sample completeness of various selection approaches. We emphasize again that our selection criteria are somewhat strict (>0.5 mag brightening). In the future, we will extend the sample by a relaxed requirement to obtain a more complete view of the event rate and the luminosity function at the faint end. The new population that is largely missed by optical surveys due to either dust obscuration or intrinsic faintness may offer us a promising approach to solve the problems of TDE demographics and missing energy.

7.2. Implication for the Turn-on and Duty Cycle of AGNs

The CL AGNs have gradually become a rather popular phenomenon. Early searching has been focused mainly on known quasars, which naturally yield more turn-off AGNs. The systematic discovery of turn-on cases has to start from a much larger galaxy sample, consisting of both Seyfert and normal galaxies. Galaxies that show rapid transformation from a quiescent galaxy to a type 1 AGN within several months to years are of great interest. So far, only two unambiguous systems (iPTF 16bco and SDSS J1115+0544) have been reported (Gezari et al. 2017; Yan et al. 2019). We refer to them as "bona fide" turn-on AGNs, which are different from the normal CL AGNs that usually change from type 2/1.9/1.8 to type 1. Some CL AGNs have been shown to change their types back and forth frequently (e.g., Denney et al. 2014; McElroy et al. 2016; Oknyansky et al. 2019), implying the existence of a persistent but unstable accretion disk, e.g., susceptible and sensitive to gas feeding. In comparison, the bona fide turn-on AGNs can serve as a more genuine laboratory than normal CL AGNs to explore the ignition mechanism of SMBHs, e.g., the rapid formation of an accretion disk, as well as the origin of concomitant multiwavelength emission (e.g., X-ray, radio).

It is worthwhile to note that both iPTF 16bco and SDSS J1115+0544 are present in our MIRONG sample. This suggests that more similar systems would be present in our sample in view of the quiescence of many galaxies before the outburst, and the selection of turn-on AGNs might be effectively using the MIR light curves. The dust covering factors (f_d) of quiescent SMBHs are around 10^{-2}, as revealed by the IR echoes of optical TDEs, which is at least 1 order of magnitude lower than that in AGNs (van Velzen et al. 2016; Jiang et al. 2021). We estimated the f_d of turn-on AGNs with a similar method used in Jiang et al. (2021), which is $f_d = L_{\rm dust}/L_{\rm bol}$. The $L_{\rm bol}$ of iPTF 16bco and SDSS J1115+0544 after state transformation is $\sim 10^{45}$ (Gezari et al. 2017) and $\sim 4 \times 10^{44}$ (Yan et al. 2019) erg s^{-1}, respectively. Meanwhile, their peak dust luminosity ($L_{\rm dust}$) inferred from WISE W1 and W2

photometry (fitted by blackbody radiation) is $\sim 10^{44}$ and 3×10^{43} erg s^{-1}, respectively. The inferred f_d ($\sim$0.1) for turn-on AGNs appears to fall within the regime connecting normal galaxies and AGNs. The result is interesting and may shed important light on the triggering mechanism of AGNs, which is perhaps regulated by the availability of the interstellar medium in the vicinity of SMBHs.

If turn-on AGNs occur only when a large amount of gas and dust accumulate around the SMBHs, the dust echo appears inevitable, explaining the high efficiency of searching in MIR. Particularly in extremely dusty environments, the ignited SMBHs can be severely obscured and only identified in the IR (Section 7.1). Uncovering more bona fide turn-on AGNs is valuable not only for understanding the AGN accretion physics but also for the probe of the AGN duty cycle, as well as the impact on their host galaxies. The duty cycle, namely, the accreting phase of an SMBH (i.e., AGN phase), is considered to be roughly a few $\times 10^7$ yr (Haehnelt & Rees 1993; Combes et al. 2000). However, the turn-on timescale is found within 1 yr (Gezari et al. 2017; Yan et al. 2019), indicating that the event rate could be as low as $\sim 10^{-7}$. Such a low expected rate seems contrary to the discovery of two and possibly more cases in our sample. Perhaps the traditional duty cycle of 10^7 yr is only suitable for the total active time but not appropriate for flare events, which may have different timescales. Current and future surveys may be able to constrain the timescale distribution with a large number of newly discovered turn-on AGNs. The specific mode of the AGN duty cycle may have a distinctive influence on the host galaxies and advance our understanding of galaxy evolution.

8. Summary and Prospects

The combined WISE and NEOWISE light curves, which have a time baseline of about one decade with a cadence of half a year, have provided us a unique data set for MIR time-domain study. Starting from $\sim$1 million SDSS galaxies, we have selected 137 galaxies that have displayed MIR outbursts with amplitudes >0.5 mag with respect to the preoutburst quiescent phase. Only a small fraction (15/137) of these outbursts have been reported by optical surveys, including four SNe, two TDE candidates, three turn-on AGNs, and six unclassified objects. The remaining sources are likely associated with the dust echoes of transient accretion events of SMBHs, as suggested by their proximity to the host galaxy centers, high MIR luminosity, weak radio emission, and MIR luminosity distribution, i.e., luminosity function. We are undertaking multiwavelength follow-up observations to identify the nature of these MIRONG. The MIRONG unveiled by our study demonstrate the importance and necessity of MIR time-domain surveys. For example, they may pave the way to solving the perplexing issues in the current study of TDEs and CL AGNs.

Since the NEOWISE survey is ongoing, we expect that more data points will be accumulated in the future. Additional data will help us diagnose the nature of MIR outbursts and obtain better measurements of dust properties. In addition, more MIR transients will be discovered with the updated database. In the post-WISE era, the Near-Earth Object Camera (NEOCam) is a planned mission to discover and characterize asteroids and comets at two MIR channels simultaneously, which will cover 68% of the extragalactic sky at wavelengths of 4.0–5.2 and 6.0–10.0 μm, respectively (Ross et al. 2019). The survey depth of NEOCam is quite similar to NEOWISE, yet its cadence is even better with, on average, 30 visits yr^{-1}. Moreover, the already selected SPHEREx mission (Doré et al. 2016) that is scheduled to launch in 2023 will be an excellent complement to NEOCam at the near-IR band, aiming to obtain spectra over 0.75–5 μm across the full sky. It will scan the entire sky four times during its nominal 25 month mission life, though it is not as deep as WISE. Therefore, the prospects for the study of MIR transients are still very bright.

We are grateful to the anonymous referee for a careful reading and nice comments, which have greatly improved the paper. We thank Dr. Roc Cutri for many useful suggestions about the use of WISE and NEOWISE archival data and Dr. John Moustakas for his kind help with the usage of `IDL/iSEDfit`. This work is supported by the Chinese Science Foundation (NSFC-11833007, 12073025, 11421303, 11733001), Joint Research Fund in Astronomy (U1731104) under cooperative agreement between the NSFC and the CAS, Anhui Provincial Natural Science Foundation, and the Fundamental Research Funds for the Central Universities. This research makes use of data products from the Wide-field Infrared Survey Explorer, which is a joint project of the University of California, Los Angeles, and the Jet Propulsion Laboratory/California Institute of Technology, funded by the National Aeronautics and Space Administration. This research also makes use of data products from NEOWISE-R, which is a project of the Jet Propulsion Laboratory/California Institute of Technology, funded by the Planetary Science Division of the National Aeronautics and Space Administration. This research has made use of the NASA/IPAC Infrared Science Archive, which is operated by the California Institute of Technology, under contract with the National Aeronautics and Space Administration. This research has made use of the NASA/IPAC Extragalactic Database (NED), which is operated by the Jet Propulsion Laboratory, California Institute of Technology, under contract with the National Aeronautics and Space Administration.

ORCID iDs

Ning Jiang https://orcid.org/0000-0002-7152-3621
Tinggui Wang https://orcid.org/0000-0002-1517-6792
Liming Dou https://orcid.org/0000-0002-4757-8622
Xinwen Shu https://orcid.org/0000-0002-7020-4290
Lin Yan https://orcid.org/0000-0003-1710-9339
Zhenfeng Sheng https://orcid.org/0000-0001-6938-8670
Chenwei Yang https://orcid.org/0000-0003-4975-2333
Luming Sun https://orcid.org/0000-0002-7223-5840
Hongyan Zhou https://orcid.org/0000-0003-1956-9021

References

Abolfathi, B., Aguado, D. S., Aguilar, G., et al. 2018, ApJS, 235, 42
Arcavi, I., Gal-Yam, A., Sullivan, M., et al. 2014, ApJ, 793, 38
Arcavi, I., Howell, D. A., Kasen, D., et al. 2017, Natur, 551, 210
Assef, R. J., Prieto, J. L., Stern, D., et al. 2018, ApJ, 866, 26
Auchettl, K., Ramirez-Ruiz, E., & Guillochon, J. 2018, ApJ, 852, 37
Baldwin, J. A., Phillips, M. M., & Terlevich, R. 1981, PASP, 93, 5
Barvainis, R. 1987, ApJ, 320, 537
Bell, E. F., Wolf, C., Meisenheimer, K., et al. 2004, ApJ, 608, 752
Bentz, M. C., Denney, K. D., Grier, C. J., et al. 2013, ApJ, 767, 149
Blagorodnova, N., Gezari, S., Hung, T., et al. 2017, ApJ, 844, 46
Blanchard, P. K., Nicholl, M., Berger, E., et al. 2017, ApJ, 843, 106
Blanton, M. R., Brinkmann, J., Csabai, I., et al. 2003, AJ, 125, 2348
Blanton, M. R., & Roweis, S. 2007, AJ, 133, 734
Bloom, J. S., Giannios, D., Metzger, B. D., et al. 2011, Sci, 333, 203
Bruzual, G., & Charlot, S. 2003, MNRAS, 344, 1000
Burrows, D. N., Kennea, J. A., Ghisellini, G., et al. 2011, Natur, 476, 421
Calzetti, D. 2001, PASP, 113, 1449
Cappellari, M., & Emsellem, E. 2004, PASP, 116, 138

Chambers, K. C., Magnier, E. A., & Metcalfe, N. 2016, arXiv:1612.05560
Chang, Y.-Y., van der Wel, A., da Cunha, E., et al. 2015, ApJS, 219, 8
Chary, R., & Elbaz, D. 2001, ApJ, 556, 562
Chilingarian, I. V., Zolotukhin, I. Y., Katkov, I. Y., et al. 2017, ApJS, 228, 14
Cid Fernandes, R., Stasińska, G., Schlickmann, M. S., et al. 2010, MNRAS, 403, 1036
Combes, F., Mamon, G. A., & Charmandaris, V. 2000, PASP, 112, 423
da Cunha, E., Charlot, S., & Elbaz, D. 2008, MNRAS, 388, 1595
Dai, B. B., Shu, X. W., Jiang, N., et al. 2020, ApJL, 896, L27
Dai, L., McKinney, J. C., Roth, N., et al. 2018, ApJL, 859, L20
Davies, L. J. M., Huynh, M. T., Hopkins, A. M., et al. 2017, MNRAS, 466, 2312
Denney, K. D., De Rosa, G., Croxall, K., et al. 2014, ApJ, 796, 134
Dong, S., Shappee, B. J., Prieto, J. L., et al. 2016, Sci, 351, 257
Donley, J. L., Brandt, W. N., Eracleous, M., & Boller, T. 2002, AJ, 124, 1308
Doré, O., Werner, M. W., Ashby, M., et al. 2016, arXiv:1606.07039
Dou, L., Wang, T., Jiang, N., et al. 2016, ApJ, 832, 188
Dou, L., Wang, T., Yan, L., et al. 2017, ApJL, 841, L8
Draine, B. T., & Lee, H. M. 1984, ApJ, 285, 89
Drake, A. J., Djorgovski, S. G., & Graham, M. J. 2019, MNRAS, 482, 98
Drake, A. J., Djorgovski, S. G., Mahabal, A., et al. 2009, ApJ, 696, 870
Eales, S. 1993, ApJ, 404, 51
Evans, C. R., & Kochanek, C. S. 1989, ApJL, 346, L13
Fitzpatrick, E. L. 1999, PASP, 111, 63
Fox, O. D., Filippenko, A. V., Skrutskie, M. F., et al. 2013, AJ, 146, 2
Fraser, M., Rybicki, K., Gromadzki, M., et al. 2017, ATel, 10747, 1
Frederick, S., Gezari, S., Graham, M. J., et al. 2019, ApJ, 833, 31
French, K. D., Arcavi, I., & Zabludoff, A. 2016, ApJL, 818, L21
French, K. D., Arcavi, I., Zabludoff, A. I., et al. 2020, ApJ, 891, 93
Fritz, J., Franceschini, A., & Hatziminaoglou, E. 2006, MNRAS, 366, 767
Gal-Yam, A. 2019, ARA&A, 57, 305
Gal-Yam, A., Mazzali, P. A., Manulis, I., et al. 2013, PASP, 125, 749
Gezari, S., Hung, T., Cenko, S. B., et al. 2017, ApJ, 835, 144
Goobar, A., Amanullah, R., Kulkarni, S. R., et al. 2017, Sci, 356, 291
Graham, M. J., Djorgovski, S. G., Drake, A. J., et al. 2017, MNRAS, 470, 4112
Graham, M. J., Kulkarni, S. R., Bellm, E. C., et al. 2019a, PASP, 131, 078001
Graham, M. J., Ross, N. P., Stern, D., et al. 2019b, MNRAS, 491, 4925
Greene, J. E., & Ho, L. C. 2007, ApJ, 670, 92
Guillochon, J. 2017, NatAs, 1, 0068
Guo, H., Peng, J., Zhang, K., et al. 2020, ApJ, 905, 52
Haehnelt, M. G., & Rees, M. J. 1993, MNRAS, 263, 168
Harris, C. E., Nugent, P. E., Horesh, A., et al. 2018, ApJ, 868, 21
Hills, J. G. 1975, Natur, 254, 295
Hoffman, D. I., Cutri, R. M., Masci, F. J., et al. 2012, AJ, 143, 118
Hutsemékers, D., Agís González, B., Marin, F., et al. 2019, A&A, 625, A54
Jencson, J. E., Kasliwal, M. M., Adams, S. M., et al. 2019, ApJ, 886, 40
Jiang, N. 2018, RNAAS, 2, 134
Jiang, N., Dou, L., Wang, T., et al. 2016, ApJL, 828, L14
Jiang, N., Wang, T., Hu, X., et al. 2021, ApJ, submitted
Jiang, N., Wang, T., Mou, G., et al. 2019, ApJ, 871, 15
Jiang, N., Wang, T., Yan, L., et al. 2017, ApJ, 850, 63
Jiang, N., Zhou, H.-Y., Ho, L. C., et al. 2012, ApJL, 759, L31
Kaiser, N. 2004, Proc. SPIE, 5489, 11
Kankare, E., Kotak, R., Mattila, S., et al. 2017, NatAs, 1, 865
Kasliwal, M. M., Bally, J., Masci, F., et al. 2017, ApJ, 839, 88
Kaspi, S., Maoz, D., Netzer, H., et al. 2005, ApJ, 629, 61
Kellermann, K. I., Condon, J. J., Kimball, A. E., Perley, R. A., & Ivezić, Ž. 2016, ApJ, 831, 168
Kellermann, K. I., Sramek, R., Schmidt, M., et al. 1989, AJ, 98, 1195
Kewley, L. J., Groves, B., Kauffmann, G., & Heckman, T. 2006, MNRAS, 372, 961
Kochanek, C. S., Shappee, B. J., Stanek, K. Z., et al. 2017, PASP, 129, 104502
Komossa, S. 2015, JHEAp, 7, 148
Kormendy, J., & Ho, L. C. 2013, ARA&A, 51, 511
Koshida, S., Minezaki, T., Yoshii, Y., et al. 2014, ApJ, 788, 159
Kostrzewa-Rutkowska, Z., Jonker, P. G., & Hodgkin, S. T. 2018, MNRAS, 481, 307
Kozlowski, S., Kochanek, C. S., Stern, D., et al. 2010, ApJ, 722, 1624
LaMassa, S. M., Cales, S., Moran, E. C., et al. 2015, ApJ, 800, 144
Lamastra, A., Bianchi, S., Matt, G., et al. 2009, A&A, 504, 73
Laor, A., & Draine, B. T. 1993, ApJ, 402, 441
Law, N. M., Kulkarni, S. R., Dekany, R. G., et al. 2009, PASP, 121, 1395
Lawrence, A., Warren, S. J., & Almaini, O. 2007, MNRAS, 379, 1599
Law-Smith, J., Ramirez-Ruiz, E., Ellison, S. L., & Foley, R. J. 2017, ApJ, 850, 22
Lazo, B., Zahid, H. J., Sohn, J., et al. 2018, RNAAS, 2, 234
Lezhnin, K., & Vasiliev, E. 2015, ApJL, 808, L5
Liao, N.-H., Dou, L.-M., Jiang, N., et al. 2019, ApJL, 879, L9
Liu, H.-Y., Liu, W.-J., Dong, X.-B., et al. 2019, ApJS, 243, 21
Lu, H., Zhou, H., Wang, J., et al. 2006, AJ, 131, 790
Lu, W., & Kumar, P. 2018, ApJ, 865, 128
Lu, W., Kumar, P., & Evans, N. J. 2016, MNRAS, 458, 575
Lu, W., Kumar, P., & Narayan, R. 2017, MNRAS, 468, 910
Lyu, J., Rieke, G. H., & Smith, P. S. 2019, ApJ, 886, 33
MacLeod, C. L., Ross, N. P., Lawrence, A., et al. 2016, MNRAS, 457, 389
Mainzer, A., Bauer, J., Cutri, R. M., et al. 2014, ApJ, 792, 30
Mainzer, A., Bauer, J., Grav, T., et al. 2011, ApJ, 731, 53
Maraston, C., Pforr, J., Henriques, B. M., et al. 2013, MNRAS, 435, 2764
Martin, D. C., Fanson, J., Schiminovich, D., et al. 2005, ApJL, 619, L1
Mathis, J. S., Rumpl, W., & Nordsieck, K. H. 1977, ApJ, 217, 425
Mattila, S., Pérez-Torres, M., Efstathiou, A., et al. 2018, Sci, 361, 482
McConnell, N. J., & Ma, C.-P. 2013, ApJ, 764, 184
McElroy, R. E., Husemann, B., Croom, S. M., et al. 2016, A&A, 593, L8
Mockler, B., Guillochon, J., & Ramirez-Ruiz, E. 2019, ApJ, 872, 151
Mor, R., & Netzer, H. 2012, MNRAS, 420, 526
Moustakas, J., Coil, A. L., Aird, J., et al. 2013, ApJ, 767, 50
Nenkova, M., Sirocky, M. M., Ivezić, Z., & Elitzur, M. 2008, ApJ, 685, 147
Oknyansky, V. L., Winkler, H., Tsygankov, S. S., et al. 2019, MNRAS, 483, 558
Pasham, D. R., Remillard, R. A., Fragile, P. C., et al. 2019, Sci, 363, 531
Phinney, E. S. 1989, in IAU Symp. 136, The Center of the Galaxy, ed. M. Morris (Dordrecht: Kluwer Academic), 543
Rees, M. J. 1988, Natur, 333, 523
Reines, A. E., & Volonteri, M. 2015, ApJ, 813, 82
Ross, N., Assef, R. J., Kirkpatrick, J. D., & Graham, M. J. 2019, BAAS, 51, 321
Roth, N., Rossi, E. M., Krolik, J. H., et al. 2020, SSRv, 216, 114
Runnoe, J. C., Brotherton, M. S., & Shang, Z. 2012, MNRAS, 422, 478
Runnoe, J. C., Cales, S., Ruan, J. J., et al. 2016, MNRAS, 455, 1691
Sarzi, M., Falcón-Barroso, J., Davies, R. L., et al. 2006, MNRAS, 366, 1151
Schechter, P. 1976, ApJ, 203, 297
Schlegel, D. J., Finkbeiner, D. P., & Davis, M. 1998, ApJ, 500, 525
Schmidt, M. 1968, ApJ, 151, 393
Shappee, B. J., Prieto, J. L., Grupe, D., et al. 2014, ApJ, 788, 48
Sheng, Z., Wang, T., Jiang, N., et al. 2017, ApJL, 846, L7
Sheng, Z., Wang, T., Jiang, N., et al. 2020, ApJ, 889, 46
Skrutskie, M. F., Cutri, R. M., Stiening, R., et al. 2006, AJ, 131, 1163
Stalevski, M., Fritz, J., Baes, M., Nakos, T., & Popović, L. Č. 2012, MNRAS, 420, 2756
Stern, D., McKernan, B., Graham, M. J., et al. 2018, ApJ, 864, 27
Stone, N. C., & Metzger, B. D. 2016, MNRAS, 455, 859
Stone, N. C., Vasiliev, E., Kesden, M., et al. 2020, SSRv, 216, 35
Strateva, I., Ivezić, Ž., Knapp, G. R., et al. 2001, AJ, 122, 1861
Strauss, M. A., Weinberg, D. H., Lupton, R. H., et al. 2002, AJ, 124, 1810
Suganuma, M., Yoshii, Y., Kobayashi, Y., et al. 2006, ApJ, 639, 46
Sun, L., Jiang, N., Wang, T., et al. 2020, ApJ, 898, 129
Svirski, G., Piran, T., & Krolik, J. 2017, MNRAS, 467, 1426
Tadhunter, C., Spence, R., Rose, M., Mullaney, J., & Crowther, P. 2017, NatAs, 1, 0061
Thomas, D., Steele, O., Maraston, C., et al. 2013, MNRAS, 431, 1383
Tinyanont, S., Kasliwal, M. M., Fox, O. D., et al. 2016, ApJ, 833, 231
Tonry, J. L., Denneau, L., Heinze, A. N., et al. 2018, PASP, 130, 064505
Trakhtenbrot, B., Arcavi, I., Ricci, C., et al. 2019, NatAs, 3, 242
Ulrich, M.-H., Maraschi, L., & Urry, C. M. 1997, ARA&A, 35, 445
van der Marel, R. P., Alves, D. R., Hardy, E., & Suntzeff, N. B. 2002, AJ, 124, 2639
van Velzen, S. 2018, ApJ, 852, 72
van Velzen, S., & Farrar, G. R. 2014, ApJ, 792, 53
van Velzen, S., Gezari, S., Hammerstein, E., et al. 2020, arXiv:2001.01409
van Velzen, S., Mendez, A. J., Krolik, J. H., & Gorjian, V. 2016, ApJ, 829, 19
Wang, J., & Merritt, D. 2004, ApJ, 600, 149
Wang, T., Yan, L., Dou, L., et al. 2018, MNRAS, 477, 2943
Wang, T.-g., Jiang, N., Ge, J., et al. 2019, ApJL, 886, L5
Wang, T.-G., Zhou, H.-Y., Komossa, S., et al. 2012, ApJ, 749, 115
Wevers, T., Pasham, D. R., van Velzen, S., et al. 2019, MNRAS, 488, 4816
Wright, E. L., Eisenhardt, P. R. M., Mainzer, A. K., et al. 2010, AJ, 140, 1868
Xiao, T., Barth, A. J., Greene, J. E., et al. 2011, ApJ, 739, 28
Yan, L., Wang, T., Jiang, N., et al. 2019, ApJ, 874, 44
Yang, C.-W., Wang, T.-G., Ferland, G., et al. 2013, ApJ, 774, 46
Yang, Q., Wu, X.-B., Fan, X., et al. 2018, ApJ, 862, 109
Zahid, H. J., Geller, M. J., Fabricant, D. G., et al. 2016, ApJ, 832, 203